QATAR UNIVERSITY

COLLEGE OF ENGINEERING

MULTIPHASE MODULAR MULTILEVEL CONVERTER BASED DRIVE SYSTEM FOR OIL AND GAS RECOVERY IN SUBSEA APPLICATIONS

BY

MOHAMED DAOUD

A Dissertation Submitted to

The College of Engineering

In Partial Fulfillment of the Requirements for the Degree of

Doctor of Philosophy

June 2019

COMMITTEE PAGE

The members of the Committee approve the Dissertation of
Mohamed Daoud defended on 18/04/2019.

Prof. Ahmed Massoud
Dissertation Supervisor

Prof. Radu Bojoi
Dissertation Supervisor

Prof. Haitham Abu-Rub
Committee Member

Prof. Lazhar Ben-Brahim
Committee Member

Dr. Atif Iqbal
Committee Member

Prof. Fares AlMomani
Committee Member

Approved:

Abdel Magid Hamouda, Dean, College of Engineering

ABSTRACT

Daoud, M., Ph.D. June 2019. Doctor of Philosophy.

Title: An Efficient and Reliable Drive System for Oil and Gas Recovery in Subsea Applications.

Ph.D. Supervisor: Prof. Ahmed Massoud.

Adjustable Speed Drives (ASDs) in subsea/offshore oil and gas applications are involved in several processes throughout production, transportation, and treatment phases, as they supply pumps and compressors. Therefore, ASDs' in subsea applications have gone through continuous development. The currently existing systems exhibit several energy-conversion challenges that negatively impact the industry costs and green energy. In order to improve the energy-conversion efficiencies, this thesis, apparently, adopts a trend of using low-rating semiconductor devices to handle medium-/high-voltage levels along the various drive system stages. A trend that is believed, by the author, to become in the near future the foundation of flexible, redundant, and compact energy-conversion in the majority of medium-/high-voltage power applications. This thesis proposes the employment of Modular Multilevel Converters (MMCs) in MV-ASD applications in order to ease a transformerless operation while handling medium voltages using low-rating semiconductors. This, in return, reduces the system size and weight. The zero-/low-speed operation of MMC-based ASDs (a main challenge of applying MMCs in ASDs) is investigated in this thesis. The recent techniques proposed to improve operation during those intervals, implement complex hardware/software approaches. To cope with this issue, this thesis proposes multiphase machines for MMC-based AC-drives. Among several advantages regarding the power splitting, multiphase machines provide additional degrees of freedom compared to their three-phase counterparts. Novel

exploitation to these additional degrees of freedom is proposed by injecting a secondary current component in the load current with specific magnitude and frequency during zero-/low-speed intervals enabling the drive system to function duly. Since the control of these secondary components is already inherited in the current controller structure of any multiphase machine, no additional algorithms or sensors will be required. Moreover, a hybrid-boost MMC converter is proposed to boost the MMC output voltage. The stepped output voltage generated by the MMC reduces or eliminates the filtering requirements. The boosting capability of the proposed architecture eliminates the need for bulky low-frequency transformers at the converter output terminals. In order to enhance the drive output torque, a Trapezoidal Phase Disposition Pulse Width Modulation Technique (TPD-PWM) is proposed in this thesis. Different slope angles of the trapezoidal modulation signal are tested and compared to other modulation techniques in order to select the angle with the best torque enhancement meanwhile maintaining good Total Harmonic Distortion (THD) levels. Moreover, the adopted modulation technique reduces the switching losses compared to the conventional Sinusoidal-based PWM. Eventually, a series-connected Half-Bridge (HB) modules are proposed as an Active Front End (AFE) rectifier for the drive system in order to generate an adequate DC-link voltage for the medium-voltage drive system using low-rating semiconductor devices. The proposed techniques through this thesis have been supported with both experimental and simulation results.

DEDICATION

To my parents, for their endless love, support, and encouragement.

ACKNOWLEDGMENT

I would like to express my gratitude to Prof. Ahmed Massoud for his guidance, support, and dedication.

I would like to thank Prof. Radu Bojoi for his support and collaboration.

I also would like to thank Prof. Shehab Ahmed, Dr. Ayman Sami, and Dr. Ahmed Elserougi for their inspiration and support.

This dissertation was made possible by GSRA grant 2-1-0609-14027 from the Qatar National Research Fund (a member of Qatar Foundation).

TABLE OF CONTENTS

LIST OF TABLES

LIST OF FIGURES

LIST OF TERMS | ABBREVIATIONS

2L	Two Level
AC	Alternative Current
AFE	Active Front End
ASD	Adjustable Speed Drives
CHB	Cascaded Half Bridge
CMV	Common Mode Voltage
DC	Direct Current
DSP	Digital Signal Processor
ESP	Electrical Submersible Pumps
FB	Full Bridge
FFM	Fundamental Frequency Modulation
FFT	Fast Fourier Transform
FPSO	Floating Production Storage and Offloading
HB	Half Bridge
HVDC	High Voltage Direct Current
IGBT	Insulated-Gate Bipolar Transistor
IM	Induction Machine
MLC	Multilevel Converters
MMC	Modular Multilevel Converter
MV	Medium Voltage
NPC	Neutral Point Clamped
NLM	Nearest Level Modulation
PD	Phase Disposition

PI	Proportional-Integral
PLL	Phase-Locked Loop
PMSM/PMSG	Permanent Magnet Synchronous Motor/Generator
PR	Proportional-Resonant
PWM	Pulse Width Modulation
Q2L	Quasi Two-Level
SM	Sub Module
SPD	Sinusoidal Phase Disposition
THI	Third Harmonic Injection
TPD	Trapezoidal Phase Disposition
VSC	Voltage Source Converter

CHAPTER 1: INTRODUCTION

The biggest challenge of the 21st century is providing sufficient energy, food, and water in order to encounter the increasing population and climate change threats. In this context, oil and gas are considered the main energy supplies on the planet. Despite the depletion of conventional oil and gas resources, tremendous resources are expected to be available subsea. That has forced the companies to explore in harsher locations and deeper water than currently reachable. Given those conditions, then lower maintenance, higher reliability, and longer life cycles are needed.

1.1. Power Supply in Subsea Oil and Gas Applications

Practically, the production process, such as pumping (oil), and compression (gas), requires employing different sorts of mechanical and electrical equipment. For instance, in oil production, different types of pumps, such as Electrical Submersible Pumps (ESPs) and multi-phase pumps, are used for extracting the oil from the reservoirs during different recovery stages. ESPs are installed inside the well and immersed in the oil. It is considered a pump-motor combination with limiting diameter to enhance the capability of down-hole installation [1], [2]. The multi-phase pumps are not deployed in the oil reservoir but installed on the seabed directly with conventional motor-pump configuration; they can be employed with applications up to 5 MW. The multi-phase term refers to the fluid passing through the pump, which can be gas, liquid or a combination of both [3].

For subsea oil and gas production, the power supply system consists of two main stages, onshore and offshore. The onshore stage includes the generation/rectification station, whilst the offshore stage contains the drive system for pumps/compressors. Both mechanical (i.e., gas turbines or reciprocating engine) and electrical ASDs have been applied in subsea applications [4].

ASDs are involved in the majority of the processes in the oil and gas industry such as the production, storage, transportation, and gas treatment/liquefaction, as these processes mainly depend on pumps and compressors. However, a low percentage of the medium-voltage motors are, generally, controlled via variable speed medium-voltage drives, as the main concern is the handling/control of high voltage levels [5].

The power converter is a basic part of the ASD, where higher efficiency and reliability of the converter have been always sought to reduce the energy loss and enhance the power quality at such high ratings. Therefore, the conventional Multilevel Converters (MLCs), such as Neutral Point Clamped (NPC), flying capacitor, and Cascaded Half-Bridge (CHB), were introduced in [6]–[11] as suitable candidates for medium-voltage applications. Recently, MMCs have been developed as a replacement of the conventional MLCs due to MMC's several merits such as modularity which enable the converter to handle high voltage levels with low-rating semiconductors, lower output harmonic contents, high efficiency, lower switching frequencies, and elimination of isolated input power supply [12]. MMC is a promising replacement in many applications that encounter conventional MLCs bulkiness and complexity issues [3]. MMC was first introduced in 2003 [13], where its modularity is based on building a large converter via combining cascaded building blocks which enables higher voltages handling [14]. Over the last decade, there has been considerable research work studying the development of the MMC regarding its operation, topology, applications, and control [4].

1.2. Problem Statement

In subsea applications, the electrical drive system for seabed motor-compressor/motor-pump combinations is commonly located offshore and topside on subsea Floating Production Storage and Offloading (FPSO) vessels far from the seabed with distances

can reach up to 150 km [15]. Thus, the footprint and the weight of the applied ASD system is a critical design criterion. Several technical requirements should be considered for an optimal design, including:

- Power density (MW/m^3).
- Specific power (MW/kg).
- Footprint (m^2/MW).
- Efficiency.
- Cost ($/MW).
- Reliability (mean time to the first failure and mean time between failures in years).

Commonly, these drive systems are operated at medium-voltage levels [16]; for instance, the drive systems such as the ASC 1000 (4.16kV with 5MW), ASC 2000 (6.9kV with 1.6MW), ASC 6000 (3.3kV with 27MW), and PSC 8000 (6.6kV with 100MW) [16]. In these medium-voltage medium-/high-power drives, three main components should be considered for proper design and operation, namely:

- The power converters (DC/AC and AC/DC).
- The electric machine.
- The transformers and filters, particularly when considering long feeders.

Conventionally, a drive system containing Two-Level (2L)-Voltage Source Converter (VSC) and three-phase Permanent Magnet Synchronous Motor (PMSM) or Induction Motor (IM), as shown in Figure 1, is applied due to its simplicity.

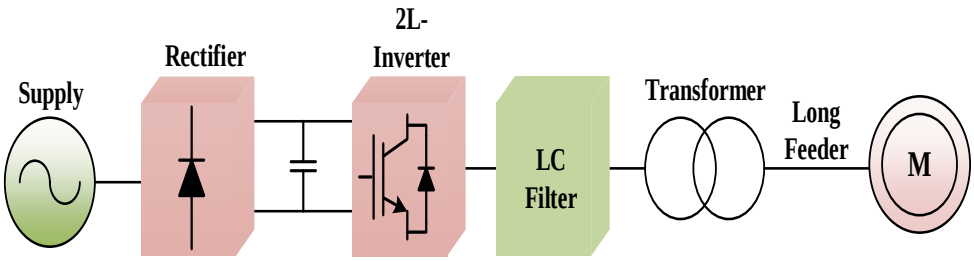

Figure 1. Conventional AC drive system structures

In that configuration, the harmonic content of the 2L-VSC output may interact with the long cable characteristics causing parallel resonance, which may lead to high voltage distortion levels [1]. In order to cope with this phenomenon, a large size passive harmonic filter must be installed. In addition, the longer the cable is, the higher the voltage drop [1]–[3], [17]. Long cables when associated with medium-voltage drives reduce the motor lifetime due to the voltage stress on the winding insulation. In order to reduce the voltage drop and transmission losses, typically the transmission voltage should be raised up using low-frequency transformers [17]. The effect of the long cable with submersible multiphase IMs was studied in [18], [19]. Such a drive system's peripherals affect negatively the motor torque, power density, specific power, footprint, and reliability. Meanwhile, the reliability and fault tolerance of that system are questioned as well. Thereafter, the three-phase drive system is usually duplicated as a backup to reduce the downtime. Practically, in order to cope with the high voltage ratings, a 2L-VSC with step-up transformers or a series-connected based 2L-VSCs can be used, yet on the expense of efficiency, reliability, and footprint.

Therefore, such a drive system may require [5]:

1) A bulky transformer at the converter output due to the limitations/unavailability of high-voltage switching devices.
2) A series connection operation of semiconductor devices.

3) Filtering stages at the converter output.
4) A high switching frequency operation to reduce the size of the output filter, hence higher switching losses.
5) A sensor-based motor control, which is a challenge for subsea applications.

These requirements negatively affect the drive system efficiency and reliability. Therefore, solution is sought in this work to overcome their negative impact. However, the sensor-based motor control will not be targeted in this work.

Moreover, the cost is the key player in the subsea industry's investment, where the weight of the system installed on a platform/vessel is a crucial factor. Therefore, any reduction in platform weight leads to significant cost-cutting.

In order to enhance the power density, specific power, and footprint, a transformerless and filterless operation is targeted. This can be achieved through multilevel converters, which enhance the power quality and reduce the *dv/dt* stresses, enabling the deployment of low-voltage semiconductor devices for handling higher voltage ratings. The NPC and flying-capacitor converters affect system reliability due to the high number of employed devices, in addition to the high complexity with increasing their levels. Whilst CHB requires isolated input DC sources. Hence, the system power density and specific power decrease. Alternatively, MMCs overcome the aforementioned drawbacks and enhance the modularity and reliability using simple HB modules without the need of isolated input supply. Moreover, the attainable stepped voltage levels yield lower harmonic content and *dv/dt,* which eliminates/reduces the required bulky passive components (i.e., the filter at the converter output terminals).

The power supply of the ASD is an extra challenge. Typically, AC transmission can be used to supply the whole platform in case of short offshore distances and light loads. However, High Voltage DC (HVDC) transmission is usually applied in case of longer

distances and higher loads due to economic reasons (lower losses than AC transmission). Power supply to the ASD using rectification stage may require, as well, bulky transformer stage.

This work aims to study the performance of the MMC for high-power medium-voltage variable speed drives in subsea oil and gas industry. The main concerns of subsea drive systems for oil and gas applications, that believed can be improved by using MMCs, can be summarized as follows:

- Low specific power, power density, and footprint due to the bulky volume of the drive system employing bulky transformers and filters.
- The drive system behavior under unbalance or faulty operations that affect system reliability.
- The effect of the long feeder on the delivered waveforms to the motor that requires extra equipment such as filters.
- The supply of adequate DC-link voltage.
- Low switching frequency operation.

Therefore, an enhanced drive system that addresses these concerns in a simpler approach may improve the overall efficiency and reliability significantly.

1.3. Research Objectives

The thesis seeks a simple and flexible offshore drive system, which is able to offer high reliability and efficiency, meanwhile, reduce the footprint and cost. That is believed to be achieved using modular systems were low-rating switching devices can handle higher voltage levels. The thesis adopts an MMC-based ASD. As well, adopting a series-connected low-rating HB module to provide adequate DC-link voltage for the medium-voltage ASD. The proposed drive system is believed to fulfill some essential features such as compact size, modularity, high-voltage handling capability,

transformerless operation, high quality of delivered waveforms, approximately seamless operation with long feeders, and fault ride-through capability.

Those features may be highly attractive for oil and gas subsea drive systems due to:

- Subsea industry is a high power application in the range of megawatts, therefore developing an MMC-based drive system suits the high power nature of this industry.
- The high quality of the MMC outputs is expected to provide better performance with the existence of long feeders between the drive system and the motor. The high-quality output supports reducing the filter size at the motor side.
- Elimination of the isolated DC power supplies (typically a transformer with multiple secondary sides) in case of CHB-based drive system, as the MMC's HBs do not require isolated power supplies. This increases system efficiency, power density, specific power, and reduces the footprint.
- The proposed drive system is based on a multiphase machine. Hence, no duplication is required for backup purposes, which reduces the drive system specific power, power density, and cost. The number of cables is increased in the proposed system, yet their cross-sectional areas are reduced for the same machine rating.

This thesis proposes scientific-based approaches for the following challenges related to utilizing MMC in subsea drive systems:

- The zero-/low-speed operation of MMC-based drive systems.
- The modulation of the MMC to provide higher output torque while maintaining lower harmonic contents.
- Eliminating the step-up transformer by boosting the MMC output voltage.

- The utilization of series-connected modules in designing an adequate AFE rectifier for medium-voltage drive systems.

1.4. Thesis Contributions

This thesis focuses on the development of MMCs in motor/generator drive systems. Adopting MMCs in ASDs has encountered several technical challenges. The main contributions of the work conducted throughout this thesis can be summarized as follows:

- Providing a new technique to enable a full frequency range operation of the MMC-based ASD. The new technique targets the starting/low-speed operation of MMC-based high-power AC drive systems. It exploits the additional degrees of freedom of a multiphase system. The proposed system eliminates extra hardware devices and complex control solutions typically used in literature. The multiphase operation inherently enhances the drive system reliability, which is crucial for high-power applications. It also allows for a higher torque quality at a lower switching frequency than three-phase systems.

- Providing an MMC with high boosting capability using a lower number of semiconductor switches that enables transformerless operation in medium-voltage drives. A multiphase hybrid-boost MMC-based drive system is proposed. The boosting ratio can reach up to kV_{dc} by increasing the number of Full-Bridge (FB)-SMs, where k is a positive integer.
- Providing a series-connected HB modules-based AC-DC converter that has boosting capability. The proposed AC-DC converter enables transformerless operation capability with an AC-DC boosting gain of $2m$, where m is the number

of the AC side phases. The proposed AC-DC converter provides an adequate AFE that suits the medium-voltage drives' DC-link requirements. This supports employing relatively low-voltage rating semiconductor switches. Hence, the complexity and challenges of series-connection of semiconductor devices are avoided. In addition, each phase can be controlled independently, i.e., a modular controller can be adopted, which reduces the complexity of the controller tuning.

- A trapezoidal modulation technique is proposed for the MMC-base AC-ASDs. It enhances the output torque at low THD levels. The modulation technique provides optimum flattened-top flux distribution, inherited by the waveform construction. The proposed modulation technique reduces switching losses, as no switching needed during the steady flat period of the trapezoidal signal. The proposed modulation provides better harmonic content in the output, through controlling the rising time of the trapezoidal reference. The proposed modulation involves simple algebraic implementation of the reference.
- Hardware prototypes for the proposed techniques have been built to investigate the proposed concepts experimentally.

1.5. Thesis Structure

This work is organized into seven chapters as per the following structure. Chapter 1 presents a brief introduction to research problems and objectives. Chapter 2 is a literature review elucidating the development of the converter topologies in medium-voltage applications up to MMCs. In that chapter, the mathematical model of MMC is presented. Chapter 3 illustrates the main challenge that encounters the utilization of MMC in ASDs, which is the zero-/low-speed operation. In that chapter, a new approach is proposed to cope with that challenge and investigated using simulation and experimental results. Chapter 4 introduces a modified hybrid-boost MMC as better utilization of MMCs in

ASDs. In that chapter, the converter concept is studied, and simulation and experimental are presented. Chapter 5 studies the torque enhancement of the MMC-based drive system using Trapezoidal Phase Disposition-Pulse Width Modulation (TPD-PWM) technique. Chapter 6 proposes a series-connected HB-modules-based AC/DC converter that suits the medium/high voltage application. In that chapter, the converter is investigated for *m*-phase applications. Finally, the overall contribution and deliverables, as well as the expected future work, are summarized in chapter 8. A representation of the thesis structure is depicted on a typical drive system shown in Figure 2.

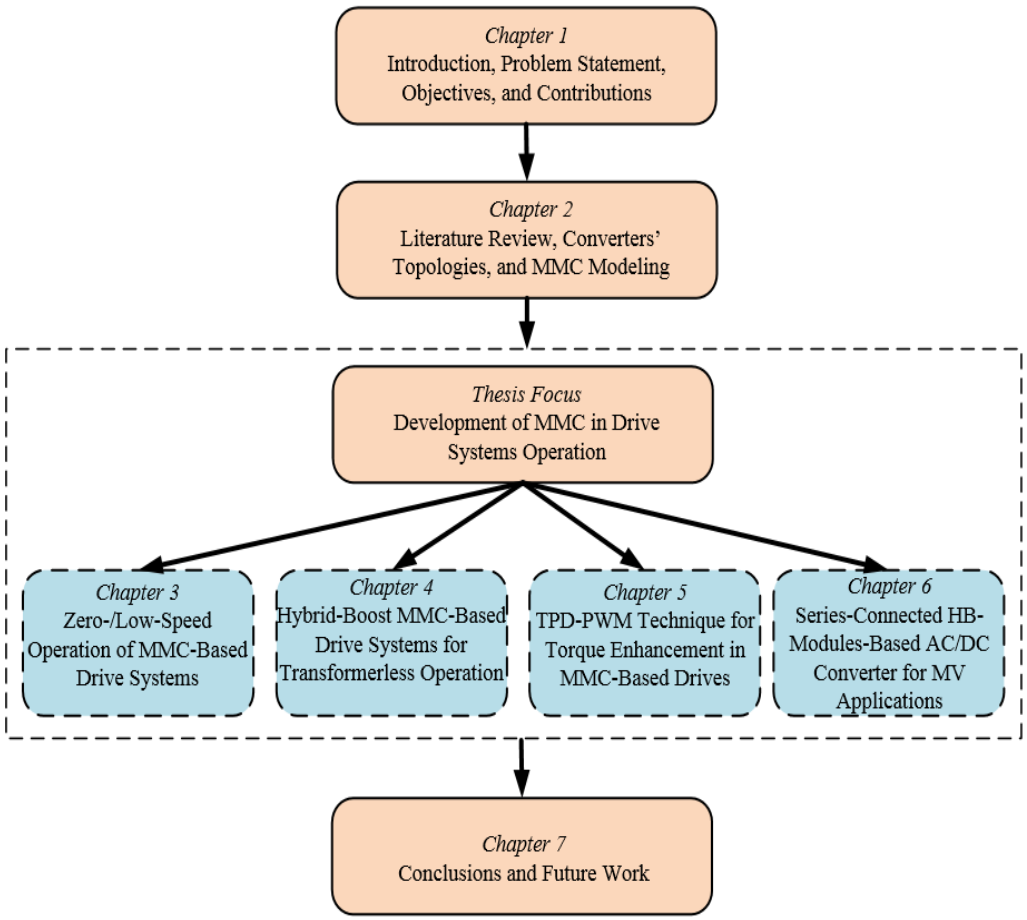

Figure 2. Schematic for thesis structure.

CHAPTER 2: LITERATURE REVIEW

High-power AC-ASDs have become the backbone of several industries and renewable energy applications. Meanwhile, multilevel converters have been introduced as promising candidates in high-power medium-voltage applications. Compared to conventional two-level converters, the multilevel converters meet the high-power AC ASDs' requirements with enhanced performance [5], [20]. Recently, MMC has emerged as a feasible option for high-power medium-/high-voltage applications thanks to converter construction that yields modularity, lower output harmonic content, low switching frequency, and transformer-less operation [21], [22], [23], [24], [25], [26]. This chapter reviews the construction, principle of operation, and modulation techniques of MMC. In the following subsections, a comparison between MMC and conventional converters is presented, as well as, the MMC mathematical model.

2.1. Power Converters Topologies

Due to the great development of the semiconductors devices over the last 50 years, a numerous number of power converters have been introduced. A brief description of the evolution of VSCs is presented in this section.

2.1.1. Conventional Two-Level VSC

The conventional 2L-VSC is shown in Figure 3. It is commonly used with low voltage applications. The main disadvantages of this converter with medium/high voltage applications are the limitations on increasing the voltage, high output harmonics, high switching losses, and low fault tolerance capabilities [8]. Series-connected switching devices, as well as transformers at the converter output, are the common procedure to enable the utilization of this converter in medium-voltage applications, yet on the expense of the converter reliability, size, and footprint.

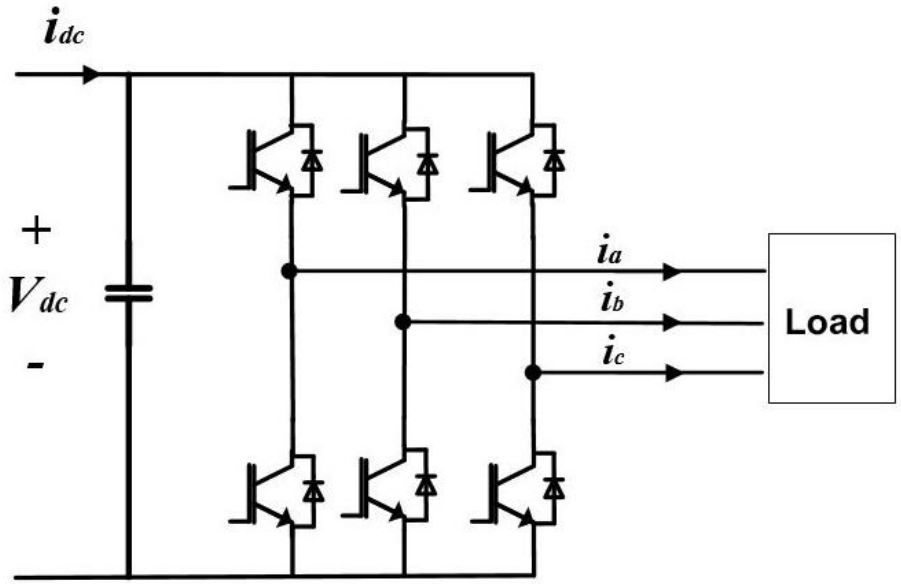

Figure 3. Two-level VSC.

2.1.2. Conventional Multilevel Converters

MLCs have attracted several power applications due to the high voltages handling capability with minimum losses and output harmonic contents compared to the conventional two-level converter [27]. There main conventional MLCs are the NPC, the flying capacitor, and CHB converters [28], [29]. Each converter has its own configuration and features. Conventional MLCs have common disadvantages such as the bulky size at higher voltages, non-extendibility, and reduced fault management capability [30].

A. Neutral Point Converter

The NPC was first introduced earlier in 1980 [7] where it represented the start of multilevel converters that based on the modification of the conventional 2L-VSC. It has been widely used in medium-voltage motor drive applications such as pumps and conveyors. This topology has a capacitive voltage divider where its midpoint being stabilized via clamping diodes [31], [32]. However, the structure may be extended to

any number of levels through increasing the number of capacitors and diodes. The NPC is practically limited to three-level converter due to the difficulty of capacitor voltage balancing and the requirement of a bulky output filter [8]. On the other hand, it has advantages such as the small DC-link capacitor and simple structure [33]. Figure 4 shows the configuration of the NPC.

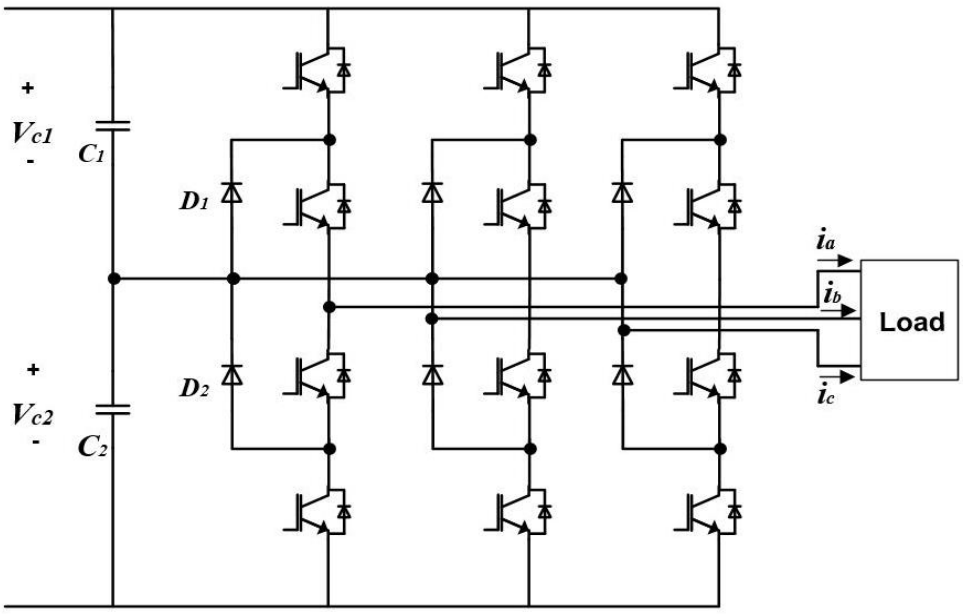

Figure 4. Three-Level Neutral Point Clamped MLC.

B. Flying Capacitor Converter

Years after the NPC, the flying capacitor MLC was introduced with different features. This topology has sorted out some of the NPC converter drawbacks; however, it has concerns relevant to low switching frequencies as the required capacitance inversely increased with respect to the switching frequency, which makes it limited to specific applications. Therefore, for low-frequency applications, NPC and CHB converters are

better candidates [34], [35]. In addition, with increasing the number of levels, a higher number of capacitors is required; hence, the control complexity increases. Figure 5 illustrates the structure of the flying capacitor MLC [9], [36].

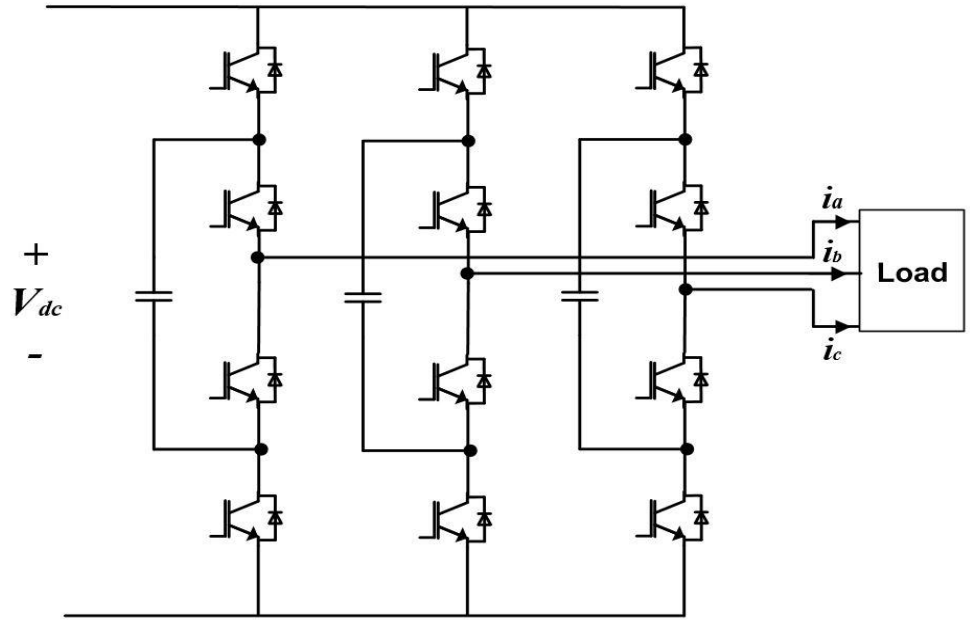

Figure 5. Three-Level Flying Capacitor MLC.

C. Cascaded H-Bridge Converter

The CHB-MLC is considered one of the most reliable topologies of MLCs. This topology [10] is based on the concept of several series-connected single-phase HBs [37]. The five-level CHB-MLC is one of the most commonly applied converters in the oil and gas industry. However, the system requires a large number of isolated power supplies that supply the HBs which increases the system cost, footprint, and reduces power density [11], [38], [39]. CHB structure is shown in Figure 6.

CHB-MLC with isolated DC source, shown in Figure 6 is commonly used in the subsea drive system, in order to increase the rating of the converter, and reduce the total

harmonic distortion of the output waveforms using low-rating switching devices [2], [3]. The utilization of NPC and flying capacitors MLCs is not applicable for such an application due to the complexity of the DC-link capacitors balancing with increasing the number of levels [30].

The main concern of CHB-MLC is the need for an isolated input source for each cell, which causes a bulky drive system. In [3], a single primary side, eighteen secondary sides' transformer is particularly manufactured for this application in order to supply isolated source to a three-phase CHB-based ASD where each phase comprises 6 HBs, then; as a result, a bulky transformer is anticipated. Moreover, the cascaded configuration of the cells in each phase causes unbalanced output in case a fault occurs at any of the semiconductor power devices. Furthermore, a large number of semiconductor power devices and gate drives are presented, as each power cell consists of a three-phase diode bridge rectifier, DC-link capacitor, and single phase bridge using four switching devices.

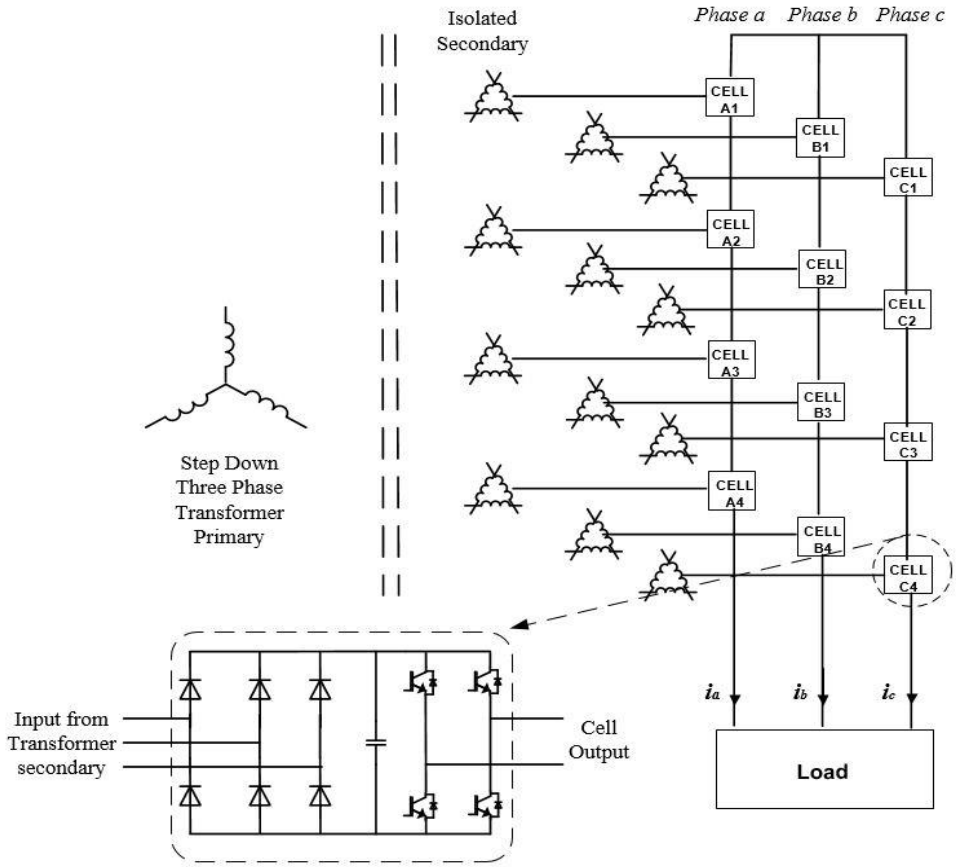

Figure 6. Cascaded H-bridge MLC.

2.2. MMC Structure

MMC is a modular-style converter that is suitable for medium-/high-power applications [40]–[45]. It was first introduced in [13] and mainly consisted of an arbitrary number of identical basic building blocks called SMs. Several configurations for the SM structure can be found in literature [26], [46]. The most common SM structures are HB- and FB-SMs. HB-SM is the simplest as it yields a low number of switching device, hence lower switching losses; in addition to reduced control complexity. Yet, in grid and HVDC applications, FB-SM is the most common due to its DC fault blocking capability. In case of HB-SM, each SM contains an HB circuit (two semiconductor switches) with a capacitor that determines the voltage across the switches [30]. Figure

7 shows the typical MMC structure. The output of the SM is either equal to the capacitor voltage (*on-state*) or equal to zero (*off-state*). Table 1 shows the possible switching states of MMC's SMs. Each phase-leg has two stacks of SMs (upper and lower) called arms where each arm contains *N-1* SMs, considering *N* is the number of converter levels. The higher the number of the SMs, the lower the output harmonic distortion is. The MMC structure allows low switching frequency of the SM's, reaching switching frequencies at the fundamental frequency in some applications [47].

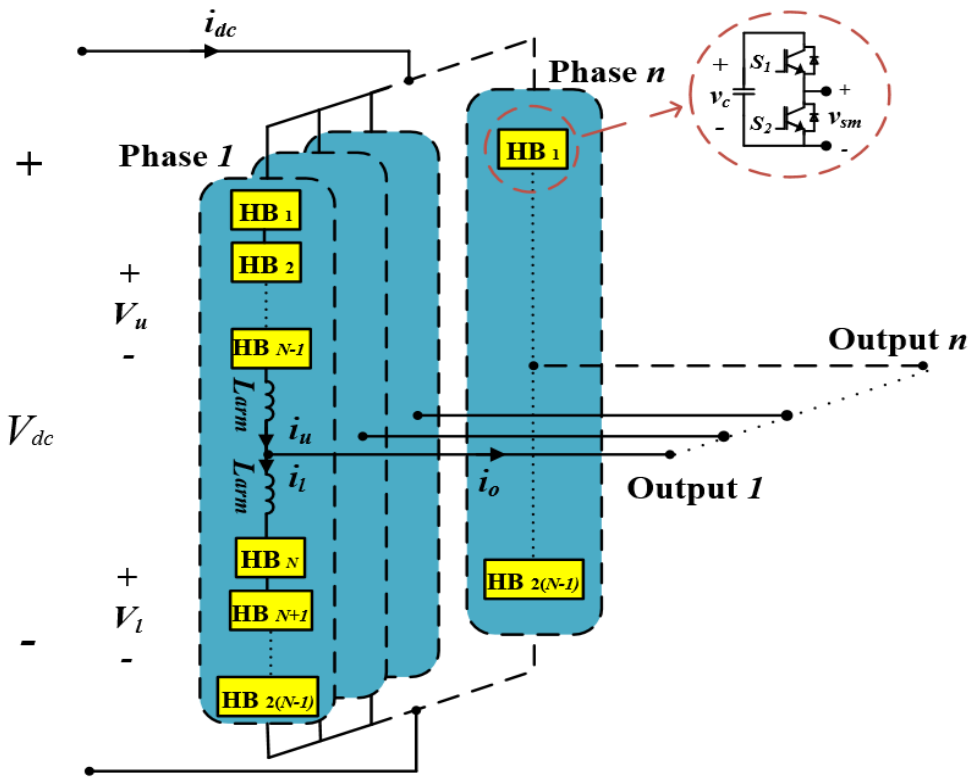

Figure 7. *N*-level *n*-phase MMC.

Table 1. SM's Output States

v_{sm}	S_1	S_2
V_c	on	off
0	off	on

2.2.1. MMC Submodule Configurations

The output of each SM forms the overall MMC's output. Instantaneously, selected SMs are inserted in each arm based on the desired instantaneous value of arm voltage. Therefore, changing the SM topology will lead to changes in the output waveforms [21]. The main SM's configurations studied in literature are briefed in Figure 8, such as two-level SMs HB and FB [48]; as well as three-level SMs such as diode clamped SM, flying capacitor SM [22], [49], clamp-double SM [48], and mixed cells [50], [51]. The two-level SM comprises one capacitor with $v_{sm} = V_c$ at *on-state*. The voltage will appear across cell output terminals if its capacitor is included in the arm current path while zero voltage will appear if its capacitor is bypassed.

The three-level cells are eligible to deliver three-level voltage [0, V_{c1} or V_{c2}, $V_{c1} + V_{c2}$] as they contain two capacitors. Zero output is obtained by bypassing entire SM. Whilst inserting one capacitor and bypassing the other leads to an output voltage of V_{c1} or V_{c2}. Inserting both leads to an output voltage of $V_{c1} + V_{c2}$.

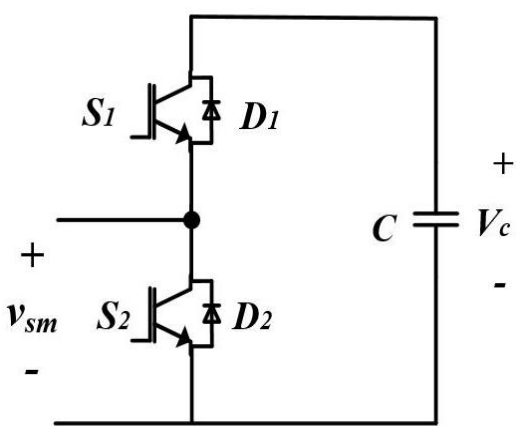
S1
D1
C
Vc
+
vsm
S2
D2
-

(a)

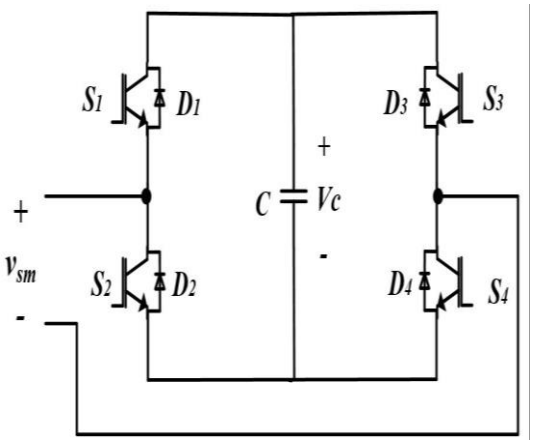
S1
D1
D3
S3
C
Vc
+
vsm
S2
D2
D4
S4

(b)

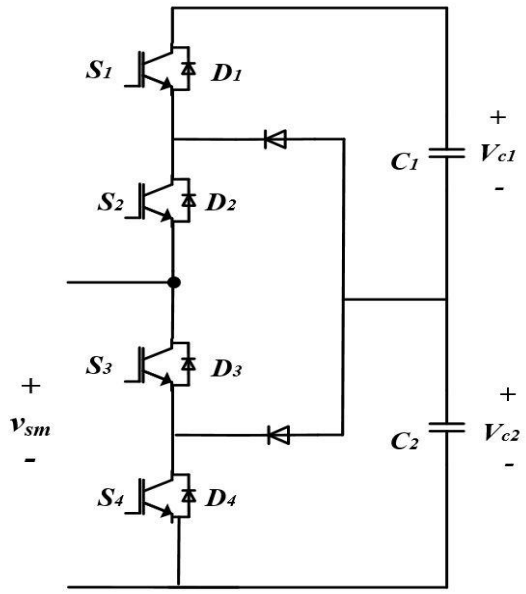
S1
D1
C1
Vc1
S2
D2
S3
D3
vsm
C2
Vc2
S4
D4

(c)

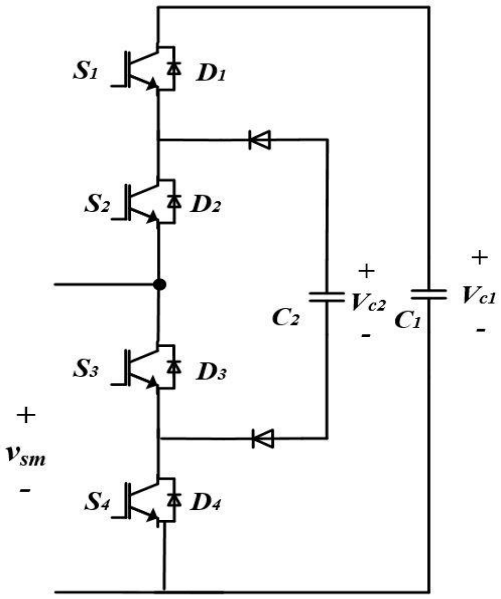
S1
D1
S2
D2
C2
Vc2
C1
Vc1
S3
D3
vsm
S4
D4

(d)

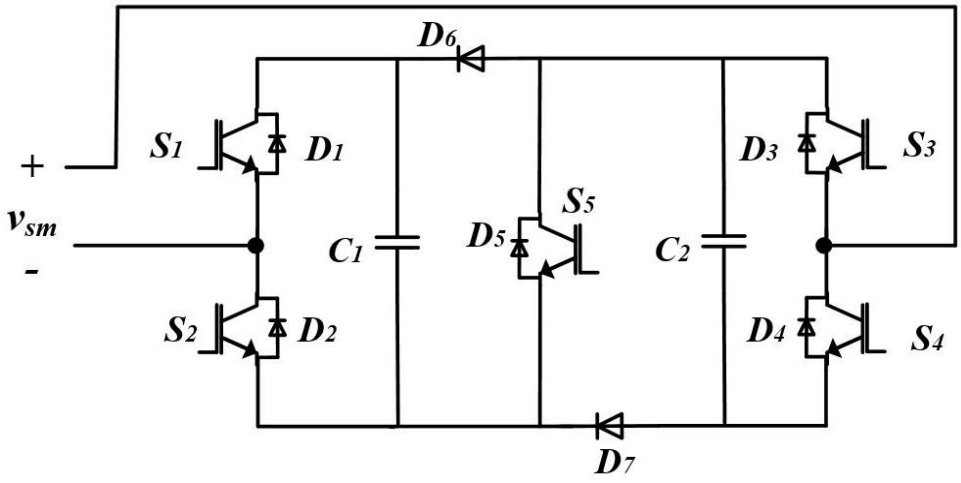
D6
S1
D1
D3
S3
vsm
S5
C1
D5
C2
S2
D2
D4
S4
D7

(e)

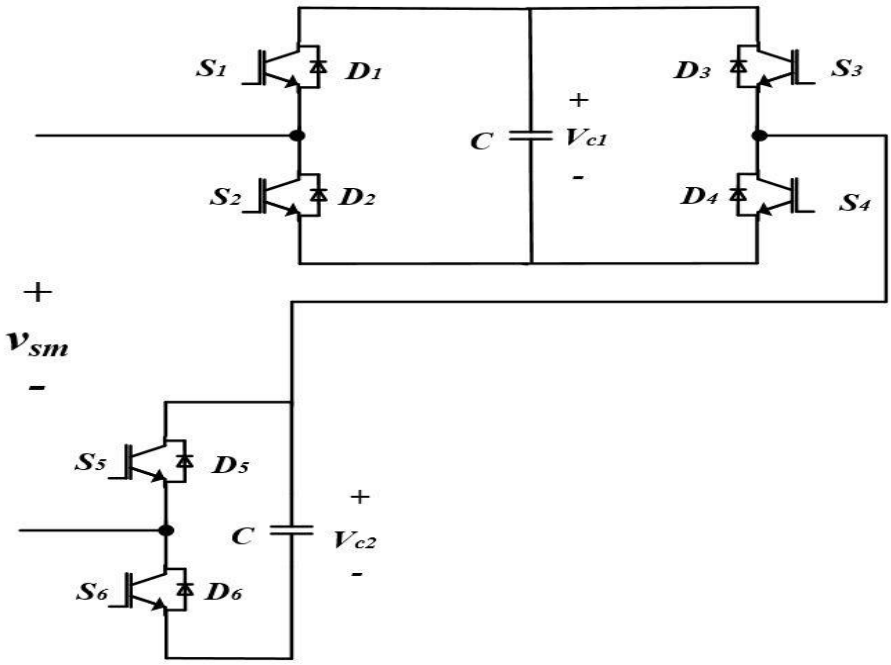

(f)

Figure 8. Submodule topologies: (a) HB, (b) FB, (c) neutral point clamp, (d) flying capacitor, (e) clamp-double, (f) mixed cell.

2.2.2. MMC Mathematical Model

MMC behavior is depicted in this section through mathematical modeling. The mathematical model interprets some concerns related to MMC operation such as SM's capacitor voltage and circulating currents.

At any instant for an *N*-level MMC, the total number of operated SMs per arm is *N-1*. The number of *on-state* SMs per arm is determined by the modulation technique.

The MMC output AC current is given as in (2.1) [52].

$$i_{o,j} = i_{u,j} - i_{l,j} \tag{2.1}$$

where $i_{o,j}$ is the phase-*j* output current, and $i_{u,j}$ and $i_{l,j}$ are the currents flowing in upper and lower arms of phase-*j*, respectively.

Circulating currents are produced internally and flow between the phases' arms and the

DC-link as well. The voltage ripples of the capacitors cause circulating currents to flow between the phase leg and the DC supply with a frequency twice the fundamental. Another source of circulating currents is the variation of the voltage levels in case of a multiphase converter, which imposes a circulating current at the switching frequency [10]. An expression for the circulating current is given in (2.2).

$$i_{circ,j} = \frac{i_{u,j} + i_{l,j}}{2} - \frac{i_{dc}}{n} \tag{2.2}$$

where $i_{circ,j}$ is the circulating current of phase-*j*, $i_{dc}$is the DC-link input current, and *n* is the number of MMC phases.

The upper and lower arms currents in each phase are given by (2.3) and (2.4).

$$i_{u,j} = \frac{i_{dc}}{n} + i_{circ,j} + \frac{i_{o,j}}{2} \tag{2.3}$$

$$i_{l,j} = \frac{i_{dc}}{n} + i_{circ,j} - \frac{i_{o,j}}{2} \tag{2.4}$$

The voltages of upper and lower arms, by applying Kirchhoff's law, can be given by (2.5) and (2.6).

$$v_{u,j} = \frac{V_{dc}}{2} - L_{arm,j}\frac{di_{u,j}}{dt} - v_{o,j} = \sum_{i=1}^{N} x_{u,j}^{i} v_{sm,u,j}^{i} \tag{2.5}$$

$$v_{l,j} = \frac{V_{dc}}{2} - L_{arm,j}\frac{di_{l,j}}{dt} + v_{o,j} = \sum_{i=1}^{N} x_{l,j}^{i} v_{sm,l,j}^{i} \tag{2.6}$$

where *x* is the index of inserted SMs in each arm (*x=1* if SM inserted, *x=0* if not), $L_{arm,j}$ is the arm inductance, V_{dc} is the DC-link voltage, and $v_{sm,j}$ is the SM's output voltage. Therefore, an expression for any SM's capacitor can be given by (2.7).

$$C_{sm}\frac{dv_{sm,u,l,j}^{i}}{dt} = x_{u,l,j}^{i} i_{u,l,j} \tag{2.7}$$

where C_{sm} is the capacitance of the corresponding SM. A relation between the output current and controlled SM voltages can be given by subtracting (2.5) and (2.6) as given

in (2.8).

$$L_{arm,j}\left(\frac{di_{u,j}}{dt}-\frac{di_{l,j}}{dt}\right)=\frac{L_{arm,j}}{2}\frac{di_{o,j}}{dt}=\frac{-v_{u,j}+v_{l,j}}{2}-v_{o,j} \tag{2.8}$$

Another relation between the circulating currents and controlled SM voltages can be given by adding (2.5) and (2.6) as given in (2.9).

$$L_{arm,j}\left(\frac{di_{u,j}}{dt}+\frac{di_{l,j}}{dt}\right)=L_{arm,j}\frac{d\left(i_{circ,j}+\frac{i_{dc}}{n}\right)}{dt}=\frac{V_{dc}}{2}-\frac{v_{u,j}+v_{l,j}}{2} \tag{2.9}$$

Hence, based on (2.8) and (2.9), it can be shown that controlling the term $v_{oc}=\frac{-v_{u,j}+v_{l,j}}{2}$ can drive the output current, while controlling the term $v_{cc}=\frac{v_{u,j}+v_{l,j}}{2}$ can drive the circulating current. For instance, to eliminate circulating current, the term $\frac{V_{dc}}{2}-\frac{v_{u,j}+v_{l,j}}{2}$ must be zero, that means $v_{u,j}=v_{l,j}=\frac{V_{dc}}{2}$. As well, from (2.8), the maximum output voltage can be obtained by inserting all lower SMs, and vice versa.

When a certain SM is inserted, the arm current will charge/discharge the capacitor of that SM. Hence capacitor ripples take place. In order to have a balanced MMC operation, the sum of the upper and lower arms average voltages must be equal to the input DC voltage. In order to have an average model of the MMC, hence the arm voltages can be express by (2.10) and (2.11).

$$V_{u,j}=X_{u,j}\frac{V_{dc}}{N-1} \tag{2.10}$$

$$V_{l,j}=X_{l,j}\frac{V_{dc}}{N-1} \tag{2.11}$$

where X is the number of inserted SMs, and $X_{u,j}+X_{l,j}=N-1$, where N is the number of converter levels.

In order to ensure proper balanced operation, the number of the inserted modules per arm must be controlled. Therefore, expressions for the upper and lower number of inserted SMs (X) in terms of reference control voltages v_{cc}^{*} and v_{oc}^{*} can be written as

(2.12) and (2.13).

$$X_{u,j} = (N-1)\frac{v_{cc}^* - v_{oc}^*}{V_{dc}} \tag{2.12}$$

$$X_{l,j} = (N-1)\frac{v_{cc}^* + v_{oc}^*}{V_{dc}} \tag{2.13}$$

where the reference voltages can be set as:

$$v_{cc}^* = \frac{V_{dc}}{2} \tag{2.14}$$

$$v_{oc}^* = V_m \cos(\omega t) \tag{2.15}$$

From (2.7), the capacitor voltage of the upper or lower arm can be expressed as in (2.16).

$$C_{sm}\frac{dV_{u,l,j}}{dt} = X_{u,l,j} i_{u,l,j} \tag{2.16}$$

Both arm currents and insertion index are fundamental frequency periodic components, where their product generates ripples in the capacitor voltages with a double frequency component.

2.2.3. The Circulating current

Circulating current is a current that flows in the MMC arms without flowing in the output. Capacitor voltage ripples are sources of circulating current, inducing a double-fundamental frequency component. As well, the switching between the phase levels induces circulating current, yet at the switching frequency.

Applying Kirchhoff's law within one-phase yields:

$$V_{u,j} + V_{l,j} + L_{arm,j}\left(\frac{di_{u,j}}{dt} + \frac{di_{l,j}}{dt}\right) = V_{dc} \tag{2.17}$$

Hence,

$$V_{u,j} + V_{l,j} + L_{arm,j}\left(\frac{d(\frac{i_{dc}}{n} + i_{circ,j} + \frac{i_{o,j}}{2})}{dt} + \frac{d(\frac{i_{dc}}{n} + i_{circ,j} - \frac{i_{o,j}}{2})}{dt}\right) = V_{dc} \tag{2.18}$$

where $d\left(\frac{i_{dc}}{n}\right) = 0$.

Therefore, a dynamic expression for the circulating current can be given as (2.19).

$$2L_{arm,j}\left(\frac{di_{circ,j}}{dt}\right) = V_{dc} - (V_{u,j} + V_{l,j}) \tag{2.19}$$

As mentioned before, it is clear that the voltage inducing the circulating current results from the difference between the DC-link voltage and sum of upper and lower arms' voltage.

2.2.4. MMC Modulation Techniques

There are several modulation techniques for MMC switching proposed in literature. The main modulation techniques can be classified as:

A. Sinusoidal Phase Disposition

This technique [42], [53], [54] uses *N* triangular carrier waveforms with the same frequency and amplitude displaced symmetrically along the desired output phase voltages to separately control each phase leg, as shown in Figure 9, taking a 5-level MMC as an example. The comparison between the carriers and the reference waveforms define the *on/off* states of the SMs of each phase by determining the number of SMs to be used within the upper and lower arms. When the reference voltage of the upper arm is at rated positive voltage, all upper SMs are set *on* with lower ones set to zero, and vice versa in case of rated negative voltage. Figure 10 shows the number of required SMs to obtain the desired voltage.

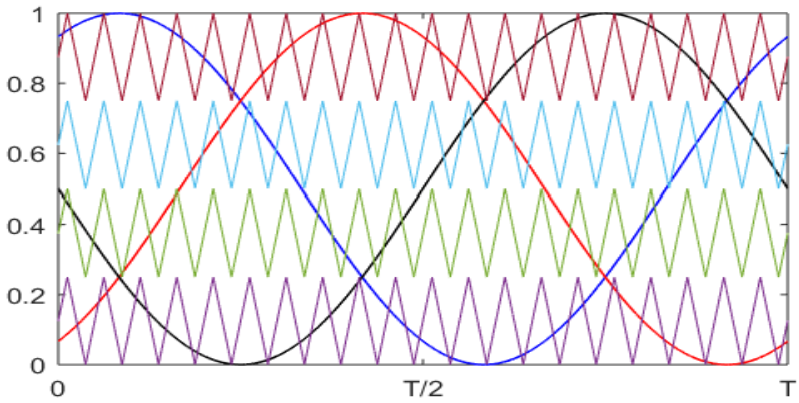

Figure 9. PD modulation technique of 5-level MMC.

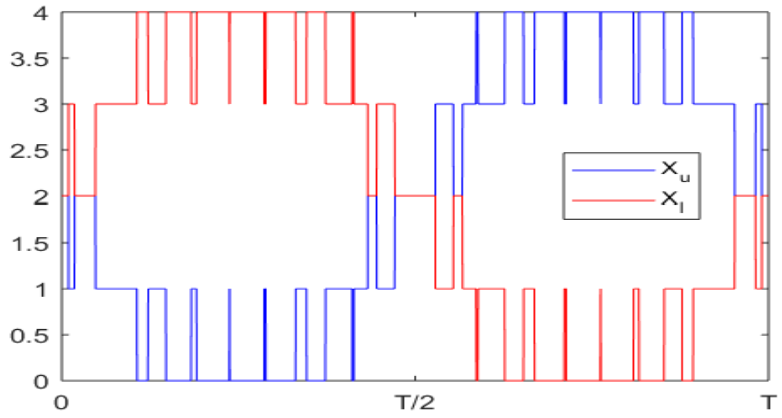

Figure 10. Insertion indices of upper and lower arms of phase-a of 5-level MMC.

B. Third-Harmonic Injection (THI) Phase Disposition

In order to increase the fundamental component of the MMC output while avoiding overmodulation, a third harmonic component can be added to the reference in the PD modulation technique [26]. In this case, introducing a third harmonic component of 1/6 peak compared to fundamental will increase the output fundamental by 15% approximately.

C. Phase Shifted Carrier-Based PWM

This technique [53] controls each SM separately. Each SM has a dedicated triangle

carrier with the same frequency, yet with a phase shift of $2\pi/(N-1)$, that is compared with the SM voltage reference. This technique improves harmonic content and controllability. The main limitations of this modulation technique are its complexity compared to the other modulation techniques and the higher switching losses.

D. Nearest Level Modulation (NLM)

This technique [55], [56] approximates the reference voltage into levels which represent the number of the SMs in each arm. Therefore, no carriers are needed and no switching frequency which reduces the switching losses and makes this technique easier to implement. This technique is only recommended with a high number of levels in order to provide a low harmonic content in the output. Figure 11 shows the *NLM* technique for a 5-level MMC, whilst Figure 12 shows the insertion indices.

2.2.5. Voltage Balancing Techniques

Following the modulation process, where the insertion indices can be determined, the role of capacitors' voltage balancing algorithms must be considered. Proper voltage balancing can be obtained by assigning the proper switching pulses to the corresponding SM in upper and lower arms. Several techniques have been proposed in literature [26], [42], [57], [58] employing both sensor-based and sensorless approaches.

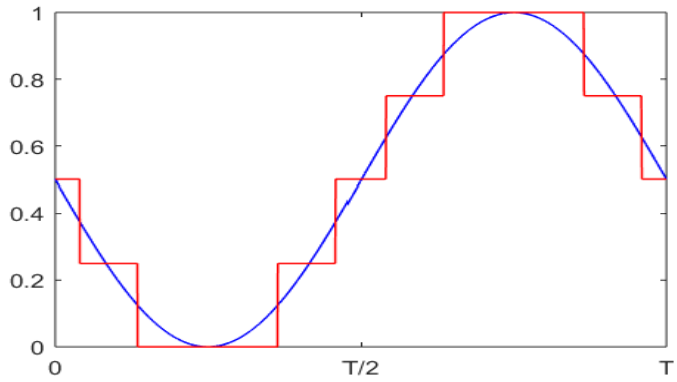

Figure 11. NLM technique of 5-level MMC.

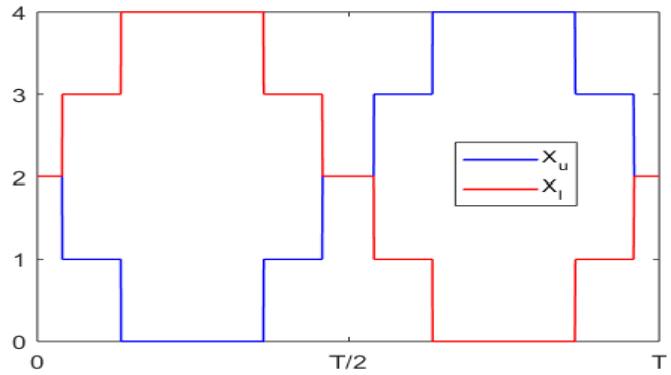

Figure 12. Insertion indices of upper and lower arms using NLM.

A. Sensor-based Balancing Approach

The most common sensor-based voltage balancing technique is based on sorting algorithms [30], [58]. The *on/off* state of each SM in the same arm is determined based on the direction of the current in the arm, the voltage level on each SM's capacitor, and the number of the required SM in each arm according to the insertion indices. Therefore, the measurements of the capacitor voltage of each SM and the arm current are essential measurements. For instance, if a new SM is to be inserted in the upper arm, then if the direction of the arm current is positive, then the algorithm will switch on the SM with the lowest capacitor voltage to charge it, and vice versa in case of negative current direction. Therefore, based on the required number of output voltage

levels, then the number of connected or disconnected SMs can be determined. The flowchart in Figure 13 depicts the applied capacitors' balancing algorithm.

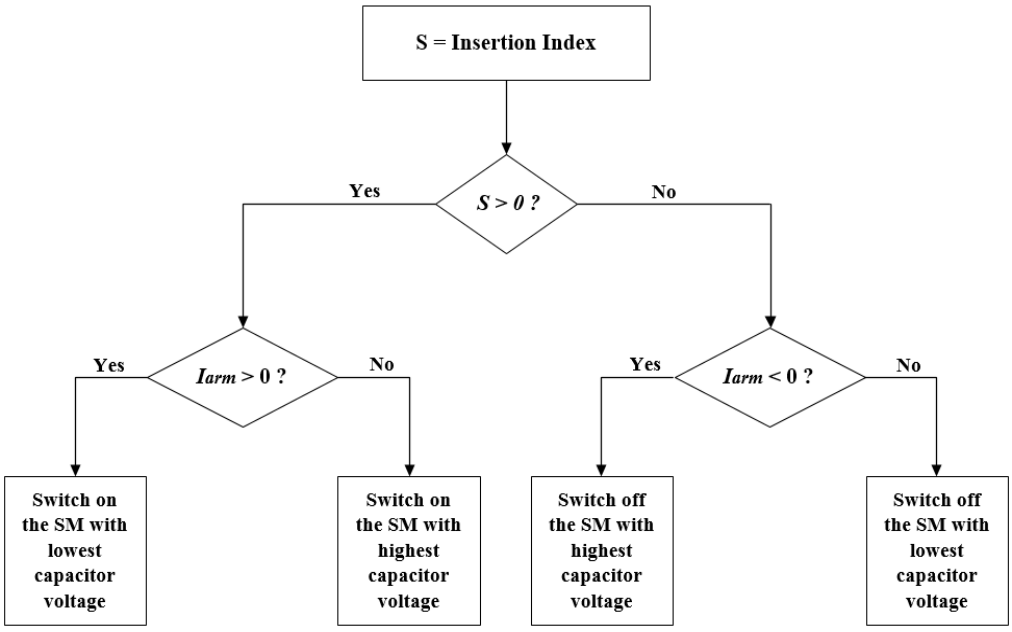

Figure 13. Sensor-based sorting algorithm.

B. Sensor-less Balancing Approach

In sensorless approaches [59], [52], enable-pulses are swapped among the arm involved switching devices each fundamental cycle in a sequence that achieves the balancing target. These pulses, for each involved SM in each arm, are extracted using any of the aforementioned modulation techniques.

For instance, in a five-level MMC, based on Figure 14(a), the upper arm voltage is compared with four carrier signal with a frequency of (f_{sw}) and displaced symmetrically along the upper arm voltage reference to generate the swapping pulses (*P1 to P4*) as shown in Figure 14(b). Based on the extracted pulses (*P1 to P4*) in each arm, and enable signals (*E1 to E4*) which are synchronized with the arm voltage reference cycles, a

software-based logic concept is implemented to obtain the sensor-less switching pattern for the presented MMC. The balancing algorithm, depicted in Figure 14(c), provides a swapping technique that ensures equal average charge on all the capacitors, hence sensor-less balanced operation.

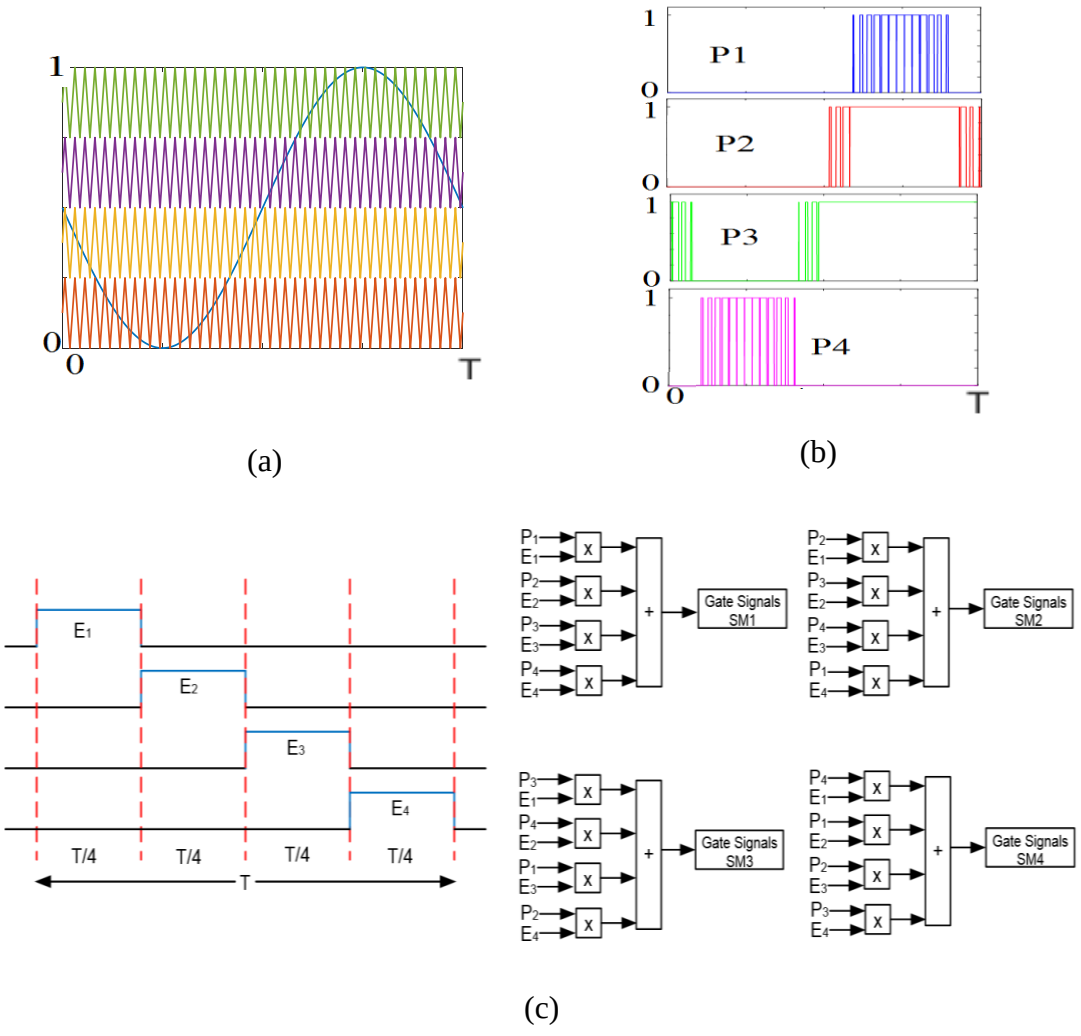

Figure 14. Sensorless voltage balancing (a) comparing upper arm voltage reference with the carrier, (b) the corresponding swapping pulses, (c) sensorless swapping technique per each arm.

2.2.6. How Conventional HB-SM-Based MMC works

Conventional HB-SM-based MMCs have no boosting capability as the peak of the generated AC voltage can be controlled up to 50% of the input DC voltage, as shown in Figure 15. In the conventional HB-MMC, each arm of the *N*-level MMC consists of *(N-1)* SMs. The capacitors of all SMs are pre-charged to $V_{dc}/(N-1)$, where V_{dc} is the input DC voltage.

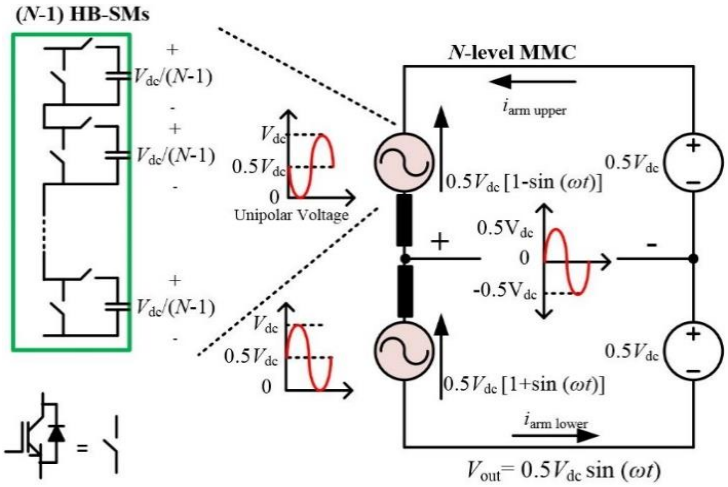

(a)

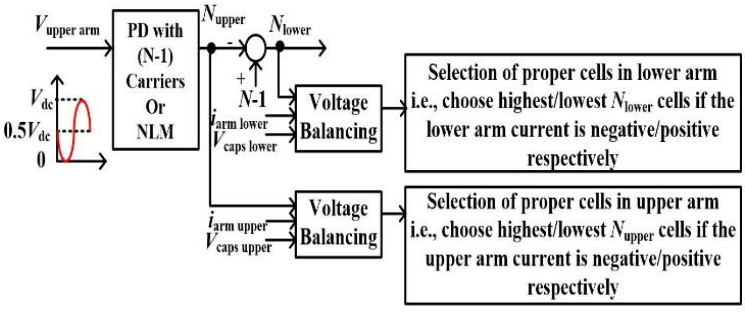

(b)

Figure 15. Per-leg basic operation of the conventional MMC at a unity modulation index (*M=1*) (a) architecture and (b) voltage balancing.

The arm voltage of the conventional MMC is controlled to generate a unipolar voltage ranging from zero to V_{dc}, which enables controlling the peak of the generated AC voltage up to $0.5V_{dc}$. The per-leg operation of the conventional HB-MMC is shown in Figure 15(a). The SMs capacitors voltages should be kept balanced by applying a proper voltage balancing technique [42], as shown in Figure 15(b). The number of involved SMs in upper and lower arms (N_{upper} and N_{lower} respectively) can be obtained using one of the aforementioned PWM techniques, such as PD, or NLM [6], [42], as in Figure 15(b).

2.3. Multiphase Machine Drives

Multiphase machines have emerged as prominent competitors to the familiar three-phase counterparts due to the evolution of Digital Signal Processors (DSPs) and power converters. A multiphase machine drive is a drive system where a machine with stator phases higher than three is used. The multiphase machine is usually supplied using a multiphase power converter. The first multiphase machine drive was introduced in 1969 when a five-phase machine was used [60]. In the late 20^{th} century, the merits of the multiphase machines started to flourish and fulfill the needs of several applications. Multiphase machine drives have provided several merits including the following:

- Fault-tolerance capabilities that ease post-fault operation without additional hardware.
- Lower torque ripples.
- Low per-phase requirements for same machine rating compared to three-phase machines.
- Additional degrees of freedom, which allows controlling flexibility when compared to three-phase counterparts.

Therefore, the high fault tolerance emerges as a salient feature of multiphase machines. Thus, multiphase machines have become the target of several industrial applications, mainly the critical ones such as aircraft actuators [61], oil and gas industry, ship propulsion systems [62], and electric vehicles [63]. The multiphase machines inevitably enhance the drive system reliability, which is crucial in high-power applications. That is, multiphase machines have become more competitive to three-phase counterparts in those applications. In both options, the machine and the converter are not commonly available in the market and needed to be designed, in addition, three phase systems require multi-parallel converters to handle the high current, which makes it easier to design a multiple three-phase machine with one stator. The additional subspaces offered by multiphase machines have been used in the literature [63] to extract operational advantages which are less feasible using conventional three-phase ASD; such as fault-tolerant operation [64], [65], motors braking [66], and fault detection [67]. Furthermore, multiphase machines produce lower torque ripples and per-phase power requirements (voltage or current) compared to similar power-rated three-phase counterparts. The most common multiphase machines comprise multiple three-phase windings or an odd number of windings which is not a multiple of three. In this thesis, the five-phase system is adopted.

In the next chapters, thesis contributions are discussed.

CHAPTER 3: ZERO-/LOW-SPEED OPERATION OF MMC-BASED DRIVE SYSTEMS

High-power motor drives in a range of tens of megawatts such as oil and gas compressors, and extra-large motors used in pumped hydro-storage are more sensitive to harmonics content, switching frequency, and energy efficiency compared to low-/medium-voltage counterparts [68]. For instance, the adjustable-speed pumped-storage generation system of the Kansai Electric Power's Okawachi Power Plant was built of 800 MW capacity, and currently, the overall capacity reached approximately 1300 MW [69]. Therefore, employing MMC in such applications can be efficient. However, the main challenge of using MMC in drive systems is the applications that require rated torque at low speed, since the SM capacitor voltage ripples are inversely proportional to the phase current frequency.

3.1. Zero-/low-speed operation of MMC-based ASDs

Investigating various possible solutions for conventional three-phase MMC-based drive systems, was the target of several works in the available literature [70]–[81] using hardware and/or software approaches.

In [70], a hardware configuration consisting of a semiconductor device in series and a snubber circuit in parallel with the DC-link are added to the MMC in order to lower the capacitor voltage ripple at low-speed operation. The topology was experimentally verified on an *RL* load, where 12% voltage ripples were obtained at 5 Hz operating frequency. Another hardware connection was proposed in [71] using a cross-connected SMs branch that connects the upper and lower arms. In [74], another cross-connected topology is proposed using FB modules connected over the conventional HB-SMs to ensure power balance among the three phases during starting. This topology was experimentally tested on an *RL* load at switching frequency of 4 kHz. In [75], MMC

IM drive was operated at rated torque and a frequency range starting above half of the nominal frequency by adjusting the circulating currents to average the capacitors voltages around the same level.

Whilst [76]–[79] use circulation current and Common Mode Voltage (CMV) to inject a current component that enables a balanced power flow between upper and lower arms. In [76], a PMSM was experimentally tested on a speed range from zero to 240 rpm, whilst in [77] a three-phase IM was employed. In [78], a five-level three-phase MMC with an *RL* load was investigated. The voltage ripples were 8% at operating and switching frequencies of 10 Hz and 10 kHz, respectively. A three-phase IM was operated from zero speed to rated speed in [79]. A circulating current of square waveform was used in [80] to reduce the current peak. Hence, the losses and arm inductor size will be reduced. In [81], the same objective was proposed using a trapezoidal current waveform. An optimized circulation current injection method was shown effective to maintain voltage ripples within defined limits while avoiding higher circulating currents [81]. In [72], the capacitor average voltage was reduced at low speeds to tolerate the ripples with the capacitor rating. In [73], a capacitor voltage control strategy was introduced based on changing the DC and AC components of the modulating signals according to the capacitor voltage level at the full speed range. A back-to-back MMC configuration has been used in [82] to drive a three-phase IM from zero up to rated speed. It connects the AC supply to the motor using an intermediate current component between both MMCs to control the machine-side MMC. These approaches involve either more hardware complexity to the system or more stresses to the converter branches due to the injected circulation current or CMV. It is worth mentioning that the starting issues of MMC-based AC-ASDs are less significant for fan and pumping loads in high-power applications, where the torque is proportional to the

square of motor speed [75], [83]. Based on the given literature, it may be concluded that either the starting or the low-frequency operation of MMC-based AC-ASD has only been achieved at the expense of extra hardware devices or complex control algorithms.

Aiming at finding a simple approach to the zero-/low-speed operation of MMC-based AC-ASDs while eliminating the need for extra hardware/software solutions, this chapter proposes an approach for multiphase machine-based drive systems. Multiphase machines possess additional degrees of freedom providing additional variables in different subspaces. For instance, an *n*-phase IM with isolated neutral possesses (*n-1*) degrees of freedom, whereas only two are required to control torque and flux. This feature means more operational flexibility. The use of MMC-based multiphase AC ASD was firstly introduced in [54]. Two series-connected three-phase MMCs were used to drive an asymmetrical six-phase IM with two series-connected DC-link capacitors. The voltage drift between the series-connected DC-link capacitors has been eliminated by controlling the secondary *x-y* current components.

In this chapter, a three-level five-phase MMC prototype is employed to drive a five-phase IM, investigating both zero-/low-frequency and full range operations including starting and steady-state. Using five-phase IM does not imply extra hardware at the same mean used for other techniques in literature. In literature, extra switching devices, snubber circuits, and back-to-back converters are installed dedicatedly to the core converter to overcome the zero-/low-frequency issues. On the other hand, a five-phase machine with a five-leg converter is already a well-established standalone system in many industries due to its advantages, mentioned above, on system performance compared to the three-phase system (regardless the converter type). The proposed system configuration is based on the conventional MMC topology shown in Figure 7.

A prototype for the entire IM-based AC drive system was built to investigate the proposed concept experimentally.

The main contributions of this work can be summarized as:

- Introducing for the first time a new technique for the starting/low-speed operation of MMC-based high-power drive systems by exploiting the additional degrees of freedom of a multiphase system.
- The proposed system eliminates extra hardware devices and complex control solutions typically used in literature.

The salient merits of the proposed technique compared to control-based techniques stated in literature can be summarized as:

- The control of the zero-/low-speed operation becomes easier, as the proposed technique uses only the output load current to perform balancing during zero-/low-speed intervals without involving the circulating current or CMV.
- It utilizes a lower number of current sensors (only the load current sensors are enough, i.e., 4 current sensors in case of five-phase IM).
- The proposed controller is designed to maintain the output current during injection periods within the machine rated current. Hence no increase in the converter rating is required.

3.2. Higher number of levels *vs.* higher number of phases of MMC-based drives

The selection of MMC number of levels is a trade-off. It is based on the required power, voltage, and the availability of switching devices. The higher the number of levels, the lower the rating of the required switching devices is. In medium-voltage drives, the required power and rated voltages are relatively high. Thereafter, either a higher number of levels or high rating switching devices are essential, providing that there are

limitations of switching devices rating. Yet, the combination of MMC and multiphase drives has been never addressed before in literature. Multiphase drives have exhibited prominent merits in medium-voltage applications such as reliability enhancement, lower per phase power requirement, and higher torque quality. For illustration, a comparison between the performance and hardware requirements of a Five-phase Three-level (*5ph-3L*) and Three-Phase Five-Level (*3ph-5L*) MMC-based drive systems is conducted in this section. The goal of the comparison is inferring that increasing the number of phases of an MMC-based drive is equivalent to increasing the number of levels of a conventional three-phase MMC drive. Yet, the multiphase system introduces lower hardware requirements in addition to the notably improved performance. The steady-state performance of both systems is investigated using MATLAB/Simulink. The comparison is carried out for two IMs with same rated phase current and MMCs' stored energy. Simulation parameters are given in Table 2 [18].

Table 2. Simulation Parameters

	IM I (3-phase)	***IM II (5-phase)***
Rated phase voltage (V)	4000	2400
Rated power (hp)	850	850
Rated torque (N.m)	4000	4000
Frequency (Hz)	50	50
Full-load phase current (A)	59	59
Rated speed (rpm)	1475	1475
Stator resistance r_s (Ω)	0.858	0.5148
Stator leakage inductance L_s (mH)	17.68	10.61
Rotor referred first component resistance $r_{r\alpha\beta}$ (Ω)	0.686	0.4116
Rotor referred third component resistance r_{rxy} (Ω)	0.36	0.216
Rotor referred first component inductance $L_{r\alpha\beta}$ (mH)	14.35	8.61
Rotor referred third component inductance L_{rxy} (mH)	7.54	4.523
Magnetizing first component inductance $L_{M\alpha\beta}$ (mH)	864.75	518.85
Magnetizing third component inductance L_{Mxy} (mH)	78.167	46.9
No. of poles	4	4
DC-link (kV)	11.333	6.8
Switching Frequency (Hz)	1000	1000

Table 3 illustrates the hardware requirements for each drive system in order to deliver the same phase current and energy stored in the capacitors. The *5ph-3L* MMC-based drive requires eight Insulated-Gate Bipolar Transistors (IGBTs) and four capacitors

fewer than the *3ph-5L* system. In this example, the IGBT rating of *5ph-3l* is slightly higher. However, increasing the number of levels will lower the rating of switching devices of the five-phase system. For instance, for a *5ph-5L* MMC, an IGBT of 1700 V rating is required compared to 1890 V for a *3ph-7L* MMC. In order to maintain equal energy storage in *5ph-3L* and *3ph-5L* MMCs, 2.4 and 2.88 mF SM capacitors are used respectively, providing that the number of the capacitors are 20 and 24, respectively. The *5ph-3L* MMC drive requires ten arm inductors of 1.8 mH, compared to six inductors of 3 mH for the *3ph-5L* MMC. Both systems require a similar number of sensors. The comparison of hardware requirements distinguishes the five-phase system as a better candidate. It requires a lower number of semiconductor switches and capacitors (representing the major cost of the converter) of the same rating compared to those used in the three-phase system approximately, as well, it already provides salient advantages such as lower torque ripples and fault tolerance capabilities. Yet, it requires a higher number of arm inductors compared to three-phase systems.

Table 3. Comparison between requirements of *3ph-5L* MMC and *5ph-3L* MMC

	3ph-5L MMC	***5ph-3L MMC***
Phases No.	3	5
Levels No.	5	3
Switching Frequency	1 kHz	1 kHz
Phase current amplitude	81 A	81 A
Phase voltage amplitude	5666.67 V	3400 V
DC link Voltage	11333.33 V	6800 V
IGBTs		
IGBTs No.	8 per arm Total = 8 x (6 arms) = **48**	4 per arm Total = 4 x (10 arms) = **40**
Voltage rating of IGBTs	2833.33 V	3400 V
Current rating of IGBTs	60 A	60 A
Total VA for IGBTs	8.16 MVA	8.16 MVA
Capacitors		
Capacitors No.	4 per arm, Total = **24**	2 per arm, Total = **20**
Voltage rating of Caps.	2833.33 V	3400 V
Capacitance value	2.88 mF	2.4 mF
Total Energy Storage	277.44 kJ	277.44 kJ
Inductors		
Arm Inductors No.	6	10
Arm Inductors	3 mH	1.8 mH
Sensors		
Voltage sensors No.	24	20
Current sensors No.	6	10
Total Number of sensors	30	30

The simulation results are shown in Figure 16. The phase currents are shown in Figure 16(a) with a THD of 6% and 4% for *3ph-5L* and *5ph-3L* MMCs respectively. The phase voltages of both systems are shown in Figure 16(b). Both comprise fifteen voltage

levels. The α-β currents are shown in Figure 16(c) and (d) with a THD of 6% and 2.7% respectively. The delivered torques are shown in Figure 16(e). The *5ph-3L* MMC system delivers lower torque ripples of 7%, compared to 11% in case of the 3ph-5L system. Figure 16 shows that *5ph-3L* MMC system exhibits improved phase currents, torque-producing currents (α-β), and torque. The capacitors voltages of phase 'a' SMs for both systems are shown in Figure 16(f). The capacitors voltage ripples in both systems are approximately the same of 2%. The MMC phase to mid-point voltages of phase 'a' is shown in Figure 16(g). The *3ph-5L* voltage consists of five levels with a voltage step of ±2833.33 V; whilst the *5ph-3L* voltage consists of three levels with a voltage step of ±3400 V. The speed is shown in Figure 16(h).

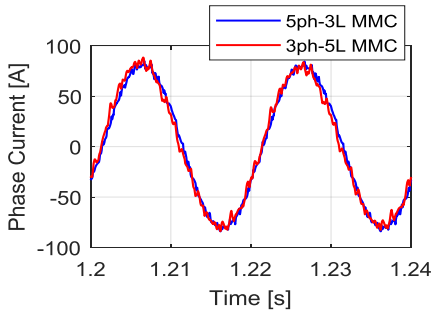

(a)

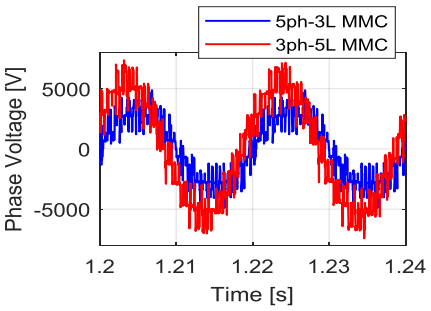

(b)

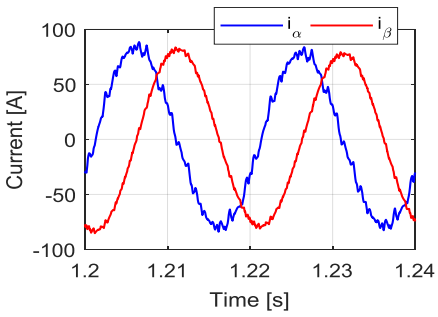

(c)

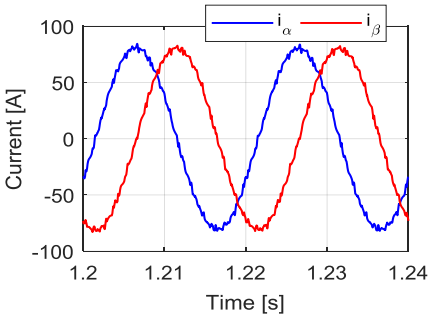

(d)

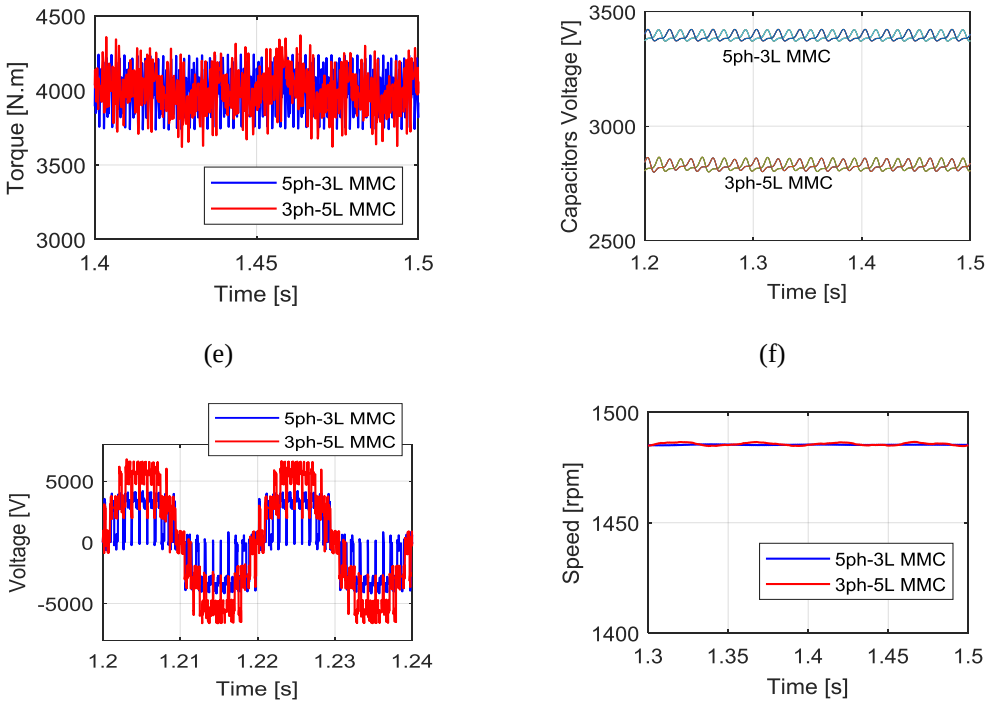

Figure 16. Simulation results. Comparison of the performance of the *5ph-3L* and *3ph-5L* MMCs, (a) phase current, (b) phase voltages, (c) *α-β* currents of *3ph-5L* MMC, (d) *α-β* currents of *5ph-3L* MMC, (e) output torque, (f) SMs' capacitors voltage, (g) phase to MMC midpoint voltages, (h) motor speed.

3.3. Effect of Operating Frequency on MMC Capacitor Voltage

In each phase of an MMC, the active power absorbed/released by upper and lower arms is responsible for charging/discharging of SMs' capacitors. Therefore, the average active power consumed by each arm must be zero to ensure balanced converter operation.

For instance, the instantaneous power, voltage, and current of an upper arm in MMC are expressed by (3.1), (3.2), and (3.3) respectively (neglecting the voltage drop on the arm inductances) [79].

$$p_{u,j} = v_{u,j} i_{u,j} \tag{3.1}$$

$$v_{u,j} = \frac{V_{dc}}{2} - v_{o,j} \tag{3.2}$$

$$i_{u,j} = \frac{i_{o,j}}{2} + i_{circ,j} \tag{3.3}$$

where V_{dc} is the DC-link voltage, $v_{o,j}$ and $i_{o,j}$ are the phase-*j* output voltage and current, respectively, and $i_{circ,j}$ is the circulating current between the DC-link and phase-*j*.

The output phase voltage and current of the proposed MMC can be expressed as (3.4) and (3.5).

$$v_{o,j} = V_m \sin(\omega t) \tag{3.4}$$

$$i_{o,j} = I_m \sin(\omega t - \varphi) \tag{3.5}$$

where V_m and I_m are the peak voltage and current, respectively, ω is the stator synchronous angular velocity, and φ is the displacement factor angle.

Assuming an input-output power balance scheme for the MMC, hence:

$$\frac{V_{dc} I_{dc}}{5} = Mean\{v_{o,j} i_{o,j}\}$$

$$= Mean\left\{\frac{V_m I_m \cos(\varphi)}{2} - \frac{V_m I_m \cos(2\omega t - \varphi)}{2}\right\}$$

$$= \frac{V_m I_m \cos(\varphi)}{2} \tag{3.6}$$

where I_{dc} is the mean of the input DC current.

Thus, the circulating current magnitude (assuming a well-suppressed double frequency component, and considering only the DC component) can be given as (3.7).

$$i_{circ,j} = \frac{I_{dc}}{5} = \frac{V_m I_m \cos(\varphi)}{2V_{dc}} \tag{3.7}$$

Therefore, the upper arm current, which indicates the SM's switching devices current

rating, is expressed as (3.8).

$$i_{u,j} = \frac{I_m \sin(\omega t - \varphi)}{2} + \frac{V_m I_m \cos(\varphi)}{2V_{dc}} \tag{3.8}$$

From (3.1), the power delivered to the upper arm can be expressed as in (3.9).

$$p_{u,j} = \frac{V_m I_m \cos(2\omega t - \varphi)}{4} - \frac{{V_m}^2 I_m \cos(\varphi)\sin(\omega t)}{2V_{dc}} + \frac{V_{dc} I_m \sin(\omega t - \varphi)}{4} \tag{3.9}$$

The voltage ripples of the arm capacitors are caused by the energy fluctuations in each arm. In (3.10), an expression for the energy stored in the upper arm's SMs can be calculated by integrating (3.9).

$$\begin{aligned} w_{SM,u,j} &= \frac{V_m I_m}{8 n_{u,j} \omega}\sin(2\omega t - \varphi) + \frac{{V_m}^2 I_m}{2V_{dc} n_{u,j} \omega}\cos(\varphi)\cos(\omega t) \\ &\quad - \frac{V_{dc} I_m}{4 n_{u,j} \omega}\cos(\omega t - \varphi) \end{aligned} \tag{3.10}$$

Hence, from the energy formula $w_{SM,u,j} = \frac{1}{2} C_{SM} V_c \Delta v_c$, the capacitor ripple voltage can be calculated as in (3.11).

$$\Delta v_c = \frac{2 w_{SM,u,j}}{C_{SM}\left(\frac{V_{dc}}{n_{u,j}}\right)}$$

$$= \frac{m I_m}{16 C_{SM} \omega}\sin(2\omega t - \varphi) + \frac{m^2 I_m}{8 C_{SM} \omega}\cos(\omega t)\cos(\varphi) - \frac{I_m}{4 C_{SM} \omega}\cos(\omega t - \varphi) \tag{3.11}$$

where $n_{u,j}$ is the number of inserted SMs in the upper arm of phase-j, C_{SM} is the capacitance of each SM, and m is the modulation index defined as ($2V_m/V_{dc}$). It is obvious that the voltage ripple is inversely proportional to the output frequency while directly proportional to the output current amplitude. Thus, in the case of zero frequency operation, the capacitor voltage ripples will theoretically be infinite. Consequently, and with the current MMC construction, the drive system cannot properly operate at zero/low frequencies. Even more, serious damage may occur to the switching devices at this low frequency range.

Figure 17 illustrates the experimental results under an operating frequency of 0.5Hz, using the employed prototype three-level five-phase MMC-based IM at a DC-link voltage of 200V. Full experiment parameters are given in Table 4 in the experimental results section. Due to the low operating frequency, the capacitors voltages of the upper/lower arms SMs, shown in Figure 17(a), significantly deviate below/above the required reference voltage of 100 V, which causes voltage ripples of 40-50%.

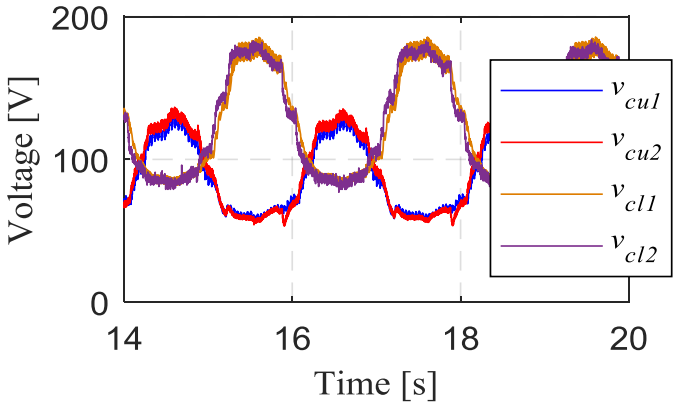

(a)

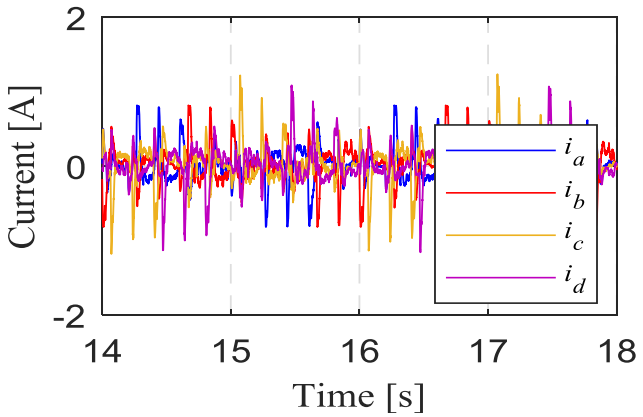

(b)

Figure 17. Experimental results of 3-level 5-phase MMC-based AC-ASD operation at 0.5 Hz. (a) All capacitors voltages of phase-*a*. (b) Output phase currents.

With this relatively high voltage ripple component, the machine line current shown in Figure 17(b) is significantly distorted. Hence the MMC fails to drive up the motor at the required conditions. Therefore, proper means of zero-/low-speed operation must be adopted with MMC-based ASDs operating at a constant load torque.

3.4. Proposed *x-y* Current Injection Concept

This section highlights the proposed role of the additional degrees of freedom of a multiphase machine in MMC-based IM ASDs. A five-phase system is employed in this study as a possible practical option.

A five-phase system comprises two subspaces, namely, fundamental torque producing (*α-β*) subspace, and a secondary (*x-y*) subspace [84]. The transformation from the time-variant variables to the decoupled space planes can be calculated using Clarke's transformation given by (3.12).

$$[i_{\alpha\beta xy}] = [T][i_{abcde}] \tag{3.12}$$

where

$$[T] = \sqrt{\frac{2}{5}} \cdot \begin{bmatrix} 1 & \cos\gamma & \cos 2\gamma & \cos 3\gamma & \cos 4\gamma \\ 0 & \sin\gamma & \sin 2\gamma & \sin 3\gamma & \sin 4\gamma \\ 1 & \cos 2\gamma & \cos 4\gamma & \cos\gamma & \cos 3\gamma \\ 0 & \sin 2\gamma & \sin 4\gamma & \sin\gamma & \sin 3\gamma \end{bmatrix} \quad \text{and } \gamma = \frac{2\pi}{5}$$

Generally, the *α-β* plane contains the fundamental current and harmonics of the order $10g\pm1$, whilst harmonics of the order $10g\pm3$ are mapped to the *x-y* plane, where *g* is a whole number (0, 1, 2, ..).

The stator and rotor voltages equations for the *α-β* and *x-y* planes are given in Appendix A [67], [85].

The torque equation can be extracted as (3.13) [67], [85].

$$T_e = C(\lambda_{\beta s} i_{\alpha r} - \lambda_{\alpha s} i_{\beta r}) \tag{3.13}$$

where $C = (\frac{5P}{4})$, and P is the number of poles.

Based on the developed torque equation, only the *α-β* subspace contributes to torque production, assuming symmetrically distributed windings. Ideally, the *x-y* current components can be considered as non-flux/non-torque producing components. Hence, the *x-y* plane features a low input impedance. This assumption, however, depends on the adopted stator winding layout [86]. Theoretically, during healthy operation, only fundamental sequence current components flow in the machine stator under zero secondary voltage components.

Since only two components are required to control the field and torque components, the remaining states will, therefore, introduce extra degrees of freedom. Consequently, and based on these decoupled subspaces assumption, the *x-y* components can be injected during either the IM starting or the low-frequency operation with a certain magnitude and frequency equal to or higher than the fundamental frequency component. This way, the deviation of SMs capacitors voltage during these periods will be avoided without affecting the machine torque production. Consequently, the *x-y* current injection will only take place during starting or at low-frequency operation in case a constant load torque is to be driven. The extra stator joule losses introduced in the system, due to the injected *x-y* current currents, are minimized by eliminating these secondary current components during normal frequency operation.

Based on the machine model, *x-y* current injection represents a simple and straightforward method while offering the following merits:

- The *x-y* plane is orthogonal to the *α-β* plane; hence, the control of both planes can independently be achieved.

- The *x-y* currents contribution to the torque production or the flux distribution can be minimized/eliminated with a proper stator winding design [86].
- The impedance in the *x-y* plane is relatively low, as it depends mainly on the machine leakage inductances [67], [85], and [87].

Fortunately, the control of *x-y* current components is already inherited in all controller structures of multiphase machines, whereas these secondary components are usually set to zero. Therefore, orienting their control towards low-frequency operation implies no additional complexity and/or notable control burden.

3.5. Proposed Multi-Phase MMC-based AC Drive Control Strategy

In the presented drive system, a five-phase IM is connected to a three-level five-phase MMC. The proposed MMC consists of a total of 20 HBs comprising 40 switching devices and 20 capacitors; in addition to 10 arm inductors (2 per each phase). As explained, a conventional MMC is not able to start an AC machine from zero speed without employing an approach for zero-/low-speed operation. Therefore, the *x-y* injection concept is adopted, as will be detailed in this section.

The block diagram of the proposed control strategy is depicted in Figure 18. The controller structure is classified into three main sub-blocks.

3.5.1. x-y Injection Control

In Figure 18(a), the control scenarios of *x-y* injection are illustrated. These control actions take place when the drive system operates at low frequencies or starts from a standstill (zero frequency). The function of the injected currents is the balancing of the capacitors at zero and low frequencies. Referring to (3.4)-(3.9), at zero fundamental frequency, the output current and voltage are constants, so are the arm voltage and current. Therefore, according to (3.9), the power delivered to the arm capacitors is constant leading to constant increase or decrease of the capacitors voltages.

As well, at low frequencies, the power delivered to the arm is almost constant with respect to the capacitors charge/discharge state.

Therefore, to avoid the imbalance at zero-/low-speed intervals, the proposed technique utilizes the additional degrees of freedom, already existing in the load current, to perform capacitor balancing hence providing the desired torque and speed without increasing the controller burden nor adding extra measurements.

These currents should be injected at relatively high frequencies around the fundamental and above. Under rated speed operation, the reference *x-y* current component will be set to zero to eliminate the losses introduced by these currents.

With this proposed concept and based on the given MMC topology, two cases are detailed:

a. With capacitor voltage measurements (Figure 18(a) bottom left): In this case, voltage sensors are used to measure the instantaneous voltage of SM capacitors. For a given phase, one of the capacitor voltages is selected from the upper arm and compared to the corresponding lower arm capacitor. The voltage error is then used to decide the magnitude of the *x-y* current components using a Proportional-Integral (PI) controller. Based on capacitor voltages difference, the controller selects the proper magnitude of *x-y* current components to ensure zero steady-state error. Targeting one capacitor per arm is only for stating the minimum requirement of employing this control technique. Using one of the capacitors in each arm should be sufficient as if two capacitors of the upper and lower arms are balanced, then consequently, the rest of the capacitors should be balanced. However, using the upper and lower average values by measuring all capacitor voltages will be more reliable, yet at the expense of more voltage sensors.

b. Without capacitor voltage measurements (Figure 18(a) upper left): In order to reduce system cost and complexity, voltage sensors may be omitted. In this case, a customized function (3.14) in terms of the fundamental *α-β* frequency and rated machine current is defined. The output of this predefined function is the magnitude of the required *x-y* current components. As a simple first assumption, this function changes the magnitude of the injected *x-y* current components inversely to the instantaneous operating frequency, such that the machine phase current will be within its rated value. At zero frequency, the function injects high frequency *x-y* current components equal to the machine rated current.

$$I_{xy}^{*}(\omega_{\alpha\beta}^{*}, i) = I_{rated}\left(1 - \frac{\omega_{\alpha\beta}^{*}}{\omega_{final}}\right) \quad (\omega_{\alpha\beta}^{*} < \omega_{final}) \tag{3.14}$$

where $\omega_{\alpha\beta}^{*}$ is the reference operating frequency, and $\omega_{final}$is the frequency at which the injection is set to zero and the desired capacitors' voltage ripples are obtained.

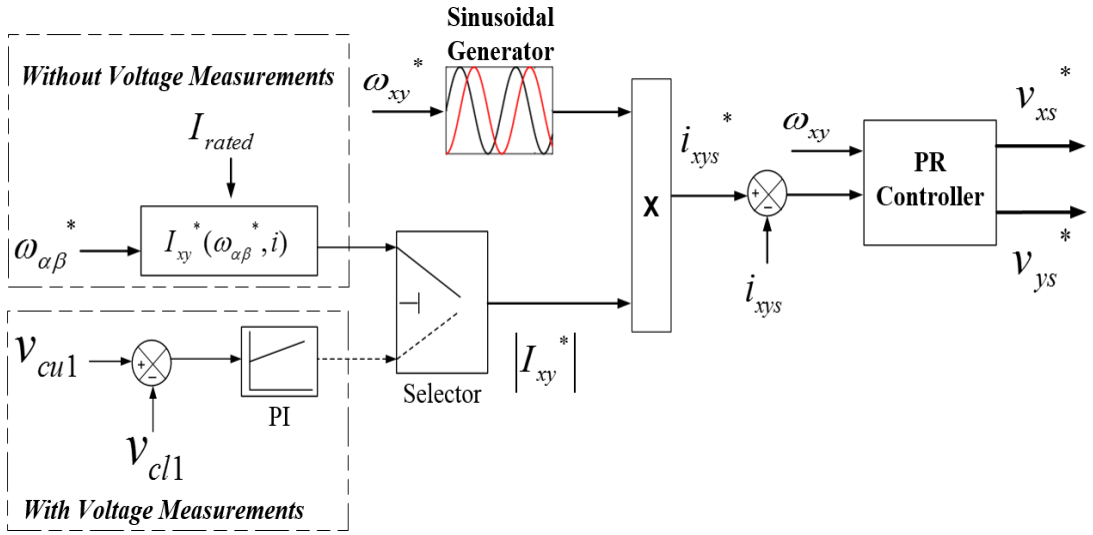

(a)

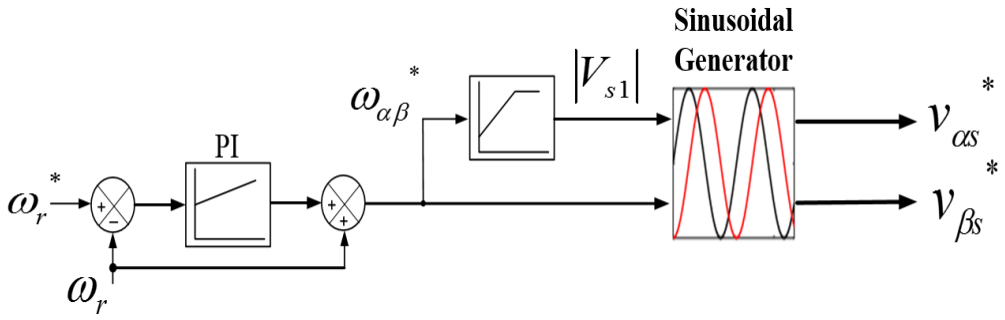

(b)

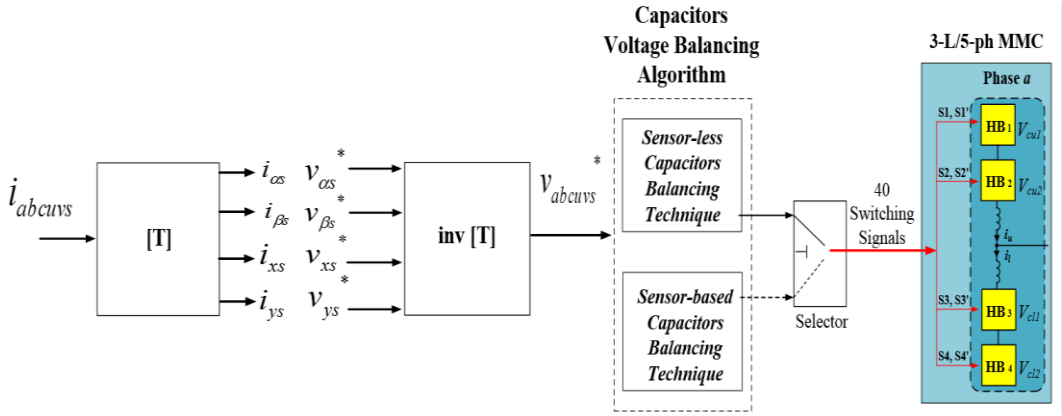

(c)

Figure 18. The overall controller of the proposed *x-y* current injection approach indicates two different control scenarios with or without voltage measurements. (a) *x-y* injection control. (b) *V/f* control. (c) Overall Schematic with capacitors voltage balancing stage.

The magnitude of the required *x-y* current components is generated using one of the two aforementioned methods then multiplied by two orthogonal sinusoidal waveforms to provide the reference *x-y* current components i_{xs}^* and i_{ys}^*. The *x-y* currents are injected at a high frequency to enable a simple capacitor voltage balancing. The frequency ω_{xy}^* of this sequence voltage component is preferably set higher than the rated frequency to avoid possible cusps and dips in the torque/speed curve produced

due to low order harmonics for slips near unity [86]. The severity of these parasitic components on the machine starting will, of course, depend on the stator winding layout as well as the speed controller adopted.

In (3.14), as the speed (frequency) reference $\omega_{\alpha\beta}^{*}$ increases, the I_{xy}^{*} decreases until reaching zero at $\omega_{\alpha\beta}^{*} = \omega_{final}$.

That is, the function enables inverse change between the *x-y* components and the fundamental operating frequency. The regulations of *x-y* current components are performed in the Stationary Reference Frame using Proportional-Resonant (PR) controllers. The PR controllers' output represents the reference *x-y* voltage components v_{xs}^{*} and v_{ys}^{*}. The expected magnitude of the *x-y* voltage components is approximated by (3.15).

$$V_{xy}^{*}(\omega_{\alpha\beta}^{*}, i) = \omega_{xy}^{*} L_{xy} I_{xy}^{*}(\omega_{\alpha\beta}^{*}, i) \tag{3.15}$$

where L_{xy} is the input inductance of the *x-y* subspace.

At a certain preset frequency ω_{final}, the injection process is quitted, and only fundamental *α-β* components are supplied to the motor. The frequency ω_{final} can be selected equal to or less than the fundamental rated frequency. The expected change in different sequence voltage components under conventional *V/f* control is illustrated in Figure 19.

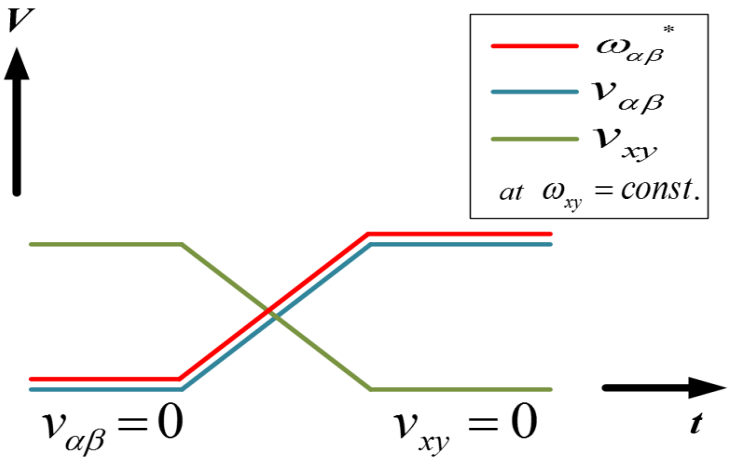

Figure 19. Illustration of the customized function in (3.14) to enable zero-/low-speed operation without voltage measurements.

3.5.2. Speed Control

Generally, the fundamental torque/flux regulation can be either carried out using scalar or vector control techniques. For high power applications, scalar *V/f* control may be sufficient and will simply be employed in this study. A speed controller is first used to provide the required slip frequency based on the machine speed error. The machine reference angular frequency can then be derived from the calculated slip frequency and the measured rotor speed. A conventional linear *V/f* control is used to produce the fundamental voltage components $v_{\alpha s}^{*}$ and $v_{\beta s}^{*}$, as shown in Figure 3.3(b). The reference phase voltages are then derived from the reference *α-β* and *x-y* voltage components by applying inverse Clarke's transformation. These reference phase voltages are then applied to the capacitors voltages balancing algorithm.

3.5.3. Capacitor Voltage Balancing Algorithm

SMs capacitors' voltage balancing is crucial in order to ensure proper operation of the MMC. An SPD-PWM sensor-based balancing technique, presented in [85], can be used in case capacitors voltages are measurable.

Whilst, a sensor-less capacitor voltage balancing technique, adopted in [59], is alternatively used in this work. Thereafter, the balancing algorithm generates the required switching control signals for different switching devices. Figure 18(c) illustrates the overall scheme of the proposed control system.

3.6. Experimental Results

A downscaled laboratory prototype of a three-level five-phase MMC-based IM drive system has been constructed for experimental validation. A photograph of the entire prototype system is shown in Figure 20. It consists of a programmable DC power supply, a three-level five-phase MMC, a 1 kW five-phase IM, a Digital Signal Processor (DSP) TMS320F28335 control unit, a speed sensor, current and voltage signal acquisition unit. The specifications of the experimental setup are stated in Table 4. One of the main advantages of MMCs is the good quality of the output waveforms at low switching frequencies, yielding low switching losses. Therefore, the employed switching frequency is set to 625 Hz. A capacitor voltage sensorless control approach is adopted in this study.

Hence, (3.14) is used to provide the magnitude of the *x-y* currents component. The experimental case studies investigate two modes of operation, namely the low-speed operation, and the motor starting, from zero up to rated speed.

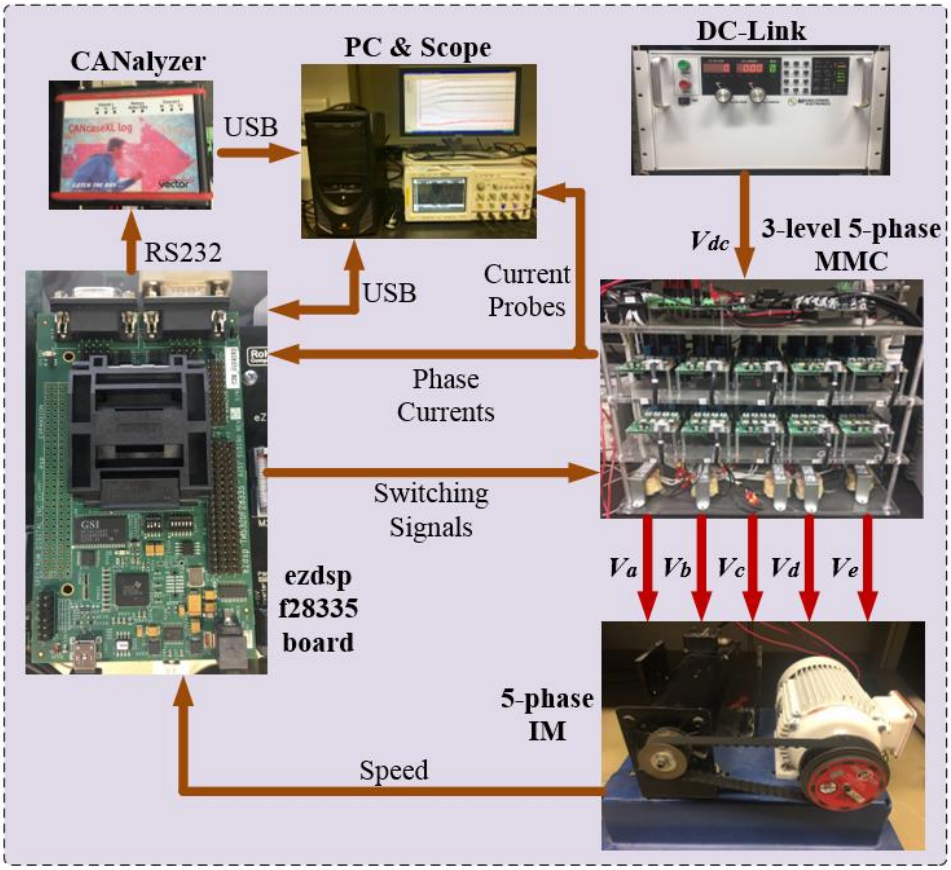

Figure 20. Experimental Prototype. The five-phase IM (bottom right) is fed through the three-level MMC and controlled using the DSP board. A DC machine (bottom left) represents the load torque.

Table 4. Specifications of Experimental Setup

IM Ratings and Parameters	
Rated phase voltage (V)	140
Rated power (hp)	1.5
Rated frequency (Hz)	50
Full-load current (A)	1.85
Rated speed (rpm)	1320
Stator resistance r_s (Ω)	9.5
Stator leakage inductance L_s (mH)	24.6
Rotor referred first component resistance $r_{r\alpha\beta}$ (Ω)	6.05
Rotor referred third component resistance r_{rxy} (Ω)	1.2
Rotor referred first component inductance $L_{r\alpha\beta}$ (mH)	36.9
Rotor referred third component inductance L_{rxy} (mH)	7.4
Magnetizing first component inductance $L_{M\alpha\beta}$ (mH)	583.3
Magnetizing third component inductance L_{Mxy} (mH)	52.6
No. of poles	4
MMC Specifications	
SM's capacitor voltage rating (V)	350
SM's capacitor (μF)	470
Arm inductor (mH)	1
IGBT IKW75N60T rating	30A/1200V
DC-link voltage (V)	300
Switching frequency (Hz)	625

3.6.1. Low-Speed Operation

In this subsection, a comparison between the low-speed operation of the drive system with and without injecting the *x-y* currents is performed. The experiment is carried out at fundamental operating frequencies of 0.5, 1, 2, and 5 Hz, and the *x-y* currents are injected at a frequency of 70 Hz, which is selected to be higher than the rated machine frequency of 50Hz.

The DC-link voltage applied for the injection method is 300V, whilst the voltage applied under no-injection operation was 200V, to avoid overvoltage stresses due to the induced high capacitor voltage ripples. The obtained capacitors voltages of phase 'a' are shown in Figure 21 and Figure 22. It is clear that the voltage ripples are high and in the range of 30-50 % as shown in Figure 21(a), (b), (c), and (d) since at low frequencies, the time required to change the state of charge/discharge of the capacitor will be relatively high. When the *x-y* current injection control method is applied, the motor was able to start smoothly at the same frequency with a low ripple content (lower than 5%), as shown in Figure 22(a), (b), (c), and (d). Figure 23 shows the upper and lower arm currents of phase 'a' while injecting *x-y* current components at 0.5, 1, 2, and 5 Hz fundamental frequencies. Figure 24 illustrates the machine currents at a fundamental frequency of 2 Hz and rated torque. Figure 24(a) shows the fundamental α-β currents whilst the *x-y* currents with a frequency of 70 Hz are shown in Figure 24(b).

Without x-y injection control ***With x-y injection control***

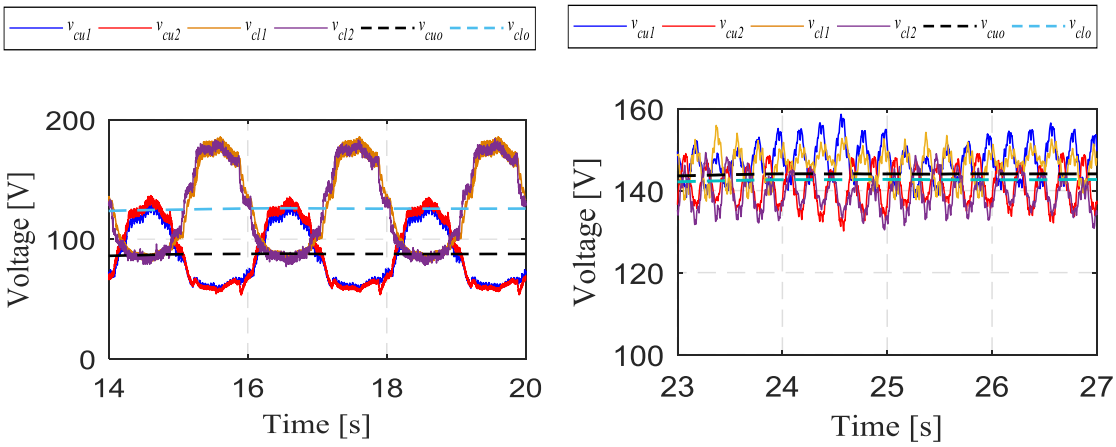

(a) (a)

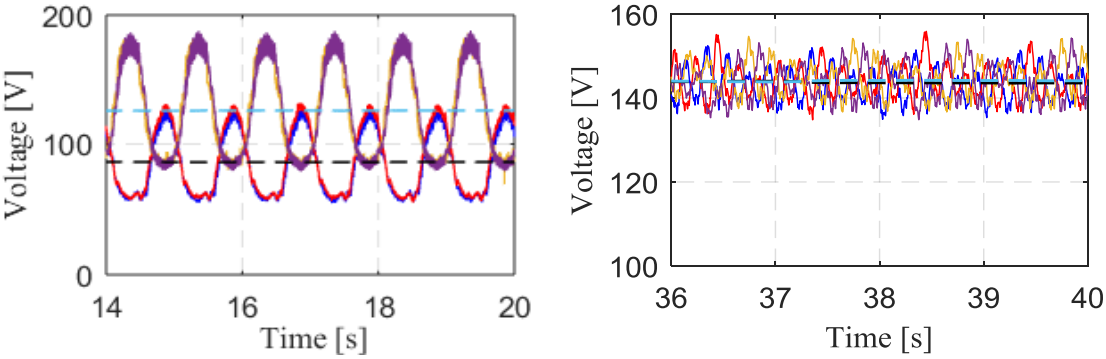

(b) (b)

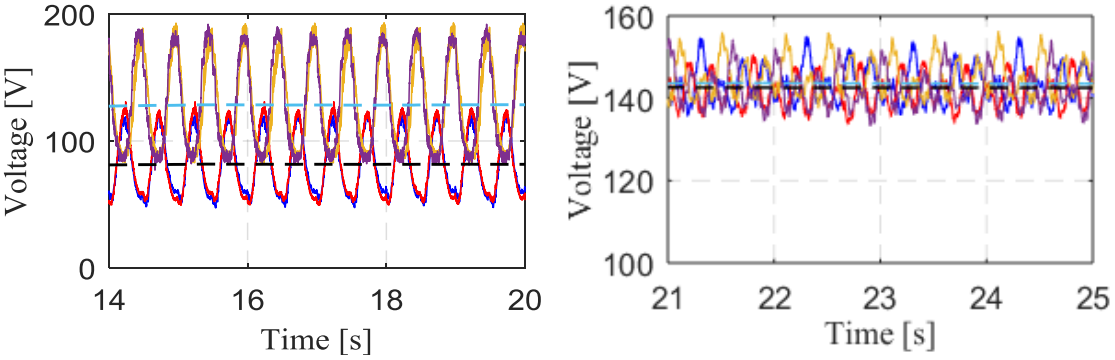

(c) (c)

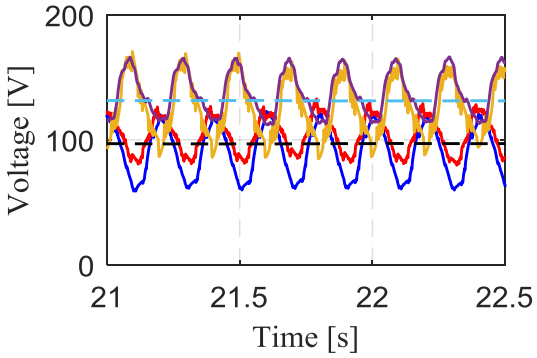

(d)

Figure 21. Experimental results of SM capacitors without the *x-y* currents injection control at frequencies: (a) 0.5 Hz, (b) 1 Hz, (c) 2 Hz, (d) 5 Hz, where v_{cuo} and v_{clo} are the average upper and lower arm voltages.

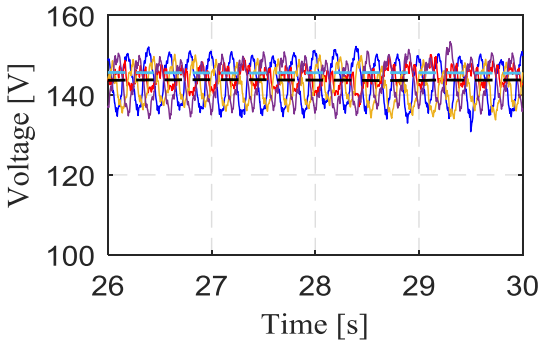

(d)

Figure 22. Experimental results of SM capacitors voltage with the *x-y* currents injection control at frequencies: (a) 0.5 Hz, (b) 1 Hz, (c) 2 Hz, (d) 5 Hz.

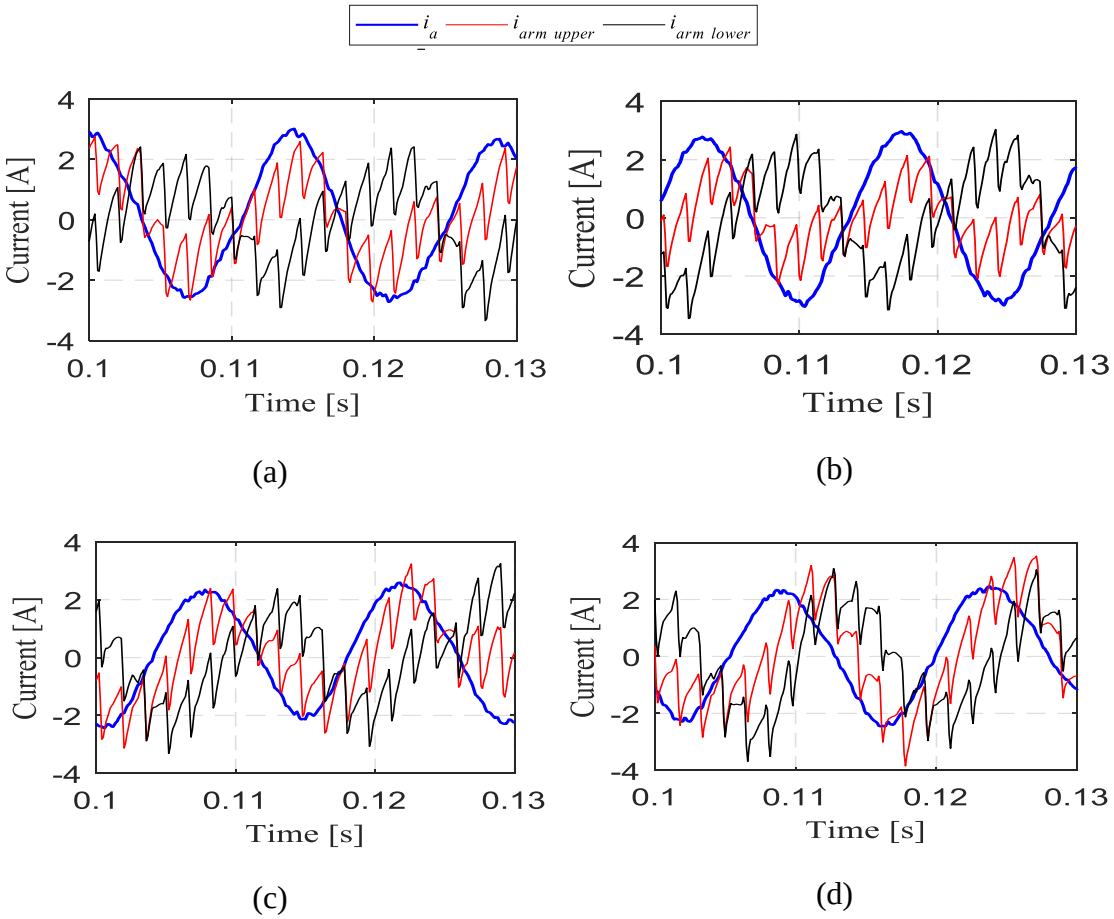

Figure 23. Experimental results of phase-*a* arm currents with the *x*-*y* currents injection control at frequencies: (a) 0.5 Hz, (b) 1 Hz, (c) 2 Hz, (d) 5 Hz.

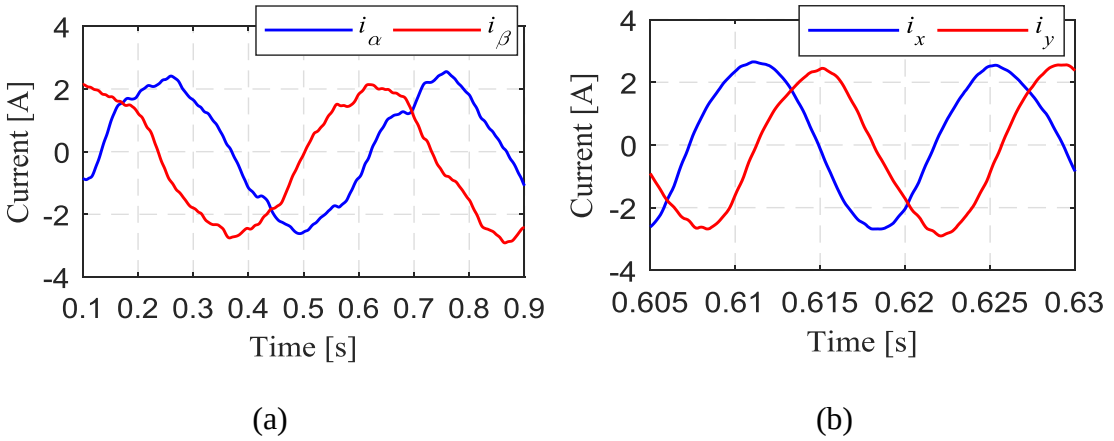

Figure 24. Experimental results of machine currents at 2 Hz fundamental frequency (a) *α*-*β* current components. (b) *x*-*y* current components.

3.6.2. Machine Starting

Figure 25 shows the system performance during starting from zero speed until reaching a steady-state speed of 500 rpm (fundamental frequency of 16.667 Hz). Figure 25(a) shows the capacitors voltages of phase 'a'. They are smoothly building up until reaching steady-state with a percentage ripple voltage magnitude of 3%. Figure 25(b) shows the RMS values of the injected *x-y* voltage components as well as the main *α-β* voltage components. At zero frequency, the controller injects high *x-y* components to enable adequate balancing of capacitors voltages, hence proper motor starting. Then, the *x-y* voltages are reduced as the capacitors voltages reaching their reference value of 150 V and the fundamental frequency, $\boldsymbol{\omega}^{*}_{\boldsymbol{\alpha\beta}}$, starts to increase. At a frequency of 16.667 Hz (500 rpm), the *x-y* voltages reach their zero steady-state values. While the fundamental frequency increases, the reference *α-β* voltages start to build up to ensure constant air gap flux until reaching their steady-state value based on conventional scalar *V/f* control.

For the given prototype, the required *x-y* voltage component was found to be relatively high due to the high impedance of this subspace with the single layer winding employed. However, this has nothing to do with the maximum converter voltage utilization since these voltage components are only presented under low-speed operation. Employing double layer stator winding designs would highly suppress this voltage component. The corresponding machine speed is shown in Figure 25(c). Figure 26 illustrates the drive system behavior at rated machine frequency of 50 Hz. The capacitors voltages of phase 'a' at steady state contain a low ripple component of 1% as shown in Figure 26(a). The control function is set to bring the *x-y* voltages to zero, at a frequency of 25 Hz, then the motor is accelerated until reaching rated frequency. The *x-y* voltages at steady-state (50Hz) are shown in Figure 26(b). The corresponding

phase currents are shown in Figure 26(c). Figure 26(d) indicates the harmonic spectrum of phase ‘a’ current at steady state condition. The corresponding THD in the phase currents is 12% at a switching frequency of 625 Hz. The steady state torque producing α-β current components are balanced at the fundamental frequency as shown in Figure 26(e). The corresponding THD presented in the α-β current components, which is more indicative in drive systems, is only 4.5% as shown in Figure 26(f), which implies lower ripple content in the steady state output torque. The corresponding steady-state *x*-*y* current components are shown in Figure 26(g), where a complete elimination to the *x*-*y* current components with simple PR current controllers tuned at fundamental frequency will hardly be obtained under this relatively low switching frequency. Employing a multiple-resonant current controller structure will highly suppress this effect. Finally, the variation of machine speed profile, according to the applied speed reference, from standstill to the rated speed is shown in Figure 26(h).

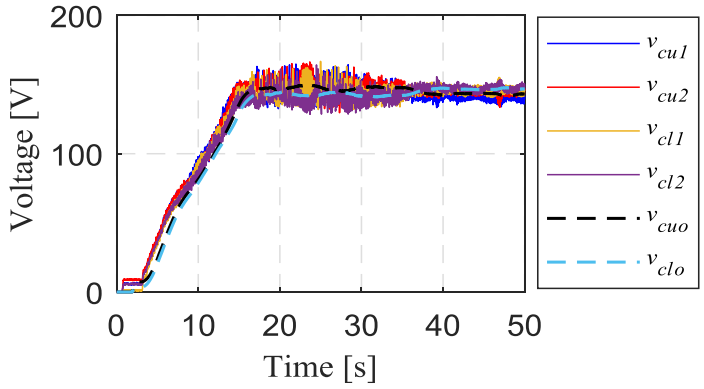

(a)

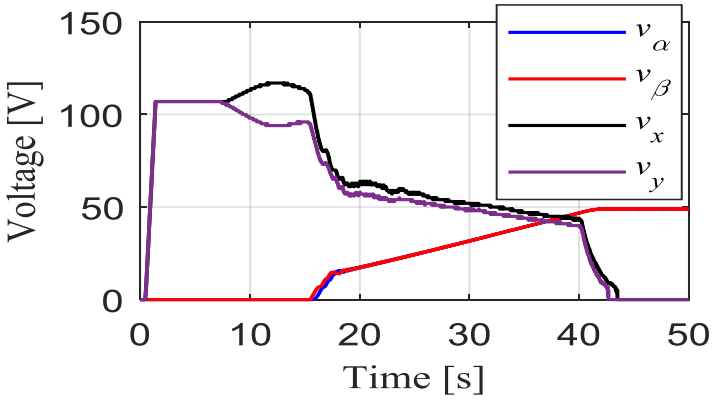

(b)

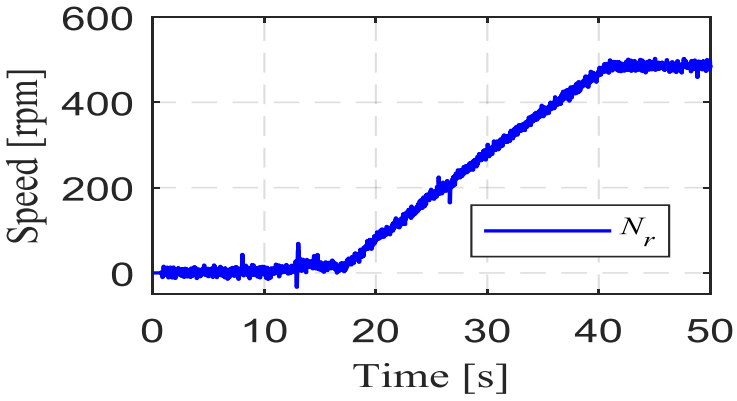

(c)

Figure 25. Experimental results of full range operation running up from 0 Hz to 16.667 Hz with constant load torque: (a) Capacitors voltage, (b) RMS values of *α*-*β* and *x*-*y* voltage components, (c) Motor speed.

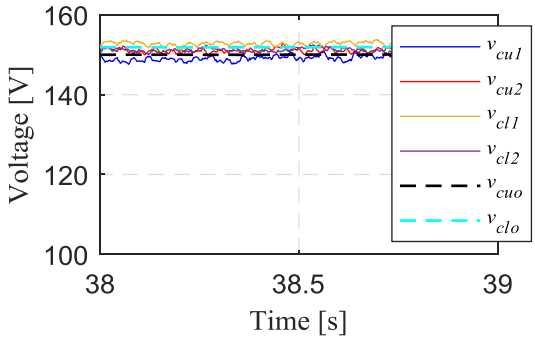
Voltage [V]
Time [s]
v_{cu1}
v_{cu2}
v_{cl1}
v_{cl2}
v_{cuo}
v_{clo}

(a)

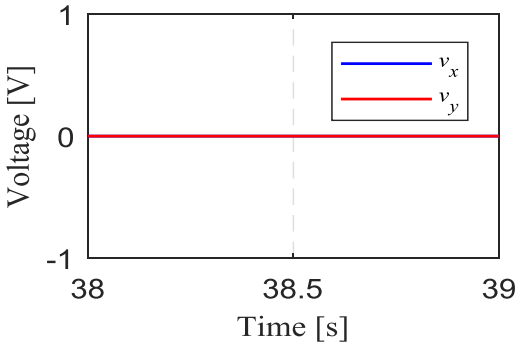
Voltage [V]
Time [s]
v_x
v_y

(b)

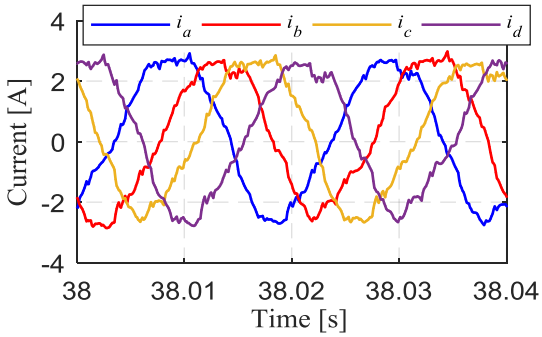
Current [A]
Time [s]
i_a
i_b
i_c
i_d

(c)

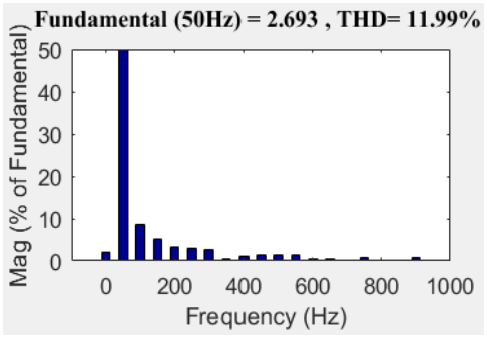
Fundamental (50Hz) = 2.693 , THD= 11.99%
Mag (% of Fundamental)
Frequency (Hz)

(d)

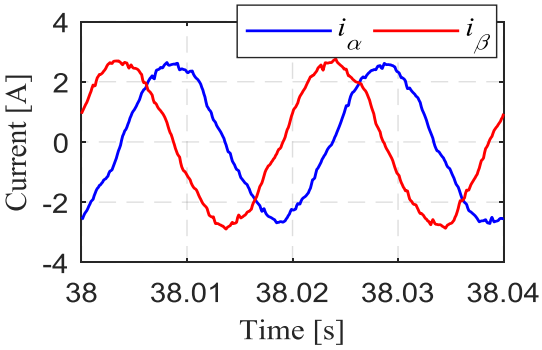
Current [A]
Time [s]
i_α
i_β

(e)

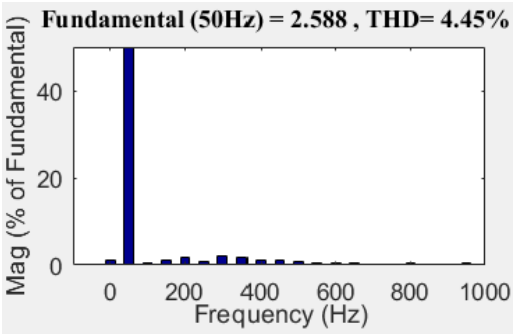
Fundamental (50Hz) = 2.588 , THD= 4.45%
Mag (% of Fundamental)
Frequency (Hz)

(f)

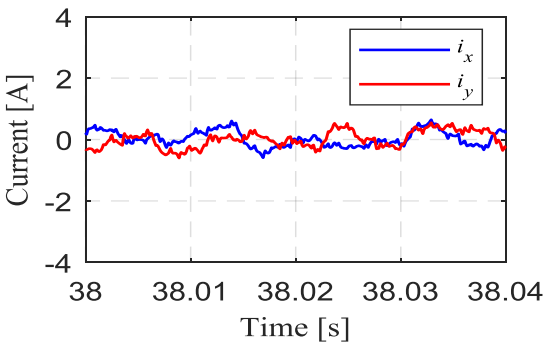

(g)

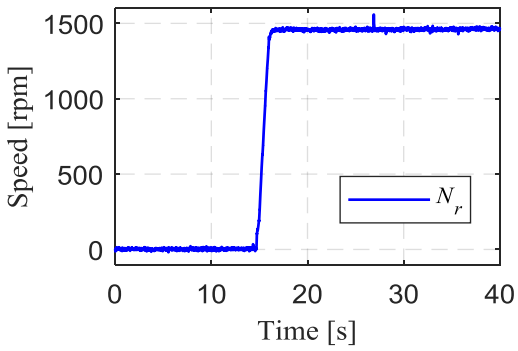

(h)

Figure 26. Experimental results of 50 Hz operation. (a) Capacitors voltage, (b) *x*-*y* voltage components. (c) Phases a, b, c, and d currents. (d) Fast Fourier Transform (FFT) spectrum of phase current. (e) Rated *α*-*β* current components. (f) FFT spectrum of *α*-*β* current components. (g) *x*-*y* current components. (h) Motor speed.

3.7. Challenges

The adopted injection technique has exhibited promising performance in the zero-/low-speed operation of MMC-based motor drives. However, the MMC is a bucking converter where a step-up transformer may be needed to interface the medium-voltage levels. Transformer operation is a challenge in certain applications such as subsea oil and gas recovery as it reduces power density and specific power, and increases footprint. This challenge is targeted in the next chapter proposing a boost MMC aiming for transformerless operation.

CHAPTER 4: HYBRID-BOOST MMC IN DRIVE SYSTEMS

As mentioned in chapter 2, in subsea medium-voltage high-power drive systems, three main system components should be considered for proper design and operation, namely the power converter, the electric machine, and the transformer.

In order to optimize drive system's technical requirements such as power density *(MW/m^3)*, specific power *(MW/kg)*, and footprint *(m^2/MW)*, a transformerless and filterless operation must be targeted.

4.1. MMCs with boosting capabilities

Boost MMCs add a stepping-up capability to the conventional MMC shown in Figure 27, yet at the cost of increasing semiconductor devices. This assists in reducing the DC-link voltage, which is a challenge in medium-voltage applications during system startup, shutdown, and normal operation. In addition, the bulky low-frequency high-power transformer may be eliminated, as shown in Figure 28 .

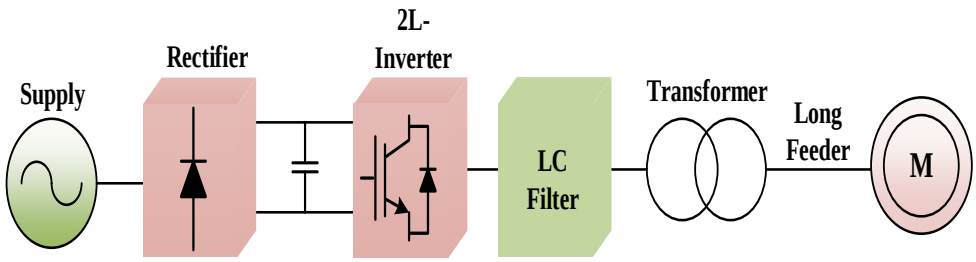

Figure 27. Conventional MMC-based AC drive system structures

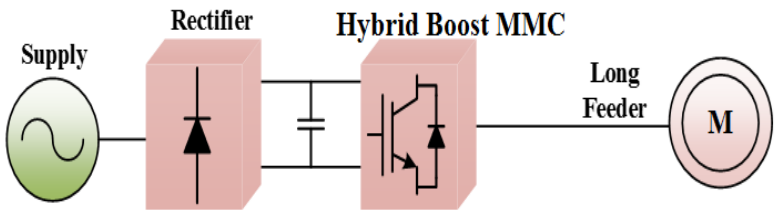

Figure 28. Proposed Hybrid-Boost-based AC drive system structures

In a boost MMC, an AC output of kV_{dc} peak, where k is a positive integer number, and V_{dc} is the input DC-link voltage, can be generated [51]; where each arm contains $(2k+1)h$ FB-SMs each rated at 0.5 V_{dc}/h, where h is a positive integer.

The voltage range of upper/lower arm is between $(0.5-k)V_{dc}$ and $(0.5+k)V_{dc}$, which results in a $(4kh+1)$-level AC output voltage with a magnitude of (kV_{dc}). On the other hand, in order to reduce the number of switching devices, a hybrid-boost MMC can be adopted. It contains a combination of $2h$ HB-SMs and $(2k-1)h$ FB-SMs per arm, i.e., a ratio of $(2k-1):2$ for the number of FB-SMs to the number of HB-SMs can be employed, respectively, to generate an AC output voltage with a peak of kV_{dc}. For example, with k=2, a ratio of 3:2 should be employed, while when k =1, a ratio of 1:2 is adopted. For simplicity, the 1:2 hybrid-boost MMC is employed throughout this chapter where AC output voltage peak of up to V_{dc} can be generated. For higher AC output voltages, other ratios can be adopted in a similar fashion. It is worth noting that operating with the aforementioned ratios results in missing the DC fault blocking capability. However, DC fault blocking feature in drive systems is not as essential as in HVDC systems, as the machine does not contribute to the fault in the DC side.

Boost FB-MMC [88] allows increasing the AC output voltage by 100%, compared to the conventional HB-SMs-based MMC, by increasing the number of employed FB-SMs by 50% (i.e., an AC output voltage peak of V_{dc} can be generated). The main disadvantage of boost FB-MMC is the employment of a large number of semiconductor devices, which affects the system cost and losses negatively.

To reduce the number of employed semiconductor devices, hybrid MMCs have been proposed with different ratios between FB-SMs and HB-SMs per arm, where 1:1 and 2:1 ratios have been presented, respectively [50], [51]. The 1:1 hybrid MMC has no

boosting capability. On the other hand, 2:1 hybrid MMC [51] can be considered as a proper replacement to the boost FB-MMC since it maintains both boosting and DC fault blocking capability yet with a lower number of semiconductor devices.

As a further reduction for the employed semiconductor devices, while keeping the boosting capability, a 1:2 hybrid-boost MMC with a combination of FB-SMs and HB-SMs with a ratio of 1:2 per arm has been proposed in [89]. The total number of SMs per arm in the 1:2 hybrid-boost MMC is $3(N-1)/4$ where N is the number of output voltage levels, and SMs are rated at $2V_{dc}/(N-1)$. The 1:2 hybrid-boost MMC can increase the utilization of DC input voltage by 100%, i.e., the peak of AC output voltage can be controlled up to V_{dc} (i.e., boosting capability).

Generally, in order to generate higher AC output voltages (up to kV_{dc}), a hybrid-boost MMC, which contains a combination of $2h$ HB-SMs and $(2k-1)h$ FB-SMs per arm each rated at $0.5V_{dc}/h$, can be employed [90].

On the other hand, with the development of power electronics, particularly when pinpointing wide-bandgap devices, enhanced efficiency, specific power, and power density can be achieved, yet the cost might be sacrificed [91]. Nevertheless, using high-voltage wide bandgap devices in high-power medium-voltage drive system applications is still in the infancy stage. However, off-the-shelf available Si semiconductor devices are limited to 6.5kV. The higher the rated voltage of the semiconductor devices, the lower is the switching capability with corresponding higher losses. For instance, a 6.5kV, 400A Si IGBT (FZ400R65KE3) from Infineon has a collector-to-emitter saturation voltage of 3V, turn-on and -off energy loss of 4250mJ, a reverse energy loss of 740mJ. While a 1.7kV, 300A Si IGBT (FF300R17ME4) from Infineon has a collector-to-emitter saturation voltage of 1.95V, turn-on and -off energy loss of 133mJ, a reverse energy loss of 41mJ. Yet, for wide bandgap devices, a 1.7kV, 300A SiC

MOSFET (CAS300M17BM2) from CREE has an *on-state* resistance of 8mΩ, turn-on and -off energy loss of 23mJ, a reverse energy loss of 41mJ. This highlights the double facet benefits of using MMC with semiconductor devices of lower voltage ratings through both increasing the switching capability, hence enhanced power quality (i.e., reduced THD), and the reduced semiconductor devices losses, hence enhanced efficiency. In addition, reducing the semiconductor devices losses positively affects the required heatsinks that enhance both power density and specific power, and reduced footprint and cost can be achieved. Increasing the number of cells in MMC may affect the reliability; nonetheless, redundancy may be seen the payback [92].

Regarding the applied machine, this chapter adopts the trend followed throughout this thesis of using multiphase machines, due to the added benefits to the system structure such as reduce the required voltage rating for the same power and phase current, when compared with three-phase based systems. This, in turn, reduces the insulation requirements. Moreover, multiphase machines, as mentioned before, enhance the reliability, fault ride through capability, power density, and reduce torque ripples, which inherently enhance the subsea drive system cost and performance.

In this chapter, a transformerless and filterless AC drive structure for subsea applications is proposed as shown in Figure 27. The proposed structure employs a 1:2 hybrid-boost five-phase MMC for simplicity (i.e., $k=1$). The same concept can be applied for higher AC output voltages (i.e., $k>1$), but with other ratios according to the aforementioned rule. The proposed system introduces the following merits:

- Reduced DC-link voltage, when compared with alternatives based on three-phase machines and/or conventional MMC.
- Enhanced efficiency, when compared with alternatives relying on other multilevel converter topologies.

- Enhanced power density and specific power, and reduced footprint.
- Enhanced reliability with fault ride-through capability.

The main contribution of this research work can be summarized as:

- Proposing a multiphase hybrid-boost MMC-based drive system for subsea applications, which enables fault-tolerant operation.
- The boosting capability of the proposed MMC enables transformerless operation in medium-voltage drives, as the boosting ratio can reach up to kV_{dc} with increasing the number of the FB-SMs. The transformerless operation, inherently, enhances the drive system utilization and reduces its weight, hence its cost.

4.2. Operational Concept of 1:2 Hybrid-Boost MMC

4.2.1. Architecture

Unlike HB-SMs, FB-SMs are able to generate a negative voltage as shown in Figure 29. The 1:2 hybrid-boost MMC (i.e., $k=1$) is shown in Figure 30. Each arm of the N-level hybrid-boost MMC consists of $(N-1)/2$ HB-SMs and $(N-1)/4$ FB-SMs; where $N=4h+1$. The capacitors of all SMs are pre-charged to $0.5V_{dc}/h$ voltage level.

In the 1:2 hybrid-boost MMC, the arm voltage is controlled to generate a bipolar voltage ranging from $-0.5V_{dc}$ to $+1.5V_{dc}$ (at highest possible output) as shown in Figure 30. This, in turn, enables controlling the peak of the generated AC voltage up to V_{dc}. During the generation of the positive part of the arm voltage, both HB-SMs and FB-SMs are used. The decision of which of these SMs should be activated is the responsibility of the voltage balancing algorithm, which will be described later. On the other hand, during the generation of the negative part of the arm voltage, only FB-SMs are used to generate negative SM voltage. Meanwhile, based on the arm current direction and the arm voltage level, a certain number of these FB-SMs will be activated.

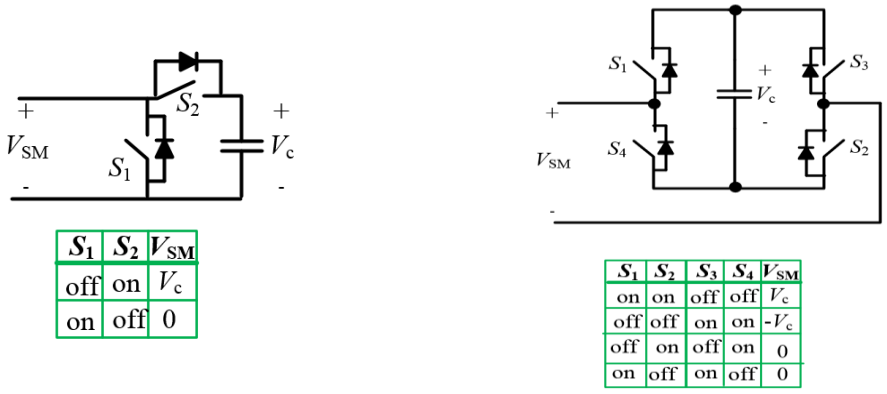

S_1	S_2	V_{SM}
off	on	V_c
on	off	0

S_1	S_2	S_3	S_4	V_{SM}
on	on	off	off	V_c
off	off	on	on	$-V_c$
off	on	off	on	0
on	off	on	off	0

(a) (b)

Figure 29. Output voltage states. (a) HB-SM, (b) FB-SM.

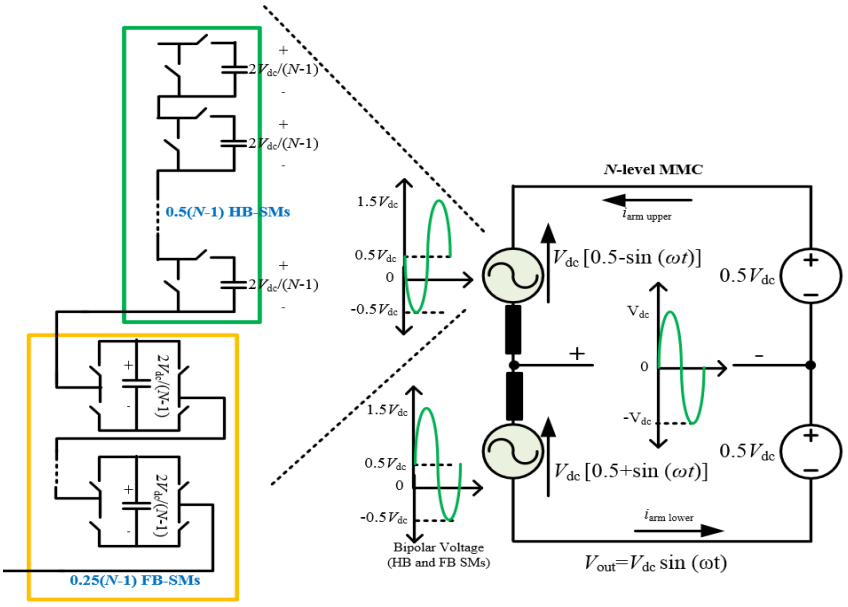

Figure 30. One-phase of the 1:2 hybrid-boost MMC.

4.2.2. Voltage Balancing Technique

A sensor-based per-leg voltage balancing technique for the hybrid-boost MMC is shown in Figure 31. A sensorless balancing technique was proposed in [59]. The procedures of the voltage balancing technique for each leg of the 1:2 hybrid-boost MMC are summarized in the following points:

- The reference of the upper arm voltage should be defined, which equals V_{dc} [$0.5-\alpha \sin(\omega t+\theta_v)$] where, α ranges from $0 < \alpha < 1$, ω is the phase angular frequency (rad/s), and θ_v is the phase angle of the AC component of the arm voltage.
- The aforementioned voltage reference is added to a DC offset of $0.5V_{dc}$ to generate a unipolar reference voltage (V_x).
- The obtained unipolar (V_x) is used to generate a signal, namely N_x, using one of the carrier-based PWM techniques such as PD shown in Figure 32(a), where $\alpha = 1$, $\theta_v = 0$, switching frequency = 2 kHz, $N = 9$, and N_x ranges from 0 to $(N-1)$.
- Then signal (N_x) can be used to extract two new variables (x and y) as shown in Figure 32(b), where $x = N_x - 0.25(N-1)$, while $y = 0.75(N-1) - N_x$.
- The absolute values of x and y represent the number of SMs to be activated in upper and lower arms, respectively (namely, N_{upper} and N_{lower} as in Figure 32(c)). The signs of x and y represent the output voltage signs of the activated SMs in upper and lower arms, respectively as in Figure 32(d).
- For positive x, both HB-SMs and FB-SMs in the upper arm are used to generate the positive part of the upper arm voltage, i.e., highest/lowest $N_{upper(+)} (= x)$ SMs will be selected, if the upper arm current is negative/positive, respectively.
- For negative x, only FB-SMs in the upper arm are used to generate the negative part of the upper arm voltage, i.e., highest/lowest $N_{upper(-)} (= |x|)$ FB-SMs will be selected, if the upper arm current is positive/negative, respectively.
- For positive y, both HB-SMs and FB-SMs in the lower arm are used to generate the positive part of the lower arm voltage, i.e., highest/lowest $N_{lower(+)} (= y)$ SMs will be selected, if the upper arm current is negative/positive, respectively.
- For negative y, only FB-SMs in the lower arm are used to generate the negative part of the lower arm voltage. i.e., highest/lowest $N_{lower(-)} (= |y|)$ FB-SMs will

be selected, if the lower arm current is positive/negative, respectively.

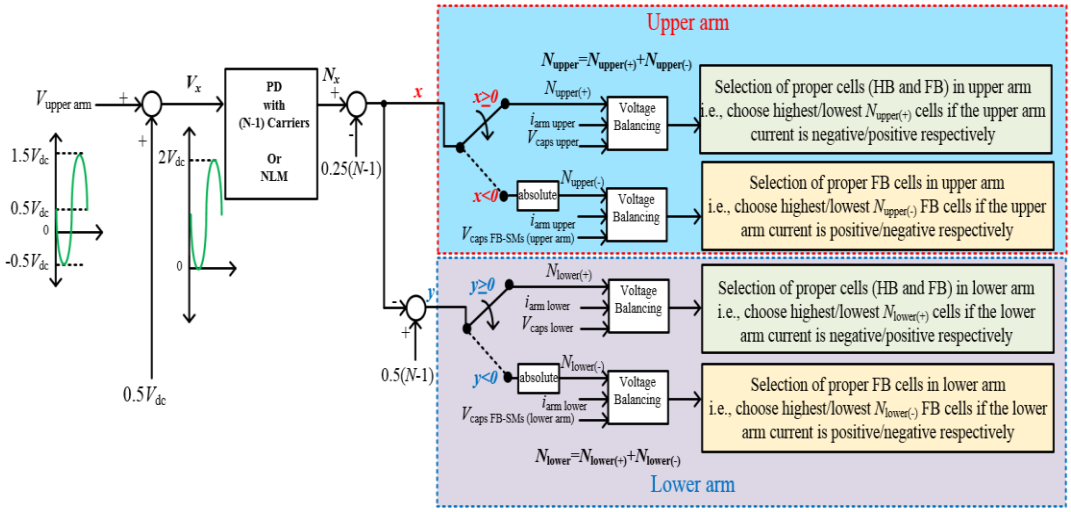

Figure 31. Per-leg voltage balancing technique of the 1:2 hybrid-boost MMC architecture.

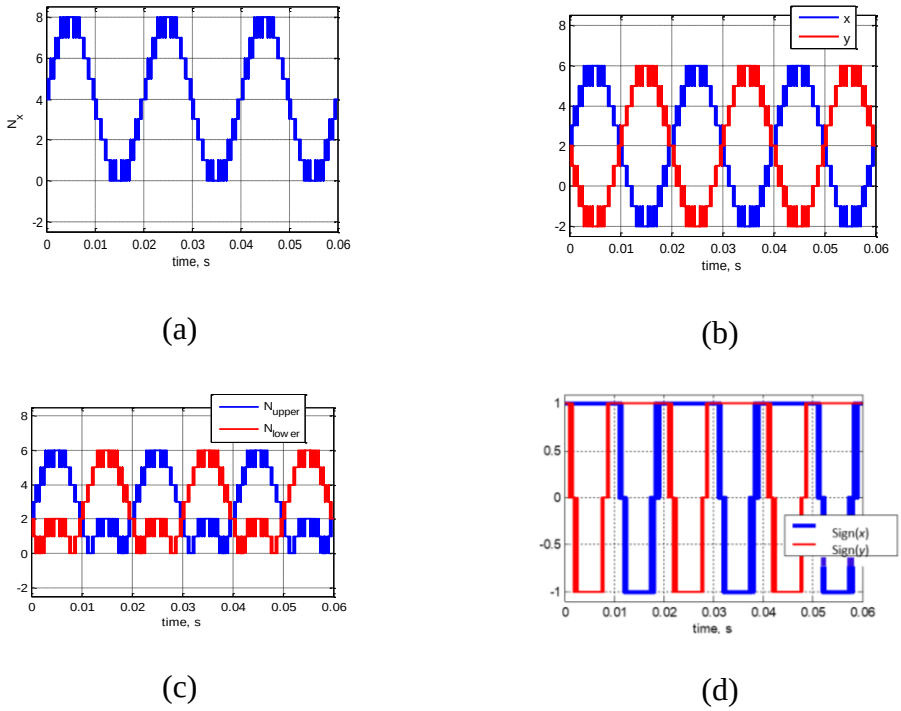

(a) (b)

(c) (d)

Figure 32. Illustration of the voltage balancing procedures (a) the signal N_x, (b) the signals x and y, (c) the number of the involved SMs in upper and lower arms, and (d) the signals sign(x) and sign(y).

4.3. Effect of Five-Phase Motor Power Factor on the Capacitors' Voltages Balancing

Assuming an ideal five-phase converter, the average DC-side and AC-side powers in the proposed approach are given by (4.1) and (4.2) respectively.

$$P_{dc}=I_{dc}V_{dc} \tag{4.1}$$

$$P_{ac}=(5\ I_m V_m\ cos(\varphi)/2) \tag{4.2}$$

where V_{dc} is the input DC voltage, I_{dc} is the mean of the input DC current, and I_m and V_m are the peak of load phase current and voltage, respectively. While $cos(\varphi)$ is the motor power factor, and the voltage of phase 'a' is given by (4.3).

$$v_{ph}(t) = V_m\ sin(\omega t) \tag{4.3}$$

By equating (4.1) and (4.2) and substituting with $V_m=V_{dc}$ (i.e., assuming the highest output voltage in the proposed structure), the mean of the input DC current can be expressed by (4.4).

$$I_{dc} = 2.5 I_m \cos(\varphi) \tag{4.4}$$

The following analysis is presented for the upper arm, where similar procedures can be applied to the lower arm. If the circulating currents are well suppressed, the upper arm current of phase 'a' can be expressed by (4.5).

$$i_{arm\_u}(t) = 0.5 i_{ph}(\mathrm{t}) + 0.2 I_{dc} \tag{4.5}$$

Substituting from (4.4) into (4.5) yields:

$$i_{arm\_u}(t) = 0.5 I_m[\cos(\varphi) + \sin(\omega t - \varphi)] \tag{4.6}$$

The corresponding upper arm voltage reference of phase 'a' can be expressed as in (4.7).

$$v_{arm\_u}(t) = 0.5 V_{dc} - V_m \sin(\omega t) \tag{4.6}$$

which ranges from $-0.5V_{dc}$ *to* $+1.5V_{dc}$. When $-0.5V_{dc}<v_{arm\_u}(t)<0$, FB-SMs are only operated to generate negative output voltage state. Meanwhile, the arm current direction

determines the charging/discharging of the FB-SMs capacitors for negative or positive upper arm current, respectively. Furthermore, when $0<v_{arm\_u}(t)<1.5V_{dc}$, adequate SMs from HB-SMs and/or FB-SMs will be operated based on the balancing algorithm to generate a positive output state.

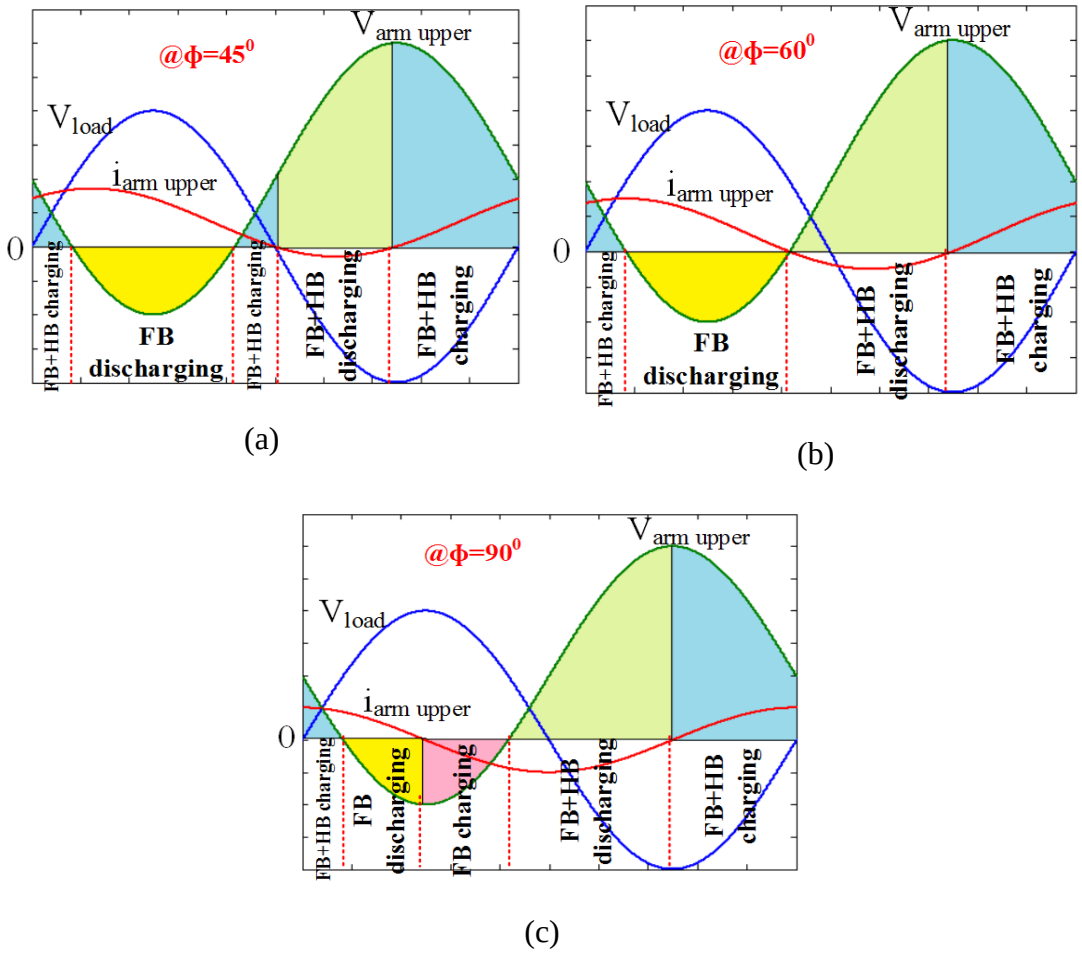

Figure 33. Illustration of the effect of the load power factor on the charging and discharging periods of SMs capacitors: (a) ϕ=45º, (b) ϕ=60º, and (c) ϕ=90º.

Similarly, the arm current direction determines the charging/discharging of the HB-SMs and/or FB-SMs capacitors. The variation of upper arm current and voltage during a complete fundamental cycle for different load power factors, along with an illustration for charging and discharging periods of FB-SMs and HB-SMs with the operation is shown in Figure 33. It is clear that as load angle increases, the area of the negative upper arm current increases, which increases the possible time for discharging HB-SMs. In case of low negative upper arm current area, the discharging time interval for HB-SMs will be insufficient, which results in a mismatch in the voltages of FB-SMs and HB-SMs.

4.4. Performance of 1:2 Hybrid-Boost MMC-Based Medium-Voltage Five-Phase IM Drive

The configuration of the proposed drive system is shown in Figure 34. Referring to Figure 30 in the presented case study, a five-level five-phase *1:2* hybrid-boost MMC with (*N=5, k=1,* and *h=1*) is used to feed a five-phase IM.

In the presented case study, the employed five-phase hybrid-boost MMC contains 80 switching devices distributed as 4 HB-SMs and 2 FB-SMs per each phase (upper and lower arms). The aforementioned voltage balancing technique is utilized for each leg of the converters to ensure a successful operation with balanced capacitors voltages. Meanwhile, the five-phase IM fosters system reliability and fault tolerance.

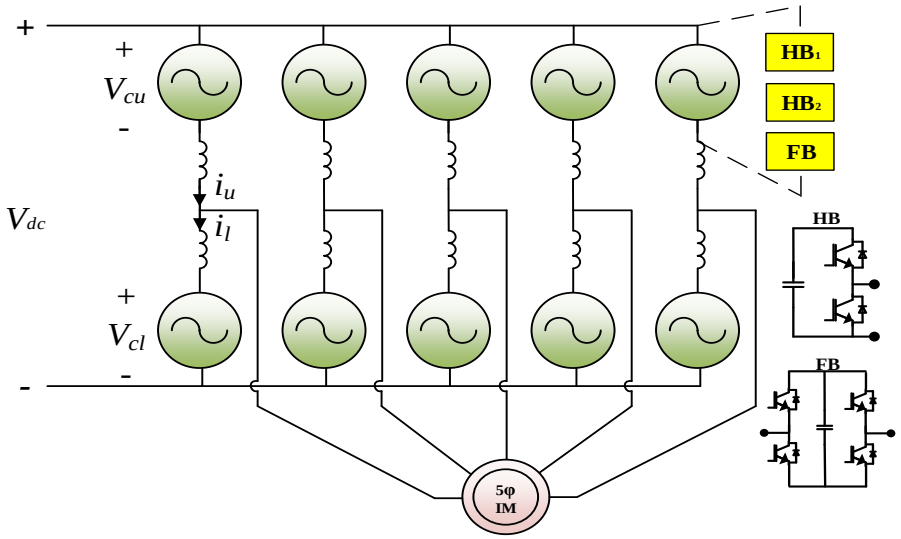

Figure 34. *1:2* hybrid-boost MMC-based multiphase IM drive system.

4.4.1. System Simulation

In this section, the drive system performance during steady-state operation is investigated using Matlab/Simulink. *V/f* scalar control is used to drive the machine at the rated operating conditions. A simulation model for the *1:2* hybrid-boost MMC-based medium-voltage drive with an 850 hp five-phase distributed winding IM has been built with the parameters shown in Table 4.

The five-phase IM's model equations can be found in [67]. Based on the data shown in Table 4, to generate the IM rated phase voltage (peak=3.394 kV) from the *1:2* hybrid-boost MMC, a DC-link voltage of 3.4 kV is employed. The machine is started at no-load at $t = 0$; then a load torque is applied at $t = 1s$. The simulation results are shown in Figure 35, assuming 2 kHz carrier switching frequency.

Table 5. Simulation Parameters

DC-link voltage (kV)	3.4
IM rated phase voltage (kV)	2.4
IM rated phase current (A)	59
IM rated power (hp)	850
Fundamental frequency (Hz)	50
No. of poles	4
FB-/HB-SM's capacitor (mF)	1
IM rated torque (N.m)	4000
IM stator resistance (Ω)	0.5148
IM stator leakage inductance (mH)	10.61
IM rotor referred resistance(Ω)	0.4116
IM rotor referred inductance (mH)	8.61
Magnetizing inductance (mH)	518.85

The machine planes are mapped into two main orthogonal frames; *α-β* frame, and *x-y* frame; in addition to the zero-sequence frame. The *α-β* frame represents the electromechanical energy conversion, while the *x-y* frame represents the harmonics/losses plane.

Figure 35(a) shows the delivered phase-to-midpoint voltages, which have a peak value equals the input DC voltage (V_{dc}). With *N=5*, i.e. *h=1*, in the simulated *1:2* hybrid-boost MMC, the output voltage consists of five different voltage levels (-1, -0.5, 0, 0.5, 1) V_{dc}.

Figure 35(b) shows the capacitors voltages balanced around $0.5V_{dc}$ (generally, $2V_{dc}/(N$-

1)). The difference between the FB-SMs and HB-SMs voltages is caused by the unequal charging/discharging times of both modules according to the load power factor, as illustrated in Figure 33. The stator phase currents are balanced and identical as shown in Figure 35(c). The $i_{s\alpha}$ and $i_{s\beta}$, which are responsible for the torque production, are shown in Figure 35(d). The output torque is shown in Figure 35(e) that exhibits a percentage torque ripple of only 2.25% at this relatively low switching frequency. Figure 35(f) shows the machine speed. Even though MMC eases low switching frequency operation, the torque ripples remain a concern for drive systems.

Figure 36 shows the torque ripple profile at different switching frequencies to conclude a range for the minimum permissible operating switching frequency that yields acceptable percentage torque ripple. With changing the frequency of the carrier responsible for assigning the number of required upper and lower SMs, the output torque ripple magnitude changes accordingly.

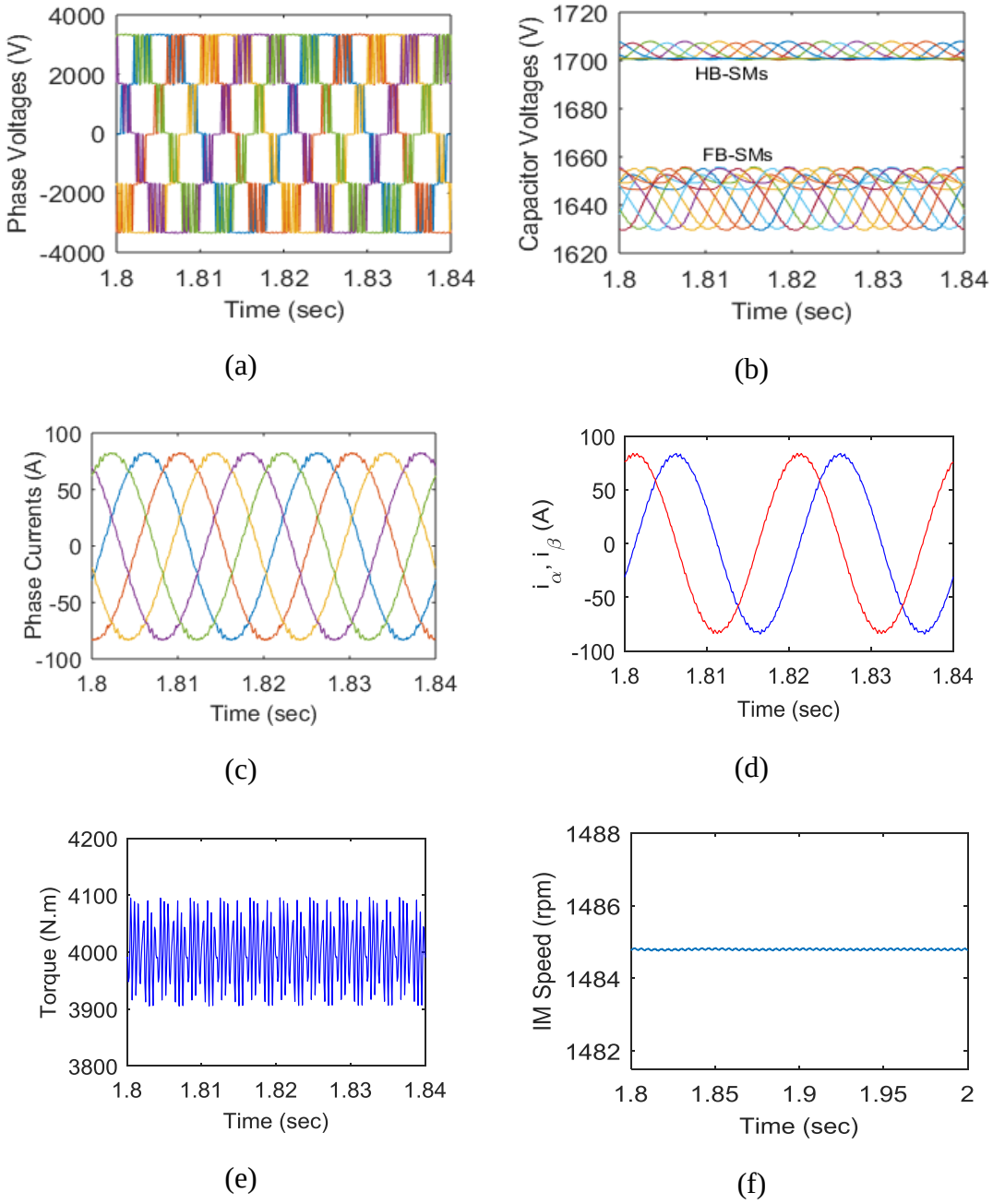

Figure 35. Simulation results at steady-state operation: (a) MMC output phase-to-midpoint voltages, (b), capacitor voltages, (c) machine phase currents, (d) fundamental $\alpha\beta$ currents, (e) machine torque, and (f) machine speed.

Figure 36 shows the output phase current components, and the corresponding delivered torque at different switching frequencies. With a carrier frequency of 10 kHz, the output

current has the lowest harmonics with the lowest i_{sx} and i_{sy} components and torque ripples of barely 1%. For a carrier frequency of 2 kHz, ripples in the $i_{s\alpha}$ and $i_{s\beta}$ components increased to 1.7%, hence in the torque.

Yet, the torque ripples are still acceptable of 2.25%. When the carrier frequency is dropped to 1 kHz, the stator currents are more distorted as shown in Figure 36(c), which can be deduced from the i_{sx} and i_{sy} components. The current THD is increased to 8.3%. However, the torque ripples are just 3% due to the lower presence of the harmonics in the torque producing components $i_{s\alpha}$ and $i_{s\beta}$. The currents THD and torque ripples at different switching frequencies are summarized in Table 5.

It is worth noting that the torque ripples are significantly less than the ripples obtained when the simulation was performed using a conventional five-phase two-level converter, as shown in Figure 37.

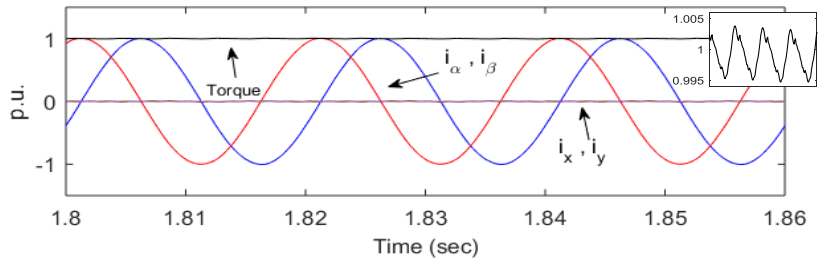

(a)

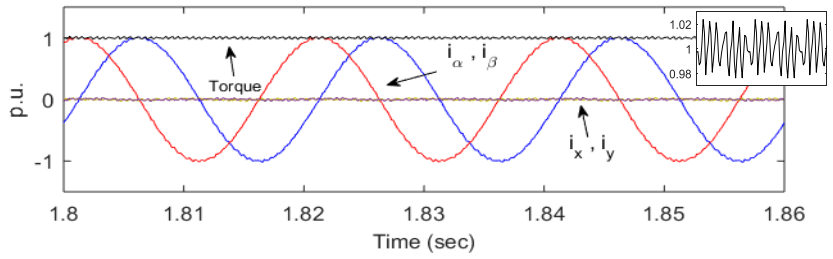

(b)

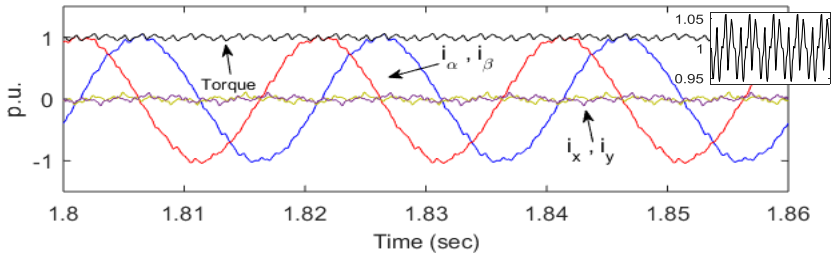

(c)

Figure 36. Effect of carrier frequency on the stator currents and delivered torque ripples (per-unit values): (a) f_s=10 kHz, (b) f_s=2 kHz, and (c) f_s=1 kHz.

Table 6. Torque Ripples and THDs with Switching Frequency Change

	f_s= 0.5 kHz	***f_s=1 kHz***	***f_s=2 kHz***	***f_s=10 kHz***
Torque ripples %	14.6	3	2.25	0.4
THD phase currents %	17.68	7.6	2.4	0.8
THD αβ currents %	10.7	3.4	1.7	0.37

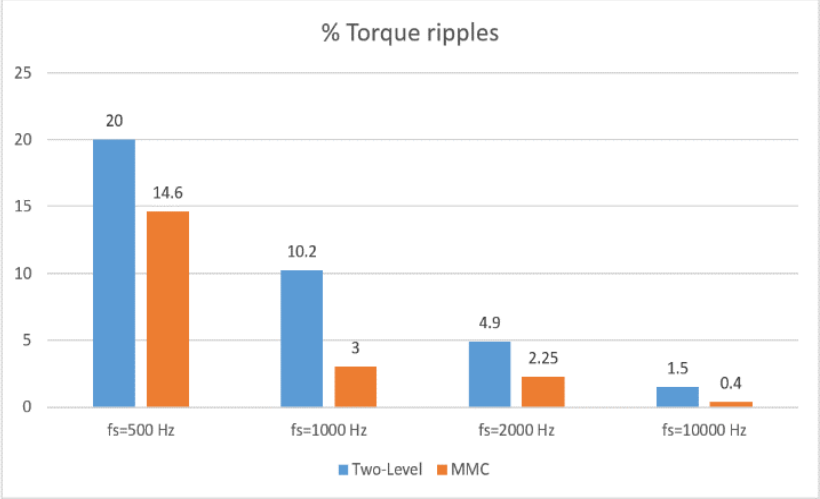

Figure 37. Generated ripples in the output torque of Hybrid-Boost MMC vs. conventional 2L inverter with the change of switching frequency.

4.4.2. Experimental Validation

A downscaled experimental single-phase prototype has been built to validate the proposed topology. For simplicity, a single-phase 5-level *1:2* hybrid-boost MMC is applied to a single-phase inductive load with low inductance value, as the experiment is performed at the worst-case scenario for capacitors' voltage balancing of approximately a unity power factor.

Figure 38(a) shows the schematic diagram of the experimental rig where the capacitors voltages and arms currents are measured, then fed to the DSP to perform the aforementioned suggested voltage balancing technique (Figure 31) for the given output voltage reference. Figure 38(b) shows the implemented experimental rig. Table 6 illustrates the experimental setup specifications.

Table 7. Experimental Setup Parameters

SM's capacitor voltage rating (V)	350
FB-/HB-SM's capacitor (μF)	470
Arm inductor (mH)	1
DC-link applied voltage (V)	200
IGBT IKW75N60T rating	30A/1200V
Switching frequency (Hz)	1000

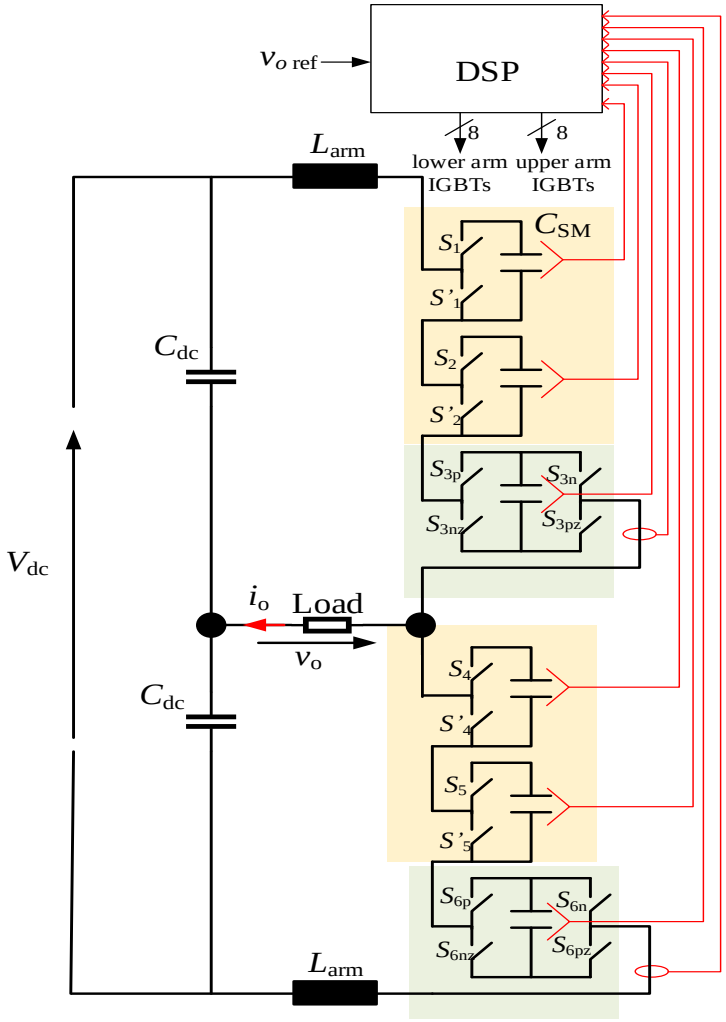

(a)

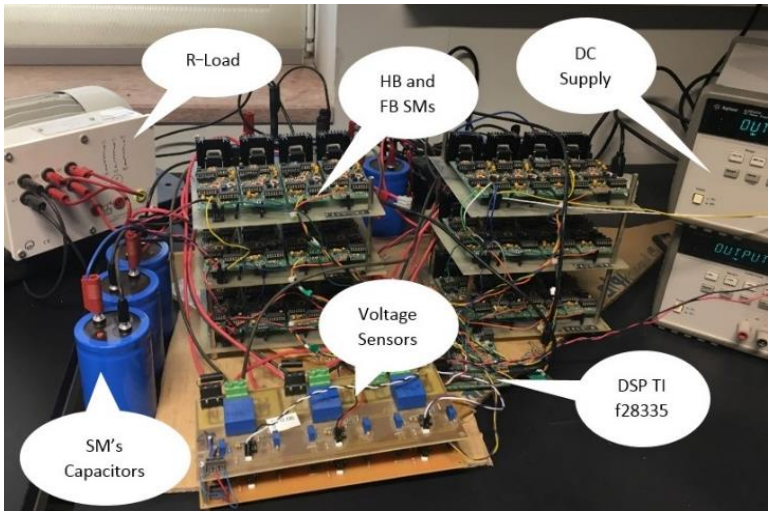

(b)

Figure 38. Experimental validation: (a) schematic diagram, (b) experimental rig.

The experimental results are shown in Figure 39 where SPD-PWM is used to generate the number of SMs to be included in each arm. As shown in Figure 39(a), the *1:2* hybrid-boost MMC delivers an output voltage of 5-level with a peak value approximately equal to the DC-link input, with a voltage drop due to the *on-state* resistance/voltage of the applied IGBTs. The upper arm voltage is shown in Figure 39(a), it is clear that it consists of four levels of five different voltage levels *(-0.5, 0, 0.5, 1, 1.5)*V_{dc}.

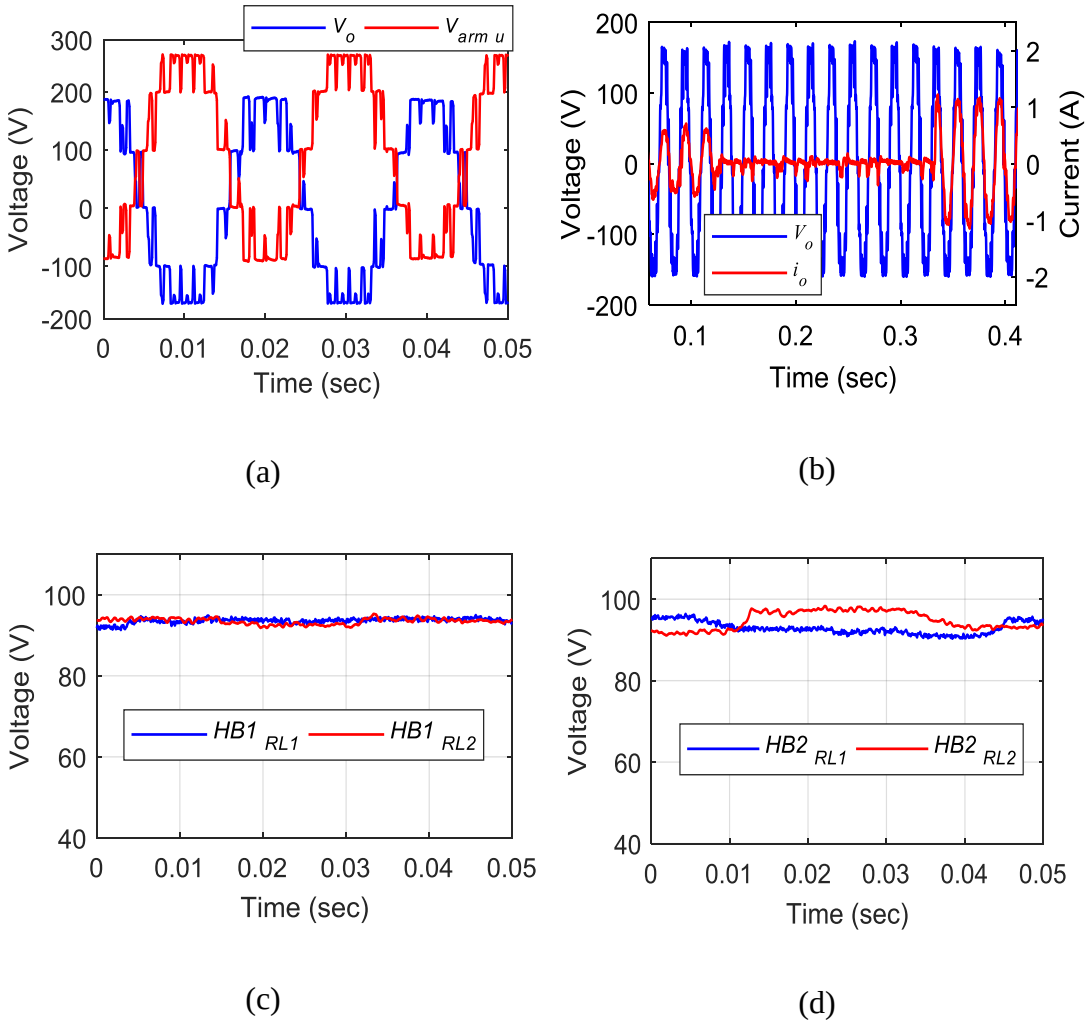

Figure 39. Experimental results: (a) output and upper arm voltages, (b) output voltage and current with load change, (c) capacitor voltage of HB_1 (d) capacitor voltage of HB_2, at two different loading conditions R_{L1}=290Ω and R_{L2}=155Ω.

The output voltage and current, when the load is changed from $RL_1=290\Omega$ to open circuit to $RL_2=155\Omega$, is shown in Figure 39(b). The current magnitude at 290Ω load is approximately 0.6 A; while it equals 1.1 A at 155 Ω.The capacitors voltages of two different HBs, namely HB_1 and HB_2, are shown in Figure 39(c) and (d) with loading change from RL_1 to RL_2, respectively. The capacitors' voltages are balanced, in both cases, fluctuating around $0.5V_{dc}$. The obtained experimental results support the

proposed topology where an MMC with boosting capability is validated with a reduced number of FBs.

4.5. Challenges

The conventional sinusoidal based modulation techniques provide good harmonic content in output waveforms. However, there is no room for torque enhancement using SPD-PWM without over-modulation. Therefore, a new modulation technique for MMC-based drive systems is proposed in the following chapter. The proposed modulation technique ensures torque enhancement with acceptable harmonic content in the output waveforms and lower switching losses compared to SPD-PWM.

CHAPTER 5: TRAPEZOIDAL PHASE DISPOSITION PULS WIDTH MODULATION FOR MMC-BASED AC DRIVES

5.1. Introduction

Capacitors energy variation in MMCs affects its operation markedly. Thus, the balancing techniques have been studied in [42], [57], [58]. Curtailment of MMC switching losses is another challenge, particularly for high-voltage/power applications. In literature, various techniques to reduce switching losses in MMC were proposed. In [93], selective harmonic elimination was proposed to enhance the quality of the output waveforms at lower switching frequencies. The discontinuous PWM technique was adopted in [94]. A hybrid approach of PD-PWM and Fundamental Frequency Modulation (FFM) was applied in [95]. Quasi two-level (Q2L) modulation was proposed in [96] to reduce switching frequency. As well, Q2L for an MMC-based high power transformer was proposed in [97]. A trapezoidal modulation waveform was studied in [98] for less *dv/dt* stresses in MMC-based DC-DC transformers.

In the same context, multiphase IMs have salient advantages over the three-phase counterparts such as fault tolerance capability, better power distribution per phase, and higher torque capability with lower torque ripples [67], [87]. They provide additional degrees of freedom, in the form of fundamental and secondary subspaces, which enhances control flexibility. Although multiphase machine with multiple three-phase winding is widely employed, five-phase IMs were mainly addressed in literature for their torque enhancement capability without additional hardware components. That has been carried out using a selected harmonic injection. The injected harmonics are selected based on the desired air-gap flux distribution [99]-[100]. In five phase IMs, the fifth harmonic is inherently omitted. If a third harmonic current, mapped to the

secondary subspace, is injected to a five-phase IM, then the fundamental flux component is enhanced with approximately 15%. Hence, a gain of approximately 10% is expected in the output torque for the same rated RMS line current [100].

The objective of this chapter is to describe the operation of MMC-based five-phase IM-based ASD under Trapezoidal Phase Disposition PWM (TPD-PWM). This technique replaces the stereotype sinusoidal reference voltages using a typical trapezoidal waveform. Under TPD-PWM, the ASD operates with enhanced output torque. Meanwhile, the output's THD is minimized. This, in essence, means an increase in the drive system's efficiency and reduction of the hardware requirements and costs. Trapezoidal modulation has been proposed in literature for several purposes [28]-[33]. Reference [101] has shown that trapezoidal modulation is capable of improving the converter's output signal by increasing fundamental and reducing harmonics. In [102]-[103] a modified trapezoidal modulation technique has been used to improve PMSM torque quality and reduce power loss of the VSC in HVDC offshore wind farms, respectively. The trapezoidal modulation was proposed for current source converters as well in [104]. It was used in DC-DC and AC-AC converters in [104]-[105] respectively. In [106], the trapezoidal modulation was applied for MLCs.

The main contribution in this chapter is the optimization of the enhanced output torque simultaneously along with the output THD through optimizing the trapezoidal reference slope angle δ (rising time t_r). The utilization of traditional Third Harmonic Injection (THI) technique in order to achieve the same goal, with the same hardware, is divisive. That is, the THI must be implemented at relatively high switching frequencies. Thereafter, for high-scale applications, significant switching losses will likely occur. Moreover, torque enhancement is more flexible with TPD-PWM due to the higher fundamental amplitude and with fewer low order harmonics than THI.

Employing a trapezoidal reference in high voltage-/power-MMC-based multiphase ASDs yields the following advantages:

- Optimum flattened-top flux distribution, inherited by the waveform construction.
- Torque enhancement, as the trapezoidal waveform comprises larger fundamental amplitude.
- Switching losses reduction, as no switching needed during the steady flat period of the trapezoidal signal.
- Better harmonic content in the output, through controlling the rising time of the trapezoidal reference.
- Simple algebraic implementation of the reference.

5.2. The proposed modulation scheme

The proposed modulation is based on conventional SPD-PWM [54]. A trapezoidal waveform, of an amplitude A_m ranges between 0 and 1 and frequency f_m, is used as a modulation signal instead of a sinusoidal waveform [107]. The intersection between the trapezoidal reference and *(N-1)* triangle carriers of a switching frequency f_s, defines the number of the inserted SM in upper and lower arms. Figure 40 illustrates TPD-PWM for a 5-level MMC, where $A_m = 1$. Then, based on those numbers, the sensor-based and sensorless voltage balancing techniques for SMs' capacitors can be adopted.

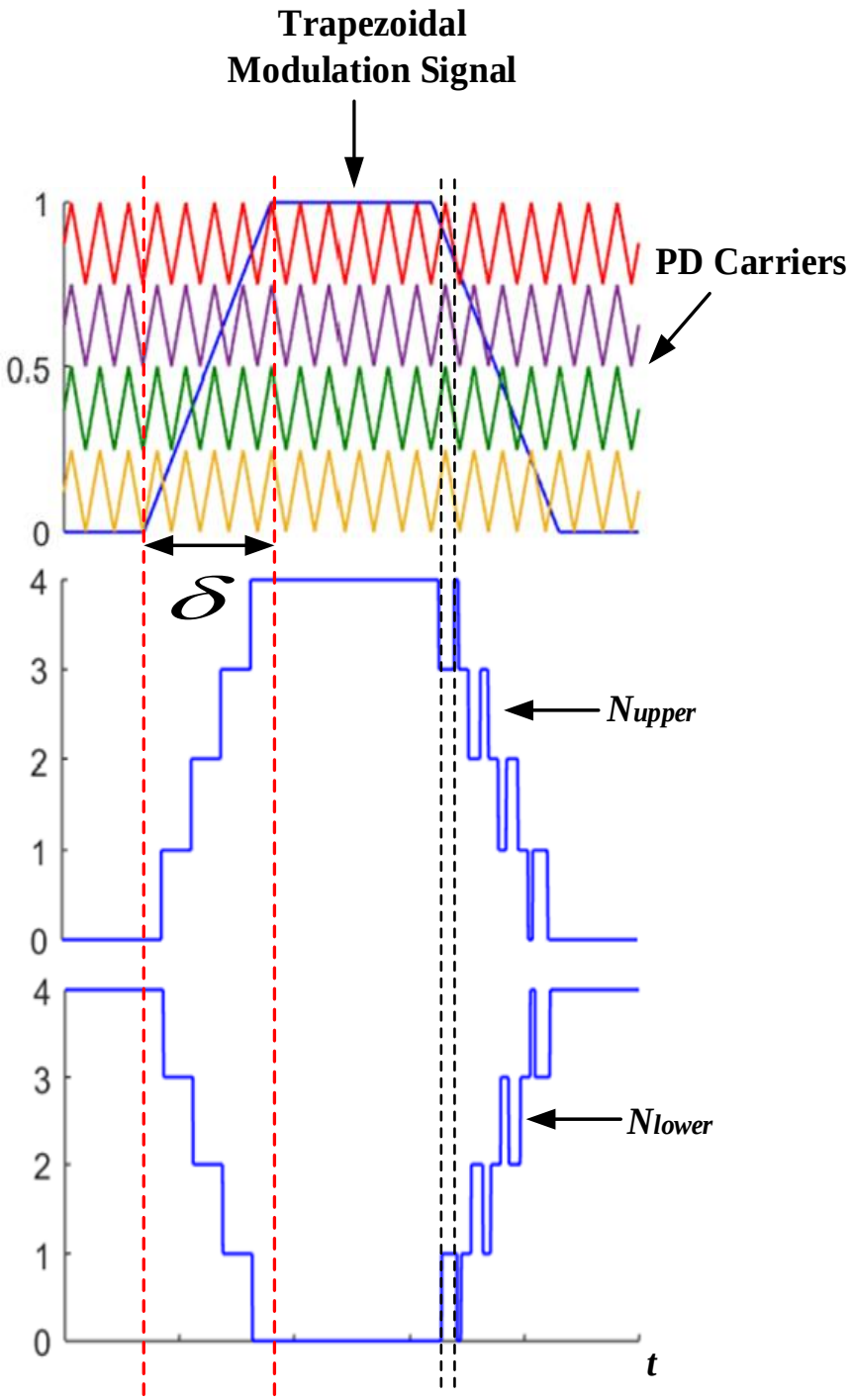

Figure 40. Trapezoidal PD PWM technique.

The balancing technique is responsible for producing the required gating signals for SMs' semiconductors.

The trapezoidal waveform is characterized, in this work, by its slope angle δ. Change of δ leads to a variation in the trapezoidal waveform shape. If δ is zero, then a square waveform is obtained, and more harmonic content exists; whilst a δ of 90° results in a triangle waveform with lower harmonic content. Therefore, the change of δ will lead to different harmonic content of the modulation signal, hence the output signals.

The magnitude of harmonic order *n* for a trapezoidal waveform, with δ ranging from 0° to 90°, can be obtained using Fourier series.

Based on the trapezoidal waveform symmetry, even terms of the Fourier expansion can be neglected considering only odd terms. The Fourier coefficients of *n*-harmonic of a trapezoidal waveform can be expressed as (5.1).

$$A_n = \frac{4}{\pi}\int_0^{\frac{\pi}{2}} F(\theta)\sin(n\theta)\,d\theta \tag{5.1}$$

where $F(\theta)$ represents the trapezoidal waveform.

For A_m = 1, $F(\theta)$ can be expressed as (5.2).

$$F(\theta) = \begin{cases} \dfrac{\theta}{\delta} & 0 < \theta < \delta \\ 1 & \delta < \theta < \dfrac{\pi}{2} \end{cases} \tag{5.2}$$

Then, an expression for (1) can be reformulated as (5.3).

$$A_n = \frac{4}{\pi}\int_0^{\delta} \frac{\theta}{\delta}\sin(n\theta)\,d\theta + \frac{4}{\pi}\int_{\delta}^{\frac{\pi}{2}} \sin(n\theta)\,d\theta \tag{5.3}$$

Hence, from (3), A_n can be expressed as (5.4).

$$A_n = \frac{4}{\pi}\frac{\sin(n\delta)}{n^2\delta} \tag{5.4}$$

Clearly, selecting δ towards zero increases the fundamental yet increases the THD. Therefore, in order to increase the motor torque, δ may be controlled towards zero, seeking higher fundamental amplitude, while maintaining a reasonable THD. By

eliminating a number of dominant harmonics, output signals with high fundamental and lower harmonic content can be easily generated. In five phase machines, the fifth order harmonic cannot flow. Therefore, a $\delta = 25.7°$ is believed to deliver the best THD as, according to (4), it eliminates the first dominating harmonic after the fifth, which is the seventh harmonic. In this chapter, a study for the best slope angle δ that yields higher torque enhancement at lower THD is performed. TPD-PWM technique is suitable for multiphase machines where some of the harmonics are mapped to a different subspace (x-y space) than the torque producing subspace (α-β space). Hence, the THD of $\alpha\beta$ torque producing current components is usually better than the phase currents. This feature does not exist in conventional three-phase machines where the phase currents are the same as torque producing components (α-β currents).

5.3. Machine Model and Control

This five-phase machine model is illustrated in Chapter 3. The Speed control is based on the scalar *V/f*.

5.4. Simulations

TPD-PWM is simulated for five-phase three-level MMC-based IM drive system using MATLAB/Simulink. The simulation case study verifies the proposed modulation technique investigating two different machine models, namely 1.5 hp and 850 hp with low- and medium-voltage, respectively. The machines' parameters and ratings are given in Table 7. Simulation models of the proposed machines have been built. First, the effect of changing the trapezoidal modulating signal's slope angle δ on the torque production is studied. Then, a simulation case study for changing δ at the full-load torque is introduced.

Table 8. Simulation Parameters

	IM I	***IM II***
Rated phase voltage (V)	140	2400
Rated power (hp)	1.5	850
Rated torque (N.m)	6	4000
Frequency (Hz)	50	50
Full-load current (A)	1.85	59
Rated speed (rpm)	1320	1475
Stator resistance r_s (Ω)	9.5	0.5148
Stator leakage inductance L_s (mH)	24.6	10.61
Rotor referred first component resistance $r_{r\alpha\beta}$ (Ω)	6.05	0.4116
Rotor referred third component resistance r_{rxy} (Ω)	1.2	0.216
Rotor referred first component inductance $L_{r\alpha\beta}$ (mH)	36.9	8.61
Rotor referred third component inductance L_{rxy} (mH)	7.4	4.523
Magnetizing first component inductance $L_{M\alpha\beta}$ (mH)	583.3	518.85
Magnetizing third component inductance L_{Mxy} (mH)	52.6	46.9
No. of poles	4	4
DC-link (V)	400	6800

5.4.1. Effect of δ on the produced torque

Figure 41 shows the effect of changing the trapezoidal modulating signal's slope angle δ on the produced torque, using the proposed TPD-PWM. Increasing the load torque, inherently, increases the phase currents; yet, changing δ leads to different phase currents at the same torque value (hence a room for torque enhancement can be achieved), as shown in Figure 41(a) and (b). They show that the same output torque value can be obtained at lower phase current value in case of δ = 10°, 20°, 25.7°, 30°, and 40° compared to SPD-PWM and THI techniques. On the contrary, at low torque values, the SPD-PWM and THI techniques offer lower currents for same output torque values. For

output torque near the rated, as shown in Figure 41(a) and (b), the lowest phase current to generate the same output torque flows with TPD-PWM with δ = 10°, of peak value 1.9 A and 60 A for IM I and IM II respectively at full-load torque. However, the quality of the delivered torque and current at that angle is questionable, as illustrated in Figure 41(c), (d), (e), and (f). The highest THD is produced at δ = 10°. The lowest THD can be obtained with a TPD-PWM of δ = 40°, as same as the THI modulation, as shown in Figure 41(c) and (d). The lowest torque ripples are obtained with SPD-PWM, whilst the highest torque ripples are produced with a TPD-PWM of δ = 30°. There is no noticeable difference in the torque ripples between TPD-PWM of δ = 10° and 25.7° near full-load.

The possible torque enhancement of each modulation technique of each machine is stated in Table 8, as well as, the corresponding THD of phase and $\alpha\beta$ currents. The slope angle δ = 25.7° provides optimum torque quality, as it provides the torque's highest enhancement at a THD near the SPD-PWM. The torque enhancement difference between TPD-PWM of δ = 10° and TPD-PWM of δ = 25.7° is small; yet, the latter provides a better line and $\alpha\beta$ currents' THD. It is worth mentioning that although the THD in phase currents may seem high, the THD in the torque producing current components ($\alpha\beta$ currents) is much lower.

Table 9. Torque enhancement comparison of *IM1* and *IM2*

	Torque enhancement%		αβ/phase Current THD%	
	IM1	IM2	IM1	IM2
SPD-PWM	0	0	3.96/7.9	6.32/12.66
TPD-PWM δ = 10°	15	24	7.74/88.67	13.04/69.28
TPD-PWM δ = 25.7°	13.33	22.5	4.83/65.4	8.12/49.7
TPD-PWM δ = 40°	8.5	14	3.25/40.63	5.35/34.03
THI	8.33	13.75	3.15/42.61	5.19/34.43

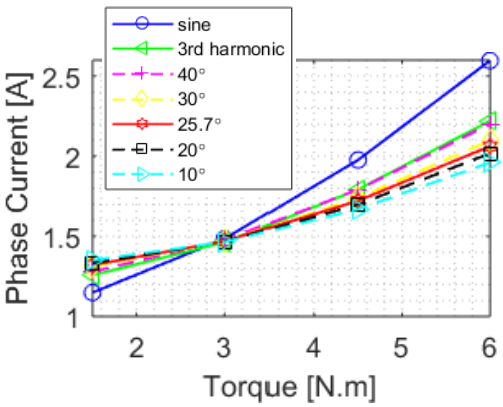

(a)

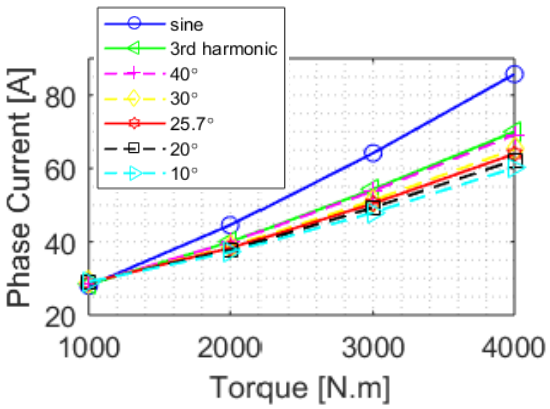

(b)

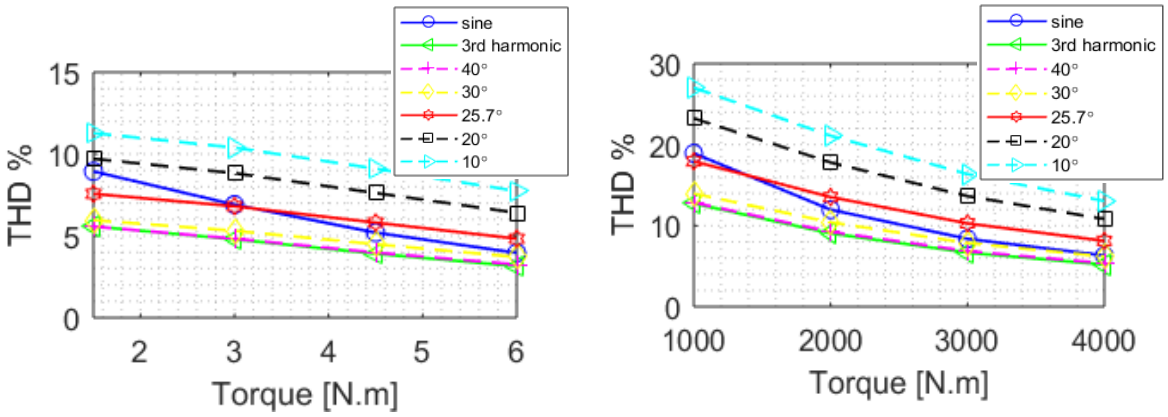

(c)

(d)

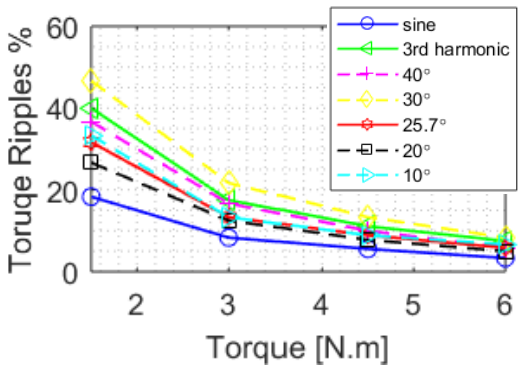

(e)

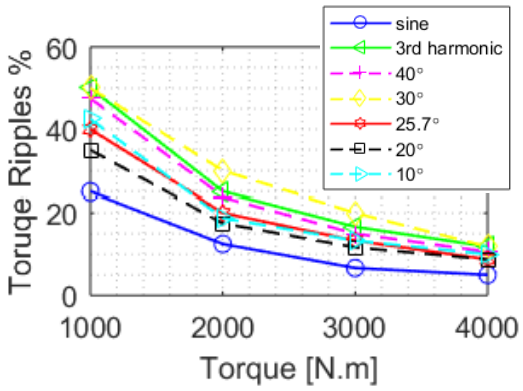

(f)

Figure 41. Simulation results. A comparison of TPD-PWM-based 3-level MMC employing two different five-phase IM models (IM I to the left, IM II to the right) at different load torques and slope angles δ. (a) and (b) T-I curves. (c) and (d) THD of $\alpha\beta$ currents. (e) and (f) Torque ripples.

5.4.2. δ Change at Full-Load Torque

Figure 42 evaluates the measured quantities at the full-load torque using different slope angles for both machines. The α-component of phase 'a' stator current is shown in Figure 42(a) and (b).

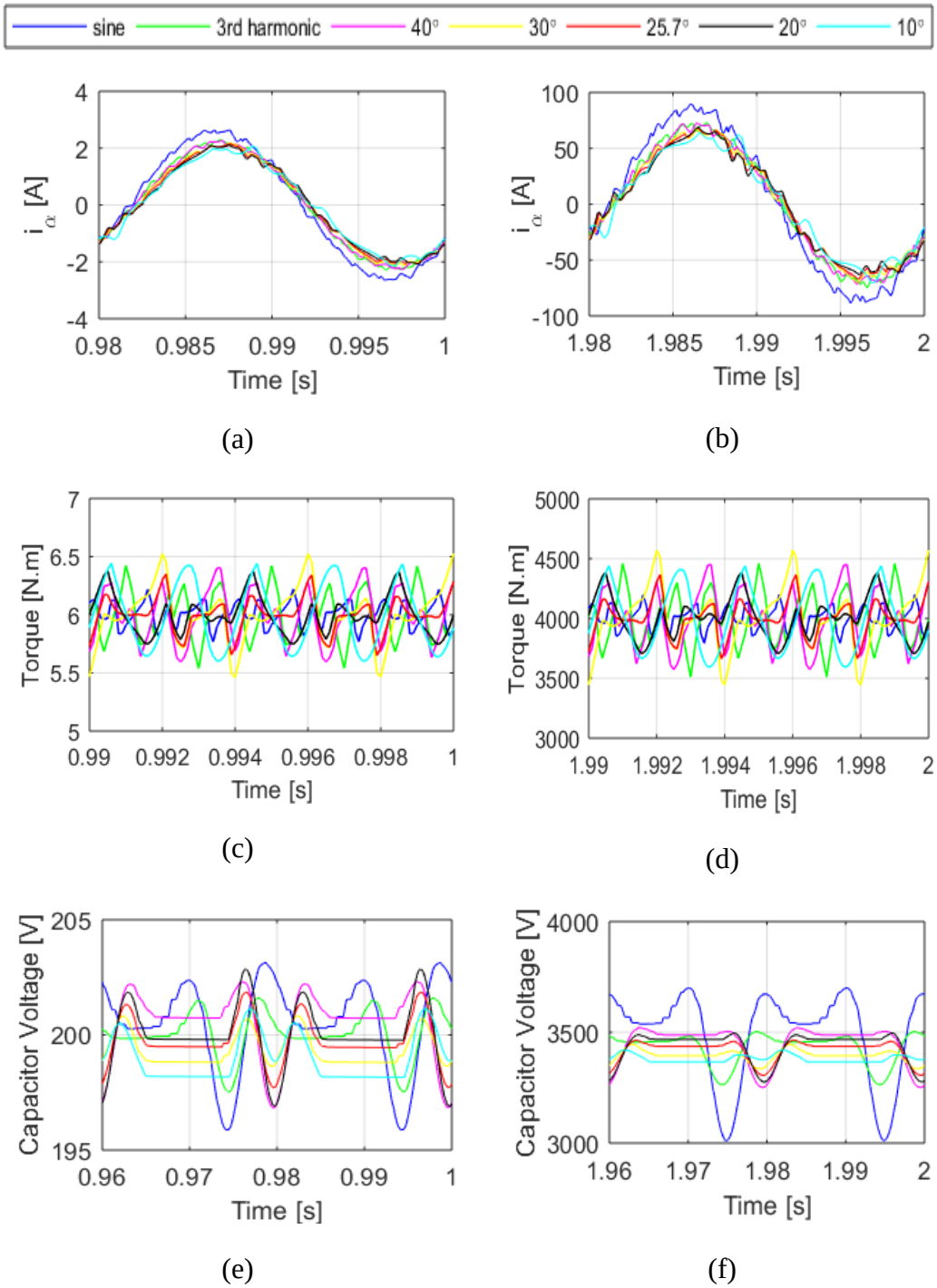

Figure 42. Simulation results. A comparison of TPD-PWM-based 3-level MMC employing two different five-phase IM models (IM I to the left, and IM II to the right) at full-load torque and different slope angles δ. (a) and (b) α-component current. (c) and (d) Torque. (e) and (f) upper arm capacitor voltage.

The highest current at the same torque (full-load) flows with SPD-PWM technique, whilst the lowest current flows with TPD-PWM of δ = 10°, δ = 20°, and δ = 25.7° respectively. The lowest torque ripples are given by applying SPD-PWM technique; meanwhile, the highest ripples are given when TPD-PWM of δ = 30° is applied, as shown in Figure 42(c) and (d). The balancing technique applied for the entire modulation techniques has ensured balanced capacitors voltages of the MMC's SMs as shown in Figure 42(e) and (f). The lowest capacitors voltage ripples of 2% are generated when TPD-PWM of δ = 25.7° and THI techniques are adopted, whilst the highest ripples of 3.6% are generated with SPD-PWM.

5.5. Experimental Results

The proposed TPD-PWM has been applied to a downscaled laboratory prototype of a three-level five-phase MMC-based IM drive system for experimental validation. The experiment parameters are given in Table 9. The applied machine parameters are given in Table 7 as *IM1*.

Table 10. Specifications of Experimental Setup

MMC Specifications	
MMC rating (kVA)	7
SM's capacitor voltage rating (V)	350
SM's capacitor (μF)	470
Arm inductor (mH)	1
IGBT IKW75N60T rating	30A/1200V
DC-link voltage (V)	350
Switching frequency (Hz)	600

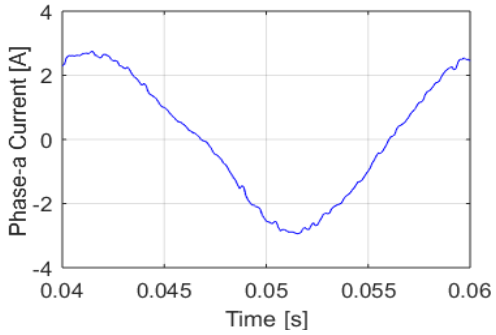
Phase-a Current [A]
Time [s]

(a)

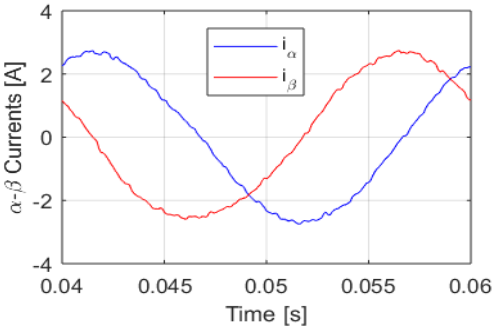
α-β Currents [A]
Time [s]
i α
i β

(b)

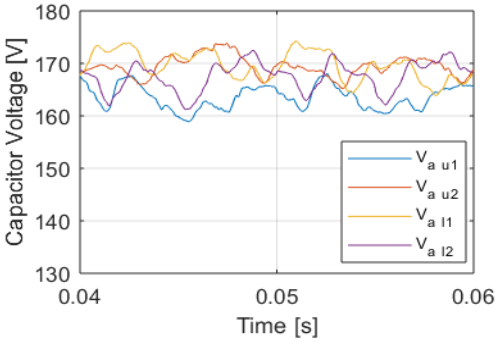
Capacitor Voltage [V]
Time [s]
V a u1
V a u2
V a l1
V a l2

(c)

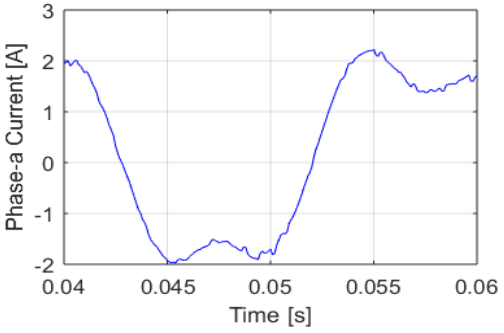
Phase-a Current [A]
Time [s]

(d)

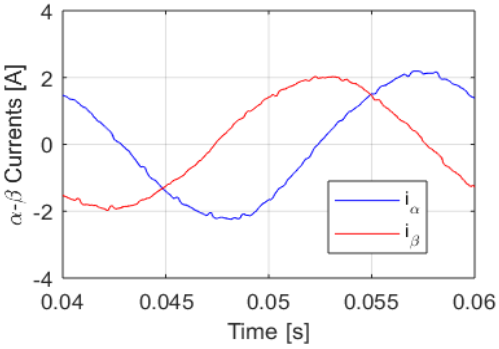
α-β Currents [A]
Time [s]
i α
i β

(e)

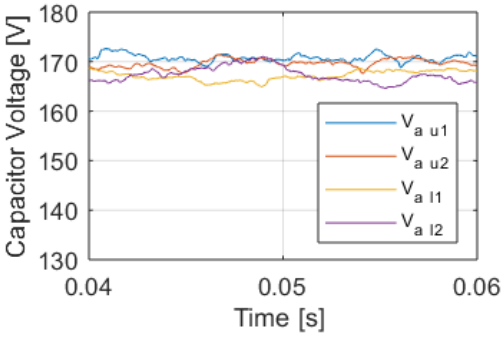
Capacitor Voltage [V]
Time [s]
V a u1
V a u2
V a l1
V a l2

(f)

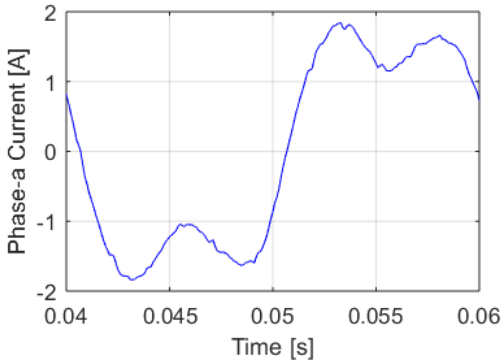
Phase-a Current [A]
Time [s]

(g)

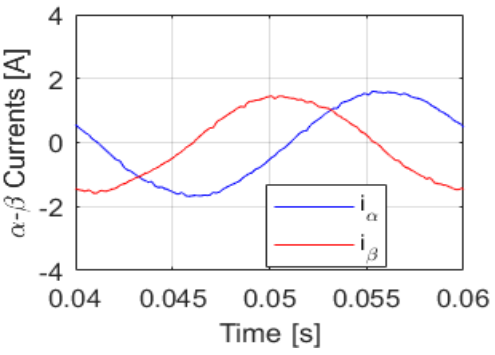
α-β Currents [A]
Time [s]
i α
i β

(h)

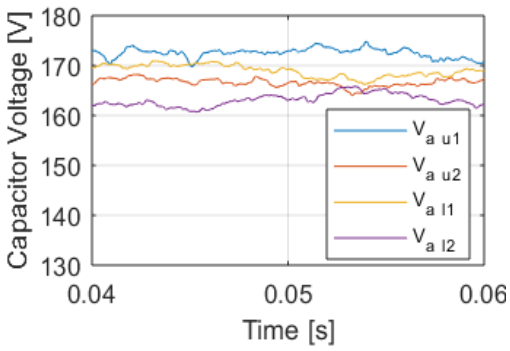
Capacitor Voltage [V]
180
170
160
150
140
130
0.04
0.05
0.06
Time [s]
V a u1
V a u2
V a l1
V a l2

(i)

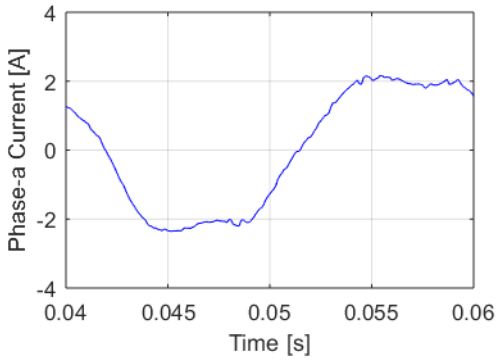
Phase-a Current [A]
4
2
0
-2
-4
0.04
0.045
0.05
0.055
0.06
Time [s]

(j)

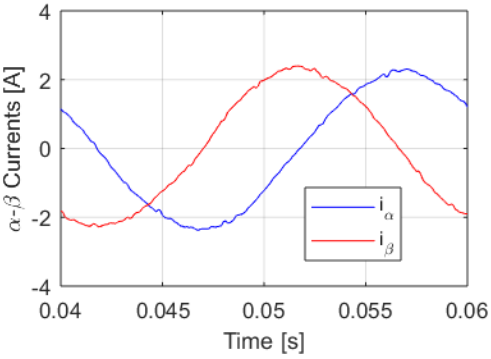
α-β Currents [A]
4
2
0
-2
-4
0.04
0.045
0.05
0.055
0.06
Time [s]
i α
i β

(k)

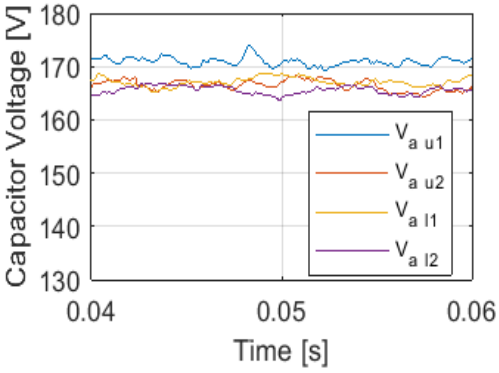
Capacitor Voltage [V]
180
170
160
150
140
130
0.04
0.05
0.06
Time [s]
V a u1
V a u2
V a l1
V a l2

(l)

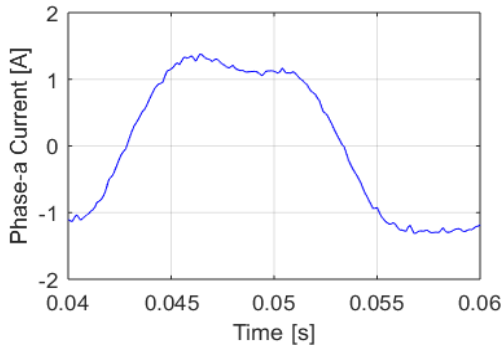
Phase-a Current [A]
2
1
0
-1
-2
0.04
0.045
0.05
0.055
0.06
Time [s]

(m)

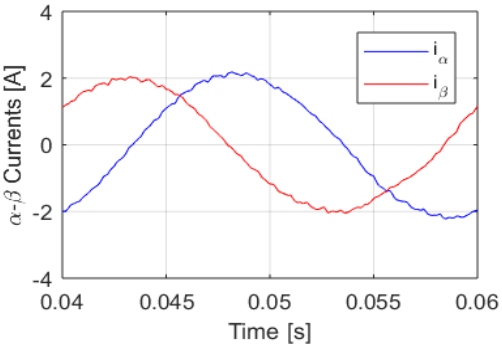
α-β Currents [A]
4
2
0
-2
-4
0.04
0.045
0.05
0.055
0.06
Time [s]
i α
i β

(n)

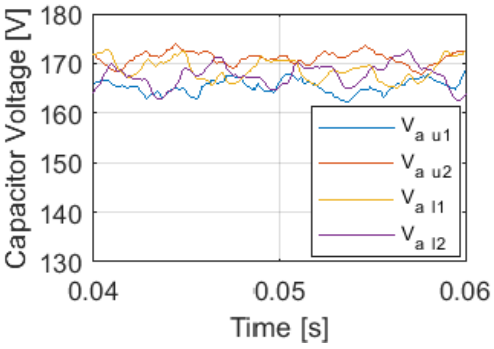
Capacitor Voltage [V]
180
170
160
150
140
130
0.04
0.05
0.06
Time [s]
V a u1
V a u2
V a l1
V a l2

(o)

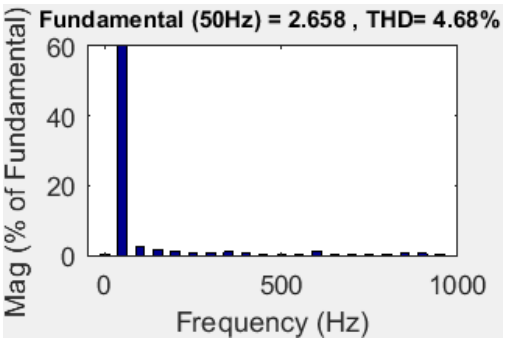
Fundamental (50Hz) = 2.658 , THD= 4.68%
Mag (% of Fundamental)
60
40
20
0
0
500
1000
Frequency (Hz)

(p)

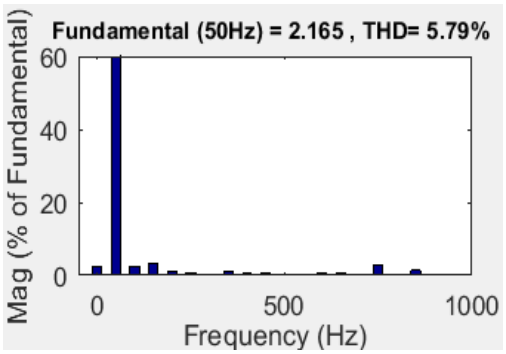

(q)

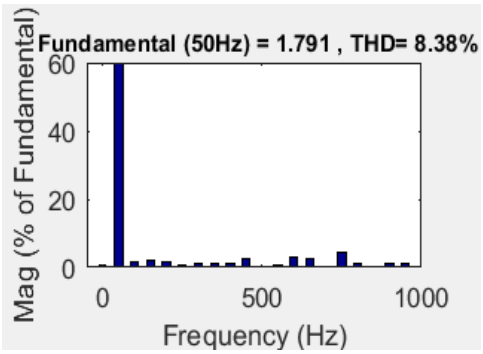

(r)

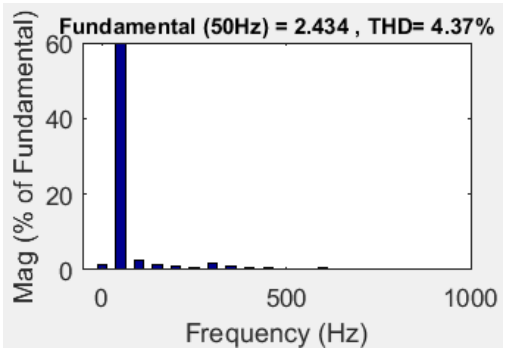

(s)

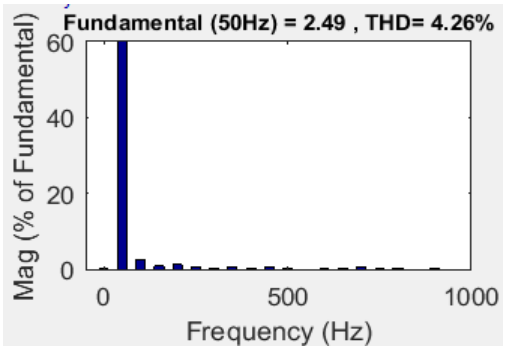

(t)

Figure 43. Experimental results of phase ‘a’ current (to the left), $\alpha\beta$ currents (in the middle), phase ‘a’ SMs’ capacitors voltage (to the right) and FFT of phase ‘a’ $\alpha\beta$ currents respectively at different modulation methods. (a), (b), (c) and (p) SPD-PWM. (d), (e), (f), and (q) TPD-PWM δ = 25.7°. (g), (h), (i), and (r) TPD-PWM δ = 10°. (j), (k), (l), and (s) TPD-PWM δ = 40°. (m), (n), (o) and (t) THI.

The different modulation methods have been applied in order to control the IM drive. The measured quantities are shown in Figure 43. The output phase current, when SPD-PWM, THI, and TPD-PWM of δ = 10°, 25.7°, and 40° are applied, are shown in Figure 43(a), (e), (i), (m), and (q). The $\alpha\beta$ currents are shown in Figure 43(b), (f), (j), (n), and (r). The capacitors voltages of phase ‘a’ SMs are shown in Figure 43(c), (g), (k), (o), and (s). The Fast Fourier Transform (FFT) of phase ‘a’ $\alpha\beta$ currents are shown in Figure

43(d), (h), (l), (p), and (t). The TPD-PWM of δ = 25.7° provides a better torque enhancement at approximately a similar THD compared to SPD-PWM (they provide the lowest $\alpha\beta$ currents for the same torque). It is also shown that the TPD-PWM of δ = 25.7° provides the lowest SM's capacitor voltage ripples.

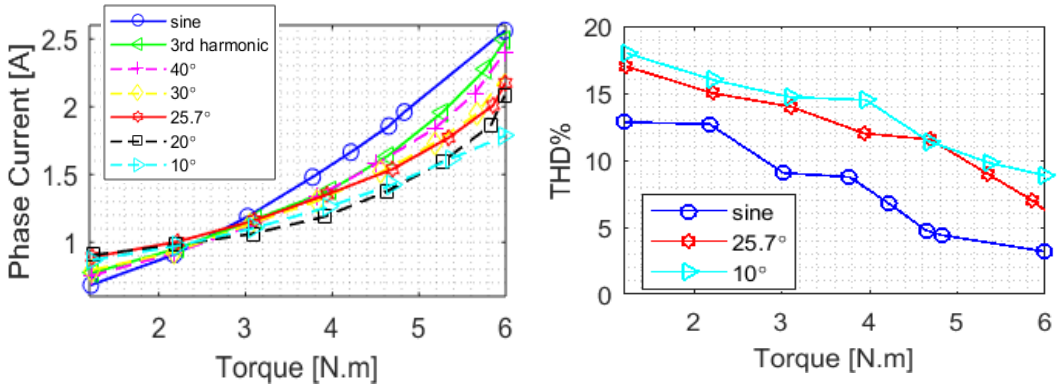

(a) (b)

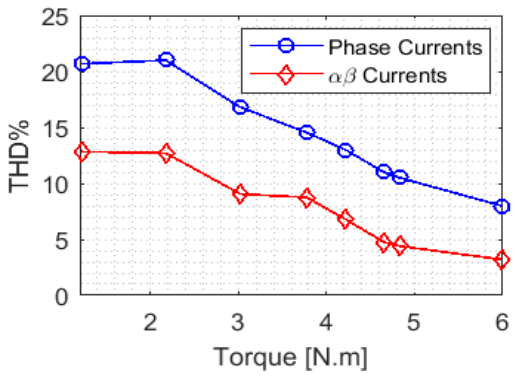

(c)

Figure 44. Experimental results. (a) IM T-I curve using different modulation methods. (b) THD of $\alpha\beta$ currents for SPD-PWM, and TPD-PWM of δ = 10° and δ = 25.7°. (c) THD of phase 'a' current compared to the $\alpha\beta$ currents.

Figure 44(a) shows the torque/current characteristics of each modulation method. Complying with the simulation results, the lowest phase current to provide rated torque flows with TPD-PWM of δ = 10°, whilst the highest current flows using SPWM. A 13% torque enhancement can be obtained by using the TPD-PWM with δ = 25.7° compared to SPD-PWM. Figure 44(b) depicts the difference between the output current THD in case of SPD-PWM, and TPD-PWM of δ = 10° and δ = 25.7°. It is clear that TPD-PWM of δ = 10° has the worst THD, even though it provides the best torque enhancement of 16%. Figure 44(c) illustrates that torque producing component ($\alpha\beta$ currents) have a better THD compared to the stator phase current, which is a feature of the multiphase machine, where the losses are mapped in the *x-y* plane.

Figure 45 shows the output waveforms when the TPD-PWM of δ = 25.7° has been applied. Figure 45(a) shows the output phase voltage and current. Figure 45 (b) shows the loading of the IM from a lighter load to a full load. Figure 45 (c) shows the motor speed.

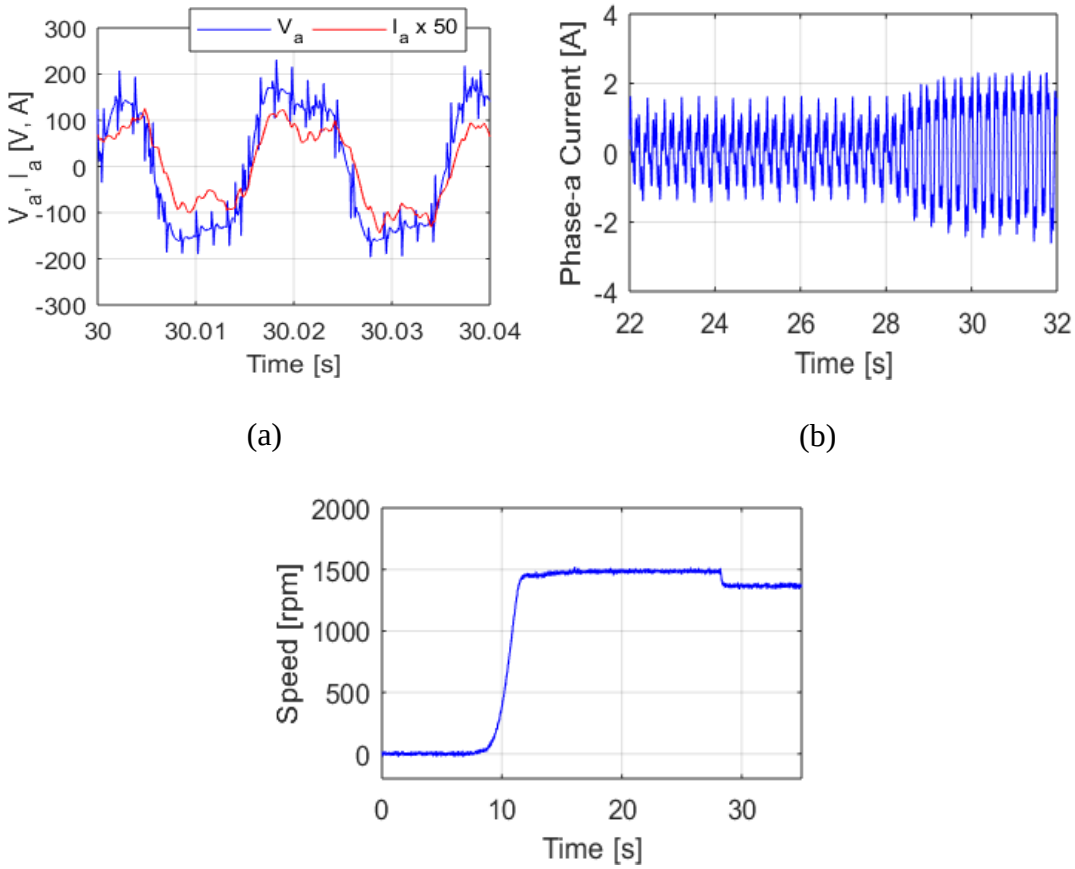

Figure 45. Experimental results of TPD-PWM of $\delta = 25.7°$. (a) phase 'a' current and voltage. (b) phase 'a' current during loading. (c) motor speed.

5.6. Challenges

After explaining the new control techniques and converter topologies that ease the utilization of MMCs in medium-voltage ASDs, the generation of adequate DC-link voltage levels to supply the drive system is challenging. Conventional rectifiers suffer transformer operation, a high number of semiconductor devices, or complicated control schemes. In the next chapter, an AC-DC converter with boosting capability using simple series-connected HB-modules and control scheme is proposed.

CHAPTER 6: SERIES-CONNECTED MULTI-HALF-BRIDGE MODULES IN MEDIUM-VOLTAGE VARIABLE SPEED DRIVES OPERATION

This chapter studies the utilization of the series-connected HB modules in medium-voltage ASD operation. The study comprises the utilization of these modules in providing adequate DC-link voltage for the medium-voltage levels. In addition, a technique for the ASD regenerative braking is also adopted.

The work presented in this chapter is inspired from the HVDC shunt tap topology proposed in [108]. That HVDC tap architecture is shown in Figure 46, which consists of six series-connected DC capacitors connected across the DC bus. Ideally, the voltage of each capacitor equals to the total DC voltage divided by the number of series-connected capacitors (i.e., $V_c = V_{dc}/6$).

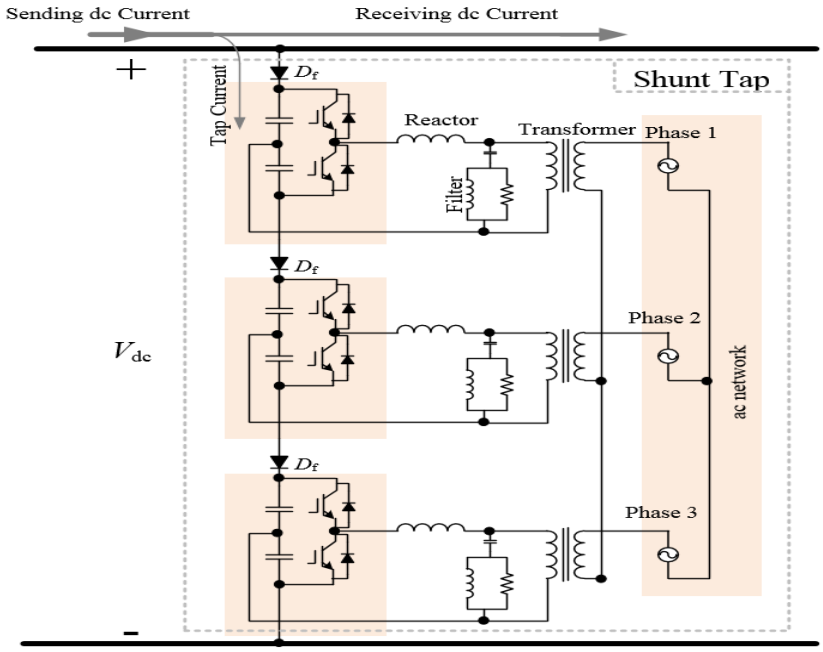

Figure 46. HVDC shunt tap proposed in [88].

Each two successive DC capacitors are used to feed a two-level HB converter. Each half-bridge converter feeds one-phase of the three-phase load. The voltage profile of each phase is a bipolar voltage ($\pm V_{dc}/6$), with a fundamental component of $MV_{dc}/6$, where M is the modulating signal peak where $0 < M < 1$. This arrangement has a bucking capability from the DC side to the AC side (inversion mode). Extra protecting diodes (D_f) have been used in this topology to block the current flow from the AC network (tap) into the DC-link during DC line faults. However, in order to permit a bidirectional power flow, these blocking diodes should be eliminated.

6.1. Series-Connected HB Modules as AFE Rectifier

One of the main components of any medium-voltage motor drive is the DC supply [109], [110]. Rectifiers are used to convert the grid power into DC quantities. They are classified into passive, hybrid, and active rectifiers [109], [111], [112]. The passive rectifier usually consists of diodes, while the hybrid rectifier consists of a combination of diodes and controlled switching devices. The active rectifier is only based on controlled switching devices. Passive rectifiers are commonly used as a front-end for medium-voltage motor drives when applied to fans, compressors, blowers, and pumps applications, as they require neither fast-dynamic speed control nor regenerative braking features. They are usually inexpensive and reliable. Therefore, three-phase six-, twelve-, eighteen-, and twenty four-pulse diode rectifiers are ordinarily used [110]. However, such rectifiers do not meet international standards as they introduce high harmonic content in the AC supply side. A multi-winding phase shifting transformer is requisite for the operation of these rectifiers that introduces reliability, cost, and footprint concerns. This transformer's reliability is related to potential voltage and winding imbalances which are one of the harmonic sources. In addition, the produced DC voltage of these rectifiers contains high voltage ripples that require filtering stage.

In hybrid rectifiers, both sinusoidal currents withdrawal and voltage regulation cannot completely be achieved. Therefore, active rectifiers [112] were introduced in order to withdraw sinusoidal currents from the AC mains with improved output DC voltage ripples, as well as enabling regenerative braking features. They are able to work at high power factor and low THD. Even though they are more expensive and less reliable. The most common AFE rectifier is the six-switch two-level active rectifier [113]. Nevertheless, the voltage levels of the electric machines used in certain high power industries have been immensely increased. Step-up transformers can be used in order to elevate the AC output of the drive system. Yet, most industries tend to apply transformer-less installation as they are bulky, high cost, and increase footprint. Therefore, advanced active rectifiers have been introduced in order to generate medium DC-link voltage in order to meet the voltage and power requirements of high power applications. An NPC and flying-capacitor three-level-based rectifiers have been introduced in [32], [114], [115]. These rectifiers can either double the DC voltage generated from certain AC supply or reduce the voltage rating of switching devices to half at the same DC-link level. However, they exhibit voltage drifting and balancing issues, in addition to the high number of diodes/capacitors. Moreover, due to the complexity of increasing their number of levels, the transformer stage may be required as well. CHB rectifiers are introduced in [116], [117] as an active rectifier for medium-voltage applications. However, this topology exhibits instability in output DC buses voltages, hence switching devices are vulnerable to collapse. Hexagram multilevel rectifier was proposed in [118]. It employs lower ratings switching devices; however, it requires a high number of switching devices and multi-secondary isolation input transformer. MMC was introduced as an AFE rectifier in [119]. It combines several merits such as modularity, scalability, and redundancy.

In this chapter, the generation of medium DC-link voltage for supplying medium-voltage ASDs is sought using series-connected multi HB modules. The presented approach has been inspired from the converter used in [120]. The main advantages of the proposed configuration are reducing the switching devices rating to $V_{dc}/3$. In the proposed configuration, six DC capacitors with a voltage rating of $V_{dc}/6$ and only six IGBTs are employed, as well as a simple control strategy. The main drawback of applying MMC as AFE rectifier compared to the proposed strategy is the higher number of the required IGBTs.

6.1.1. System Architecture

The proposed configuration for generating medium DC-link voltage from the low-voltage grid using series-connected HB modules is shown in Figure 47. The proposed system consists of three series-connected HB modules, an isolation transformer, and *L*-filter. The HBs' DC sides are connected in series, while each of their AC sides is connected to one phase of the grid supply through proper *L*-filter and single-phase transformer as shown in Figure 47. Isolation transformers, as the input stage before the AFE rectifier, are required. The isolating transformers provide isolated AC main phases as inputs for the involved HB modules. The transformers with proper turns-ratio are also used to adjust the voltage level according to the desired DC-link voltage level. On the other hand, *L*-filters are required to ensure operating with a non-distorted sinusoidal grid current with acceptable THD. *L*-, *LC*-, and *LCL*-filters can be used. For simplicity, *L*-filter is applied in this work. The HBs' DC-link capacitors should be chosen properly to avoid unnecessary voltage ripples during the operation. The detailed design of the suitable values of HBs' capacitors and the *L*-filter inductors can be found in [121].

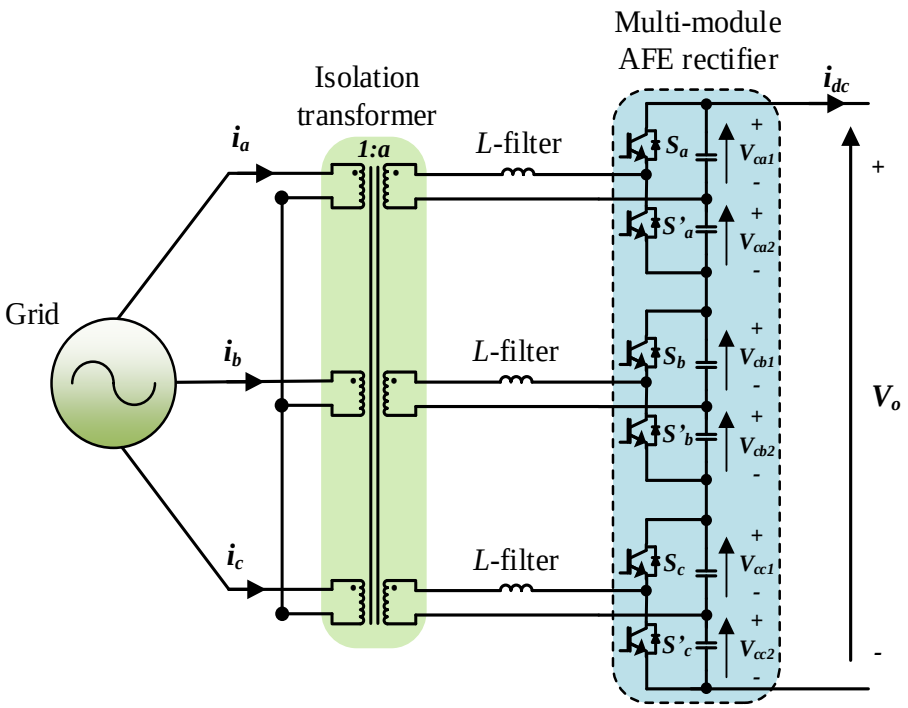

Figure 47. Schematic of the proposed configuration.

Clearly, the proposed configuration has a boosting capability from the AC to the DC side. Consequently, a lower AC voltage can be adopted to generate a specific DC-link voltage; in other words, higher DC-link can be generated from the same AC main. A six-times output DC-link voltage can be generated compared to the input AC-peak referred to the converter side. If the peak of the input AC voltage referred to the converter side is around $V_{dc}/6$, then an output DC-link voltage of V_{dc} can be obtained. The corresponding voltage rating of each IGBT of the involved HBs is $V_{dc}/3$.

The main advantages of the proposed configuration are:

- The series connection of HB modules provides operating with a high boosting ratio, which allows generating a medium DC-link voltage from low-voltage grids while employing a transformer with reasonable turns-ratio.
- Employing relatively low-voltage rating semiconductor switches. Hence, the

complexity and challenges of series-connection of semiconductor devices are avoided.

6.1.2. Control Strategy

The proposed control strategy, shown in Figure 48, is based on conventional grid power control, where PI controllers are used to control DC-link voltage as well as the grid currents. First, *α-β* and *d-q* transformations are applied. Grid's voltage and current are measured. The grid voltage is fed to a Phase-Locked Loop (PLL) to obtain the grid's phase angle, which is used for *d-q* transformation. Then the *d-q* current components can be generated. The output DC-link voltage is measured then compared to the reference voltage; the error is applied to a PI controller. The PI controller output represents the reference active power current component i_{dg}^*. The reference reactive power current component i_{qg}^* is set to zero. Both reference values are compared to the measured ones. The errors are applied to PI controllers to get the required *d-q* voltage components as shown in Figure 48.

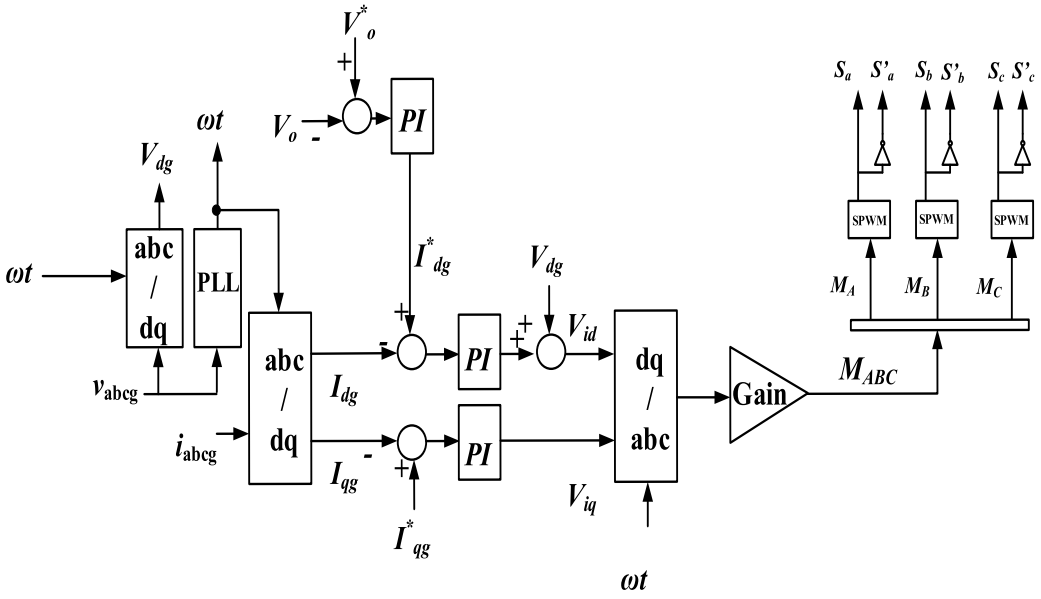

Figure 48. Control Strategy.

Then inverse transformation is applied to the *d-q* voltage components to generate the three-phase time-domain reference voltages for the involved HBs. Then inverse transformation is applied to the *d-q* voltage components to generate the three-phase time-domain reference voltages for the involved HBs. Then per-unit reference voltage for each involved HB modules (M_{ABC}) can be extracted by using proper gain as shown in Figure 48. Then the conventional sinusoidal PWM is employed to generate the gate pulses of the involved HB modules (S_a, S_a', S_b, S_b', S_c, and S_c').

6.1.3. Proposed system vs. Two-Level controlled rectifiers

The conventional two-level fully controlled rectifiers consist of six switching devices as same as the proposed AFE rectifier configuration. However, the rating of the switching devices in the proposed topology is $V_{dc}/3$, whilst the rating of the conventional rectifier switching devices is V_{dc}. Moreover, in order to obtain a V_{dc} output DC-link voltage, an AC input referred to converter side of peak $V_{dc}/2$ is required in the case of the conventional rectifier, whilst a peak of $V_{dc}/6$ is required in the case of the proposed rectifier configuration. Therefore, the proposed configuration offers a significant advantage compared to the conventional configuration. The proposed topology is able to generate the required DC-link voltage using switching devices of 1/3 voltage rating compared to the conventional three-phase two-level VSC with parallel legs.

6.1.4. Simulation

In this section, the performance of the proposed configuration is simulated using MATLAB/Simulink platform assuming different loading conditions. The simulation model parameters are given in Table 11. The simulation case study is designed in order to provide a DC-link voltage of 8kV to a certain drive system using the proposed rectifier configuration. The simulation study aims to expose the boosting capabilities of

the proposed architecture while maintaining low voltage rating switching devices.

Table 11. Simulation Parameters

DC-link voltage (*kV*)	8
Grid voltage (V_{rms})	220
HB's capacitor (*mF*)	10
L-filter reactor (*mH*)	5
Transformer turns ratio	310:1500
Switching frequency (*kHz*)	2

The simulation results are shown in Figure 49 assuming that the equivalent resistance seen by the DC-link voltage equals 100Ω for $t<2.5\ s$ *and* $t>3.5s$, while it equals 80Ω for $2.5s<t<3.5s$. Figure 49(a) shows the output DC-link voltage. The voltage is well regulated and tracking its reference value of 8 kV. The DC-link current is shown in Figure 49(b). A sinusoidal grid current with low harmonics content has been withdrawn as shown in Figure 49(c) and (d). The direct and quadrature current components of zero reactive power operation are shown in Figure 49(e). The direct current tracks its reference value that is extracted from the regulation of DC-link voltage. The controller sets the quadrature current component to zero.

The HB modules' capacitor voltages are shown in Figure 49(f) and (g). The capacitor voltages are balanced and equal to $V_{dc}/6$. The voltage peak-to-peak ripples are low with approximately 7.5% of the HB voltage level. An FFT was performed on the grid current in order to obtain its THD. The grid current THD is 3 %, which is acceptable in the

grid-connected applications as shown in Figure 49(h).

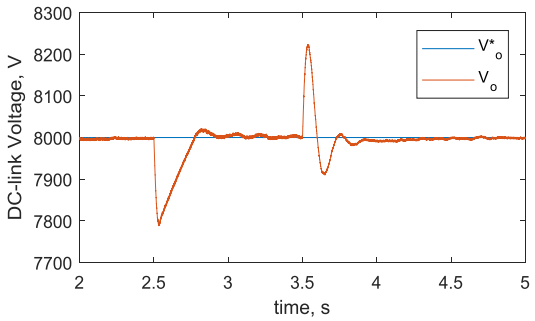

(a)

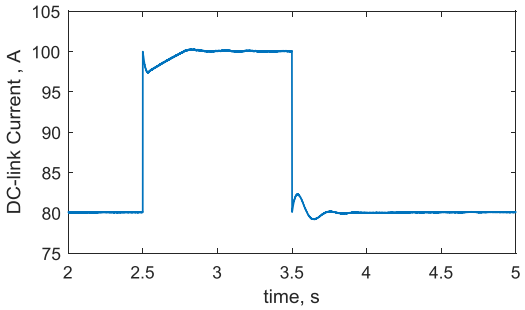

(b)

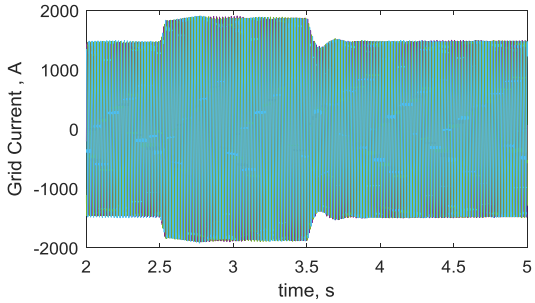

(c)

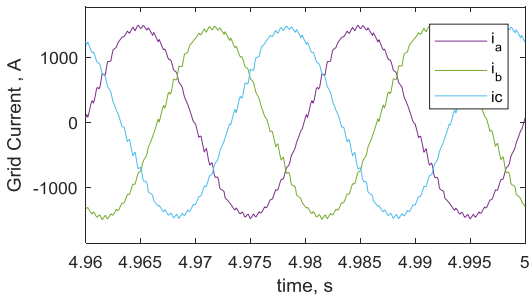

(d)

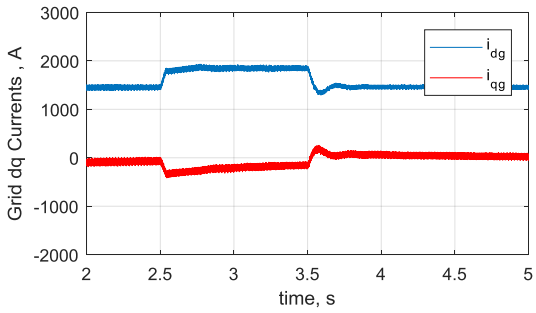

(e)

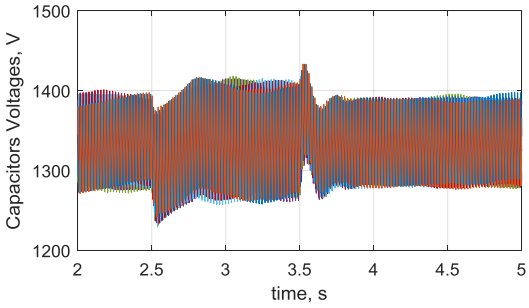

(f)

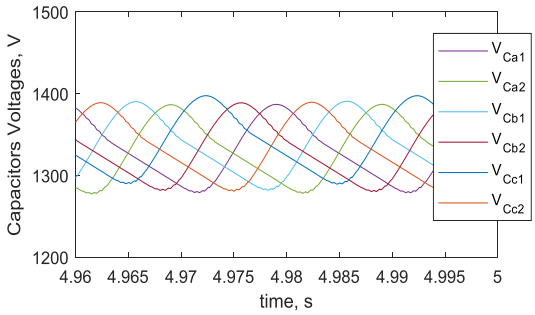

(g)

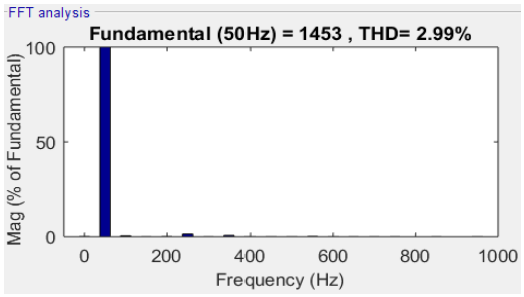

(h)

Figure 49. Simulation results: (a) output DC-link voltage, (b) output DC-link current, (c) grid current, (d) zoomed-in view of the grid current, (e) direct and quadrature components of grid current, (f) HBs' capacitors voltage, (g) zoomed-in view of HBs' capacitors voltages, and (h) FFT spectrum of the grid current.

6.2. Application for the Series-Connected HB Modules: ASD's Regenerative Braking Operation

In this section, a transformerless regenerative braking topology is proposed for integrating low-voltage high-power drives with medium-voltage DC-links, where the obtained AC–DC voltage boosting is enough to produce the required DC-link voltage.

6.2.1. System Architecture

A. Converter Topology

The proposed configuration for integrating a multiphase machine with DC-link is shown in Figure 50, proposing an asymmetrical six-phase machine. The proposed converter consists of six HB converters; their DC sides are connected in series, while the AC side of each HB converter is connected to one phase of an open winding asymmetrical six-phase machine. Each HB converter controls the phase current of the corresponding generator phase. The voltages of the DC capacitors (12 capacitors in case of a six-phase machine) are also controlled to ensure an equal voltage sharing. The voltage share of each capacitor equals (V_{dc}/12), which results in a phase voltage magnitude of MV_{dc}/12.

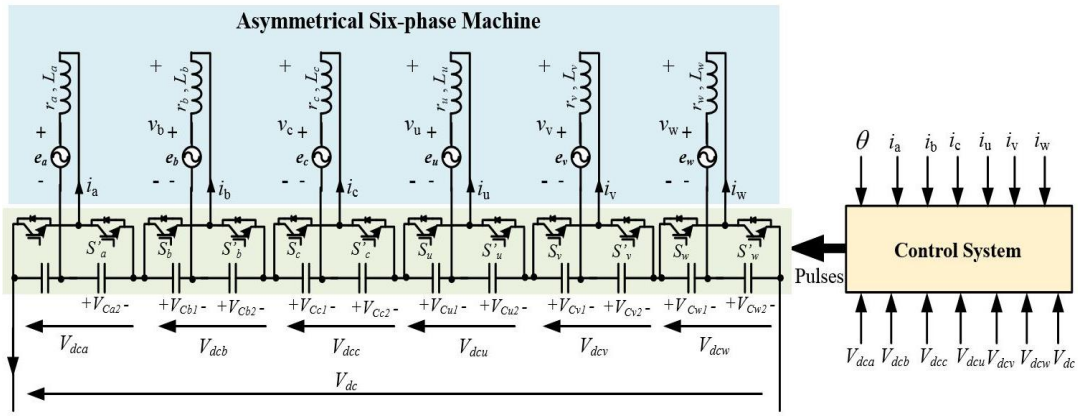

Figure 50. The proposed series-connected HBs configuration.

It is clear that the proposed configuration has a good boosting capability from the AC to the DC side; hence, relatively low-voltage machines can directly be coupled to a relatively high voltage DC-link (V_{dc}) without an extra voltage boosting stage. The main

advantages and challenges of the proposed architecture are mentioned clearly in the following subsection.

B. Advantages and Challenges of the Proposed Converter

The proposed converter provides the following advantages:

- Operation with a relatively high AC-DC boosting capability (1:2*m*), where *m* is the number of generator phases when compared with available topologies in literature.
- Relatively low-voltage rating switching devices can be employed for a given high DC-link voltage level.
- Modular controllers can be employed, as each phase can be independently controlled.

On the other hand, some challenges are imposed when such an architecture is employed, which are:

- The insulation level of different generator phases will be different due to the series connection of the DC-link capacitors. The lower winding (the nearest winding to the negative pole of the DC-link voltage) will have a lower insulation level, namely V_{dc}/m, while the upper winding (the nearest winding to the positive pole of the DC-link voltage) will have the highest insulation level which is V_{dc}. The insulation level of different winding sets increases gradually with a step of V_{dc}/m from the lower to the upper windings. This will impose technical challenges if a conventional double-layer distributed winding is adopted, which is the practical case for conventional high power generators. Recently, the non-overlapped Fractional Slot Concentrated Winding (FSCW) layouts [122] allow for a modular machine from the construction point of view, which facilities the machine manufacturing and provides a more cost-effective

design [123]. Fortunately, the modular construction with single layer winding adopted facilitates the winding insulation process and can be a practical example where the proposed converter can be applied. For certain slot/pole combinations, a complete physical separation between phases can be obtained, which highly simplify the electrical insulation of different phases [124].

- Each phase of the machine is connected between the mid-point of the HB converter leg and the mid-point of the common point between each pair of capacitors. Hence, the phase current will circulate through these capacitors, which corresponds to a notable voltage ripple component superimposed on the capacitors' voltages. This voltage ripple component depends on the operating frequency, phase current magnitude, and the capacitance value. The average DC voltage level across each capacitor equals $V_{dc}/(2m)$ while the frequency of this superimposed voltage ripple component equals the fundamental frequency. Increasing the capacitance can be a simple and direct solution to reduce this ripple voltage; however, this may end up with high capacitance values for low-voltage high-power systems. By thoroughly investigating this problem, it has been found that there is a relation between the capacitance value and the fundamental phase voltage magnitude. As the capacitance value decreases, the fundamental phase voltage increases for the same peak as the modulating signal. This is mainly due to the induced voltage ripple component has the same fundamental frequency. On the other hand, a low value of the DC-link capacitors corresponds to a higher ripple current magnitude at the DC side. Hence, a compromise should be made in the converter design between the acceptable DC-link current ripple and the minimum capacitance that may be employed. The effect of the capacitance value on the output voltage magnitude

will be highlighted in the next sections.

6.2.2. The Control System

The per-phase controller for the proposed configuration is shown in Figure 51, where *j* denotes the phase letter (*j* = *a*, *b*, *c*, *u*, *v*, and *w* in case of the six-phase system). The control system is divided into two controllers, the current controller, and the DC voltage controller. The details of each controller stage are illustrated in the following subsections.

A. Current Controller

Since all phases are independently controlled and to ensure proper current tracking, two PI controllers are used to control the current of each phase. First, the current of any phase (i_j) is measured and transformed into equivalent *dq*-components, as shown in Figure 51 [125]. The synchronization angle of each phase (θ_j) is obtained as shown in Figure 52. Two PI controllers are used to determine the *dq* voltage components as shown in Figure 51. Then *dq* voltage components can be transformed into $\alpha\beta$ voltage components. The extracted α-component of the voltage represents the reference voltage of the HB converter for phase (*j*) [125].

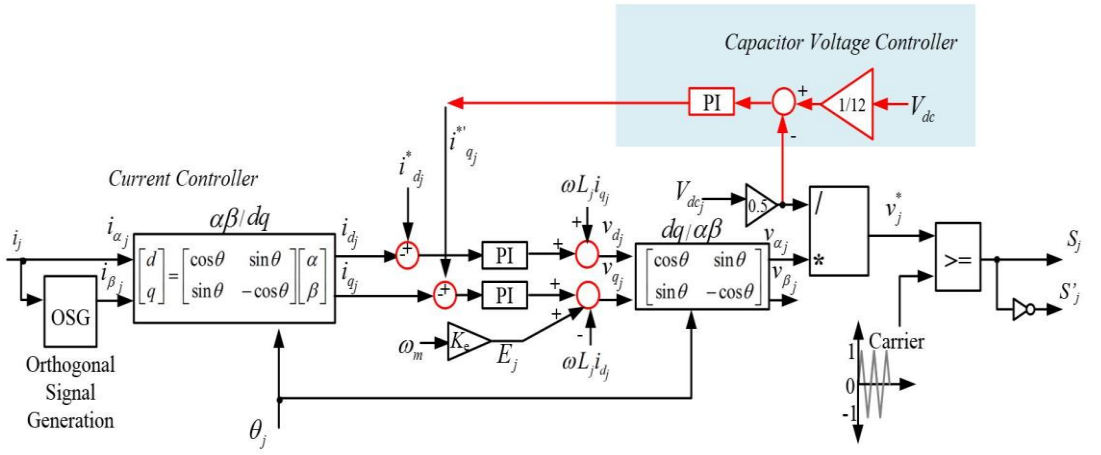

Figure 51. Per-phase controller of the proposed architecture.

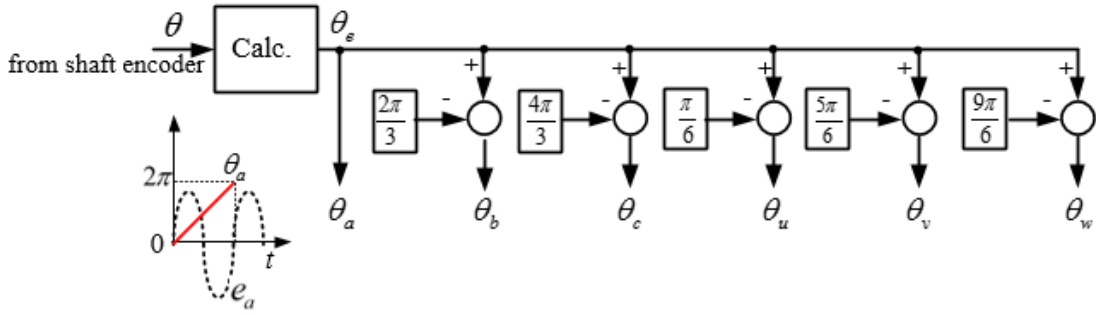

Figure 52. Extracting the orientation of machine phases.

Due to the series connection of the DC capacitors, the instantaneous values of the DC sides of different HB are not equal. Hence, each DC capacitor voltage should be measured to calculate the suitable modulating signal for each phase. Finally, conventional sinusoidal PWM modulation can be simply employed to control the voltage of each phase based on the extracted per-phase reference modulating voltage signal (v^*_j).

B. DC Capacitor Voltage Controller

The DC capacitor voltage controller is employed to ensure equal voltage distribution

among the series-connected DC side capacitors. In the capacitor voltage controller of the proposed architecture, the half of the per-phase DC-side voltage (V_{dcj}) is compared with the total DC voltage divided by the total number of DC capacitors (12 in case of the six-phase machine). A PI-controller is then used to generate the required quadrature component of the corresponding reference current to ensure equal voltage distribution in case of any possible mismatch, as shown in Figure 51.

6.2.3. Simulation

In this section, the system performance of a typical 2MW drive system is simulated using Matlab/Simulink. The DC side of the proposed architecture is connected to a DC-link of 4kV. The simulation parameters are shown in Table 12.

Table 12. Simulation Data

PMSM rated power (MW)	2
Frequency (Hz)	50
Per-phase inductance of the winding (μH)	200
Per-phase resistance of the winding (mΩ)	0.3
Per-phase rated voltage peak (V)	200
i_{qj}^* and i_{dj}^* (A)	-3000 (rated) and 0 respectively
DC-link capacitances	Case 1: 200 mF (High capacitance) Case 2: 50 mF (lower capacitance)
Carrier frequency (kHz)	5

First, the effect of capacitance value on the output voltage and the capacitor ripple voltage is investigated in the presented simulation study. Then, a simulation case study of the overall system under variable speed is introduced.

A. Effect of DC-link Capacitances on System Performance

To investigate the effect of capacitor design on the system performance, the system performance is compared under two different values of the module capacitors, namely, 200mF and 50mF. The capacitance is relatively high because the machine phase voltage is low (200V peak) while the phase current is relatively high (3kA peak). The corresponding simulation results for these two values are shown in Figure 53 and Figure 54 respectively, assuming a fundamental output frequency of 50 Hz and the induced EMF of phase '*a*' is taken as a reference.

The modulating signals for both cases are shown in Figure 53(a) and Figure 54(a) respectively. Figure 53(b) and Figure 54(b) show that the capacitor voltages are balanced in both cases, and the per-phase DC-voltages are balanced as well, and their summation equals to the total DC-link voltage of the proposed converter. The capacitor ripple voltage magnitudes mainly depend on the magnitude of phase currents and the selected capacitances. As a result, the voltage fluctuations in the case of low DC-link capacitances are higher, which results in a higher possible fundamental output voltage. To have the same output voltage in both cases, the peak value of the modulating signals in case of low DC-link capacitances will be lower, as depicted by Figure 53(a) and Figure 54(a).

The phase currents in both cases are shown in Figure 53(c) and Figure 54(c) respectively. It is clear that the currents are identical and their peak magnitude equals the absolute of quadrature current reference $|i_q^*|$ (i.e., 3000A), which confirms successful current tracking of the proposed controller.

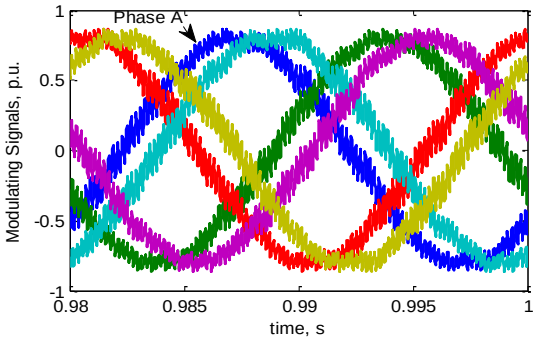
Phase A
Modulating Signals, p.u.
time, s

(a)

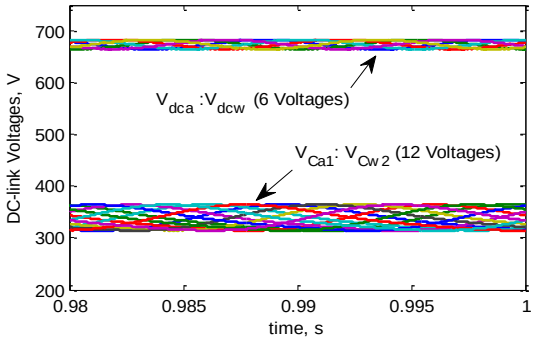
V_{dca} :V_{dcw} (6 Voltages)
V_{Ca1}: V_{Cw2} (12 Voltages)
DC-link Voltages, V
time, s

(b)

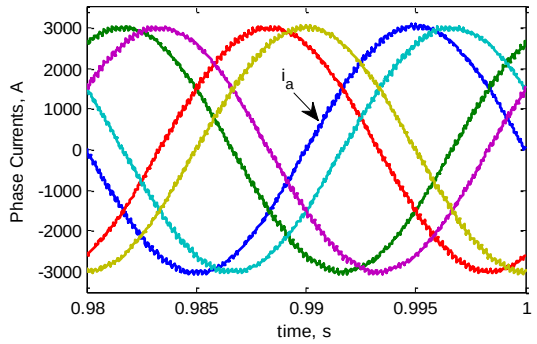
i_a
Phase Currents, A
time, s

(c)

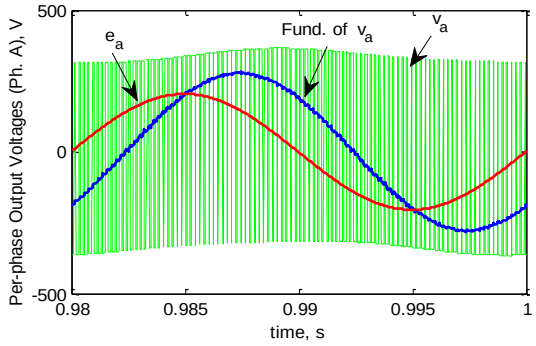
e_a
Fund. of v_a
v_a
Per-phase Output Voltages (Ph. A), V
time, s

(d)

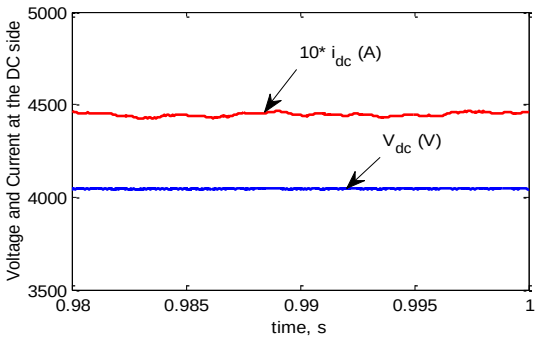
10* i_{dc} (A)
V_{dc} (V)
Voltage and Current at the DC side
time, s

(e)

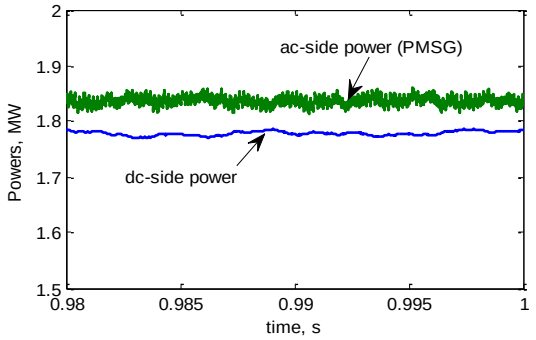
ac-side power (PMSG)
dc-side power
Powers, MW
time, s

(f)

Figure 53. Simulation results for a high DC-link capacitance (200mF) at rated frequency: (a) Modulating signals of the involved HB converters, (b) DC-link voltages, (c) Phase currents, (d) Per-phase output voltages (phase a), (e) DC voltage and scaled-up current at the DC terminals of the proposed architecture, (f) Input (AC side) and output (DC side) powers.

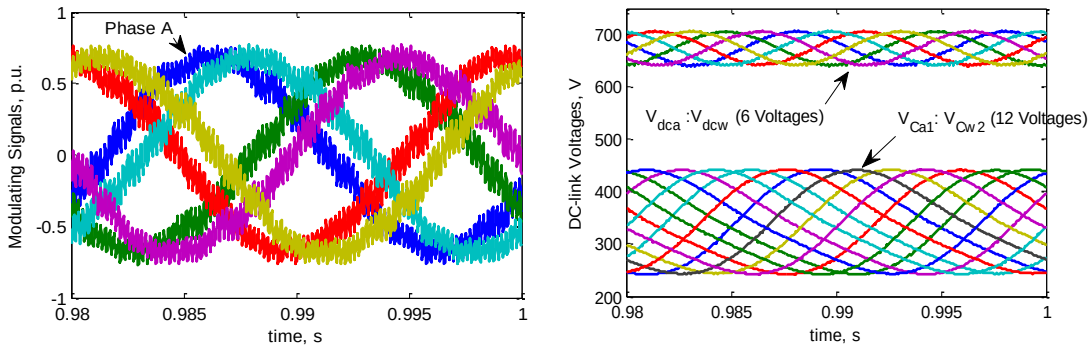

(a)

(b)

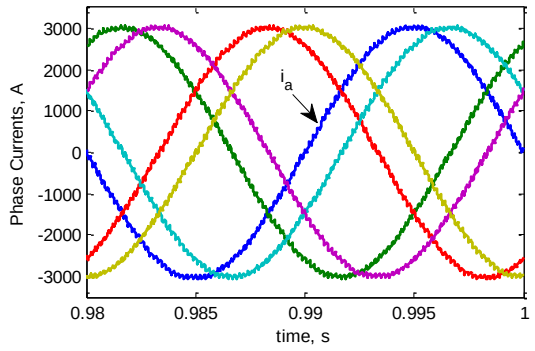

(c)

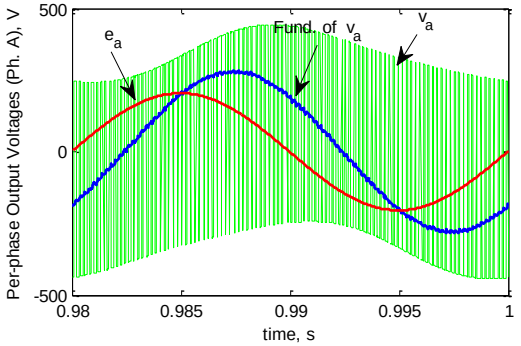

(d)

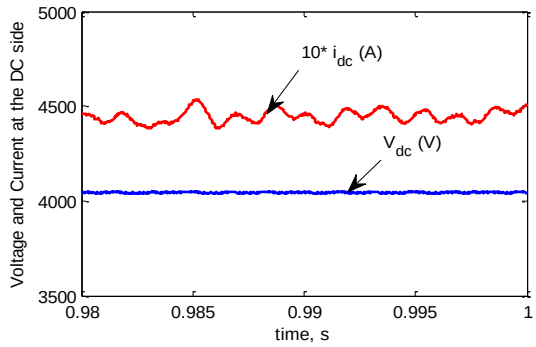

(e)

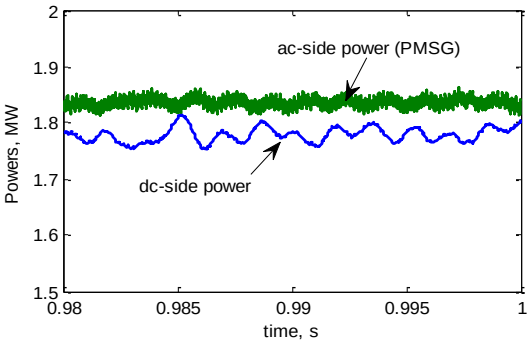

(f)

Figure 54. Simulation results for a low DC-link capacitance (50mF) at rated frequency: (a) Modulating signals of the involved HB converters, (b) DC-link voltages, (c) Phase currents, (d) Per-phase output voltages (phase a), (e) DC voltage and scaled up current at the DC terminals of the proposed architecture, and (f) Input (AC side) and output (DC side) powers.

The output phase voltage and the EMF induced-voltage of Phase '*a*' for both cases are shown in Figure 53(d) and Figure 54(d) as well. It is clear that the fundamental component of the phase voltage (v_a) is identical in both cases, which is expected for the same current reference and per phase machine impedance.

Finally, Figure 53(f) and Figure 54(f) show the machine AC side power and the DC side power in both cases. It is clear that the AC side power is higher than the DC side power as the power flow is from the AC side to the DC side (i.e., rectification mode). The power difference represents the system losses (2.5% losses in the presented case). The DC-side power in case of low capacitance has an oscillatory component as a reflection to the DC current ripple shown in Figure 53(e).

Figure 53(e) and Figure 53(e) show the DC-link voltage and current in both cases. It has to be noted that the converter DC voltage is constant in both cases apart from the capacitance value is low or high. On the other hand, the DC-link current ripple magnitude in case of low capacitance value is higher as expected. Smoother current can be obtained by employing a smoothing reactor at the DC side.

It is worth mentioning that the total capacitor stored energy is likely more important than the absolute capacitance value in order to quantify the capacitor volume from a practical perspective. Practical experience advises that a total capacitor sorted energy of 30-40kJ/MVA is acceptable in designing practical modular multilevel converters

[32], [33]. This energy can be simply calculated from:

$$\boldsymbol{E = \frac{1}{2}\, N_c C\, V_c^2} \tag{6.1}$$

where C is the capacitance, V_c is the average capacitor voltage, and N_c is the total number of capacitors.

For the presented simulation case study, the corresponding energy stored equals approximately 80 kJ/MVA and 20 kJ/MVA for the 200mF and 50mF capacitors, respectively. Hence, the total energy stored in the 50mF case is within the acceptable practical range, while providing an acceptable system performance.

B. System Dynamic Performance

In this subsection, the system dynamic performance is presented assuming a regenerative speed profile, assuming that the machine speed linearly varies from 1pu at t = 1s to 0.8pu at t = 1.1s. The simulation results are shown in Figure 55, assuming a value of 200 mF for all capacitors. Figure 55(a) shows that the magnitude of the modulating signals decreases with the speed reduction. Figure 55(b) shows the effect of the speed reduction on the capacitor voltages.

It is clear that the capacitors' voltage ripple magnitude decreases with the reduction in the phase current (i_q^*) to $(0.8)^2$ pu, as shown in Figure 55(c). Finally, the variation of the AC side and DC side powers are shown in Figure 55(d). The input AC power drops to $(0.8)^3$ pu when speed decreases to 0.8 pu, which is expected as the mechanical power of the PMSG (P_m) is proportional to ω_m^3.

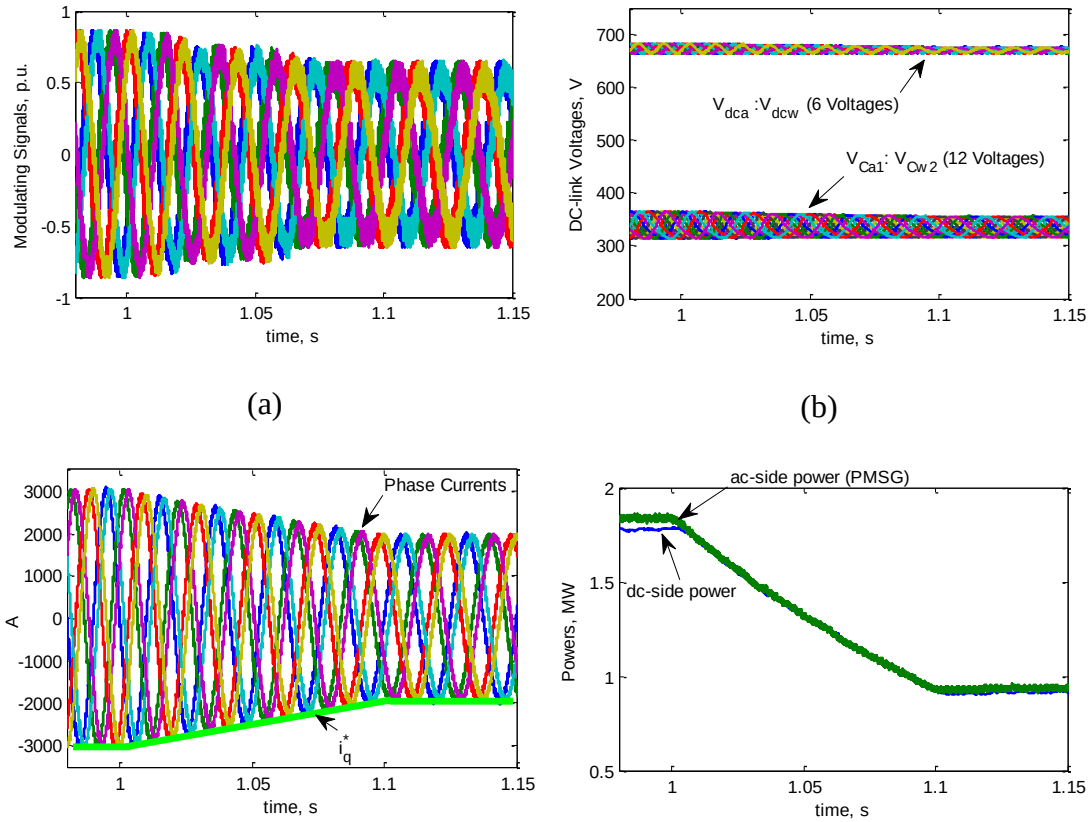

Figure 55. Dynamic performance of the system after reduction of mechanical speed: (a) Modulating signals of the involved HB converters, (b) DC-link voltages, (c) Phase currents, (d) AC side and DC side powers.

CHAPTER 7: CONCLUSIONS AND FUTURE WORK

7.1. Conclusions

In summary, this thesis has focused on the MMC-based MV-ASD applications, mainly subsea oil and gas recovery. The operation of MMC-based motor drives has encountered several challenges as follows:

1) The zero-/low-speed operation of the MMC in case employed in drive systems.
2) The bulkiness of the drive system in medium-voltage levels due to the presence of low-frequency step-up transformation and filter stage at the output.
3) Output torque enhancement.
4) The supply of proper DC-link voltage to the drive system.

Those challenges have been addressed in this thesis. The main challenge is the zero-/low-speed operation of MMC-based ASDs. This thesis introduced an approach for exploiting the additional degrees of freedom of a five-phase machine to enable stable operation of an MMC-based drive system under zero-/low-speed operation. The *x-y* plane's current components are injected under zero-/low-speed operation to enable adequate capacitors voltages balancing. These injected secondary current components are reduced as the machine start to accelerate up to higher speeds. With the given proposed concept, the experimental validation proved that the capacitor voltage could be as low as 5% under very low fundamental frequency. The salient advantages of the proposed technique can be summarized as follows:

1) No additional control algorithm is required as the control of the *x-y* currents is inherited in any multiphase-based drive system.
2) The injected *x-y* currents do not contribute to torque production.

3) Since the injected *x-y* voltage components are only required under low-speed operation, the proposed concept will not affect the converter maximum voltage utilization.
4) The proposed *x-y* injection method is valid for any multiphase machine with distributed stator windings.
5) The proposed technique uses only the output current to perform balancing during zero-/low-speed intervals.
6) Only output current sensors are required.
7) No change in the converter current rating is needed.

Moreover, this thesis deals with the bulkiness of the drive system. A five-phase hybrid-boost MMC-based IM drive was investigated in this thesis as an alternative to the bulky drive systems used in MV applications such as subsea oil and gas recovery. Generally, a stepped AC output voltage with a peak of up to kV_{dc}, where $k > 1$, can be obtained at the output terminals of the (2*k-1*):2 hybrid-boost MMC with a reduced number of semiconductor devices when compared to existing boost MMC configurations. Having a boosting capability results in eliminating the bulky low-frequency step-up transformer. In the presented case study, a hybrid-boost MMC, which contains a combination of FB-SMs and HB-SMs with a ratio of 1:2, is employed. The hybrid-boost MMC is able to deliver an AC output voltage magnitude that is twice the voltage of other medium-voltage MV converters including the conventional MMC (i.e., k=1). The high output quality also eliminates the need for the filtering stage at the output side. In addition, the multiphase machine enhances the drive system fault tolerance capability and reduces the torque ripple at a relatively low switching frequency, which are critical needs for MV applications. The presented drive system exhibited a good performance with low current THD and torque ripples at a relatively

low switching frequency of 2 kHz. The SMs capacitors were balanced with the presented voltage balancing technique. The proposed system was investigated in simulation using MATLAB/Simulink. Then the performance of the 1:2 hybrid-boost MMC was experimentally tested on a downscaled prototype. The obtained experimental results combined with the simulation study demonstrate the good potential for the converter.

Output torque enhancement has been sought in this thesis using the proposed TPD-PWM. A significant torque enhancement can be reached using TPD-PWM of 25.7° slope angle with a THD content close to that obtained using SPD-PWM. Adopting a trapezoidal waveform-based modulation inherently enables the reduction of switching frequencies. Thereafter, an increase of the drive system utilization, reduction of switching losses, and simple implementation of the modulation reference can be obtained.

In order to generate an adequate DC-link voltage levels MV-ASDs, a series-connected multi HB modules-based AFE rectifier has been proposed in this thesis. The proposed approach has sought the generation of high DC-link voltage employing low rating switching devices. For the same AC side voltage, the proposed approach generates a DC-link voltage level three times greater than the voltage generated by conventional two-level fully controlled rectifier, with lower switching devices ratings by 1/3. The simulation case study has addressed the proposed configuration. It has been revealed that a boosted output DC-link voltage of 8 kV can be obtained from a grid peak voltage of 310 V. The proposed control strategy has exhibited fast response providing output voltage ripples of 3.75% and grid current THD of 2.99%.

Generally, a series-connected multi HB-modules with a boosting gain from AC to DC sides equals 2*m*, where *m* is the number of AC sides phases, can be obtained. The

proposed approach can effectively provide a transformerless operation while employing relatively low-voltage semiconductor switches, which enhances system efficiency, simplicity, and cost.

7.2. Future Work

The thesis covered the main challenges of MMC-based drive systems. However, the following points can be considered for further improvement of the system compatibility.

1) Investigating the drive system tolerance during faulty states. As mentioned, the MMC exhibits high reliability due to the possibility of installing redundant SMs that can be equipped during a fault in the converter semiconductor devices. Meanwhile, multiphase machines are well known for their fault tolerance capabilities.
2) Examining the proposed system performance and response to a different number of machine phases experimentally. The proposed systems in this thesis are believed to be applicable to any number of phases above three. The extended study may need to be applied, for instance, to the asymmetrical six-phase machines.
3) Long cables associated with the drive system in specific applications, such as subsea oil and gas recovery, represents a challenge due to the traveling waves and voltage drop. MMC is believed to be suitable to such concerns as its output contains low harmonic content compared to other converters, plus the boosting capabilities proposed in this thesis may cope with the voltage drop concerns. The effect of the long cables on MMC-based MV-ASDs may be investigated experimentally as well as using simulation tools.
4) Integrating a Silicon Carbide (SiC)-based MMC. The proposed systems may benefit the following merits of SiC-based switching devices compared to conventional Si-

counterparts:

- Higher operating temperatures.
- Better output waveforms due to the higher permissible switching frequencies.
- Higher efficiency
- Reducing the number of the converter levels to two levels using high voltage rating of SiC switching devices (up to 15kV).

REFERENCES

[1] X. Liang and O. Ilochonwu, “Passive Harmonic Filter Design Scheme for Subsea Cable Applications with 6-Pulse Variable Frequency Drives,” in *2009 IEEE Energy Conversion Congress and Exposition*, 2009, pp. 597–603.

[2] J. R. Smith, D. M. Grant, A. Al-Mashgari, and R. D. Slater, “Operation of Subsea Electrical Submersible Pumps Supplied Over Extended Length Cable Systems,” in *IEE Proceedings Electric Power Applications*, 2000, vol. 147, pp. 544–552.

[3] S. Demmig, J. Andrews, and R.-D. Klug, “Control of Subsea Motors on Multi-Km Cable Lengths by Variable Frequency Drives,” in *Petroleum and Chemical Industry Conference Europe Electrical and Instrumentation Applications*, 2011, pp. 1–10.

[4] K. Rajashekara, H. S. Krishnamoorthy, and B. S. Naik, “Electrification of Subsea Systems : Requirements and Challenges in Power Distribution and Conversion,” vol. 2, no. 4, 2017.

[5] H. Abu-Rub, J. Holtz, J. Rodriguez, and G. Baoming, “Medium-voltage multilevel converters State of the art, challenges, and requirements in Industrial applications,” *IEEE Trans. Ind. Electron.*, vol. 57, no. 8, pp. 2581–2596, 2010.

[6] J. Rodríguez, J. I. Leon, S. Kouro, R. Portillo, and M. A. M. Prats, “The age of multilevel converters arrives,” no. June, pp. 28–39, 2008.

[7] A. Nabae, I. Takahashi, and H. Akagi, “A New Neutral-Point-Clamped PWM Inverter,” *IEEE Trans. Ind. Appl.*, vol. IA-17, no. 5, pp. 518–523, 1981.

[8] J. Rodríguez, J. S. Lai, and F. Z. Peng, “Multilevel inverters: A survey of topologies, controls, and applications,” *IEEE Trans. Ind. Electron.*, vol. 49, no. 4, pp. 724–738, 2002.

[9] S. S. Fazel, S. Bernet, D. Krug, and K. Jalili, “Design and comparison of 4-kV neutral-point-clamped, flying-capacitor, and series-connected H-bridge multilevel converters,” *IEEE Trans. Ind. Appl.*, vol. 43, no. 4, pp. 1032–1040, 2007.

[10] R. H. Baker and L. H. Bannister, “Electric power converter,” 3 867 643, 1975.

[11] M. Saeedifard, R. Iravani, and J. Pou, “Analysis of a space vector modulated five-level converter,” *2007 IEEE Power Eng. Soc. Gen. Meet. PES*, 2007.

[12] G. T. Son *et al.*, “Design and control of a modular multilevel HVDC converter with redundant power modules for noninterruptible energy transfer,” *IEEE Trans. Power Deliv.*, vol. 27, no. 3, pp. 1611–1619, 2012.

[13] A. Lesnicar and R. Marquardt, “An Innovative Modular Multilevel Converter Topology Suitable for a Wide Power Range,” in *IEEE Bologna Power Tech Conference Proceedings*, 2003, p. 6.

[14] F. Deng and Z. Chen, “Voltage-balancing method for modular multilevel converters under phase-shifted carrier-based pulsewidth modulation,” *IEEE Trans. Ind. Electron.*, vol. 62, no. 7, pp. 4158–4169, 2015.

[15] ABB Oil, Gas, and Chemicals, “INSUBSEA Power and Automation: Expanding capacity, extending lifespan and reducing cost for oil and gas fields,” 2017.

[16] ABB Oil, Gas, and Chemicals, “ABB drives in chemical, oil and gas Medium voltage drives for greater profitability and performance,” 2011.

[17] R. O. Raad, T. Henriksen, H. B. Raphael, and A. Hadler-jacobsen, “Converter-Fed Subsea Motor Drives,” *IEEE Trans. Ind. Appl.*, vol. 32, no. 5, pp. 1069–1079, 1996.

[18] A. A. Hakeem, A. A. Elserougi, A. S. Abdel-khalik, S. Ahmed, and A. M. Massoud, “Performance evaluation of a transformerless multiphase electric

submersible pump system," *J. Eng.*, vol. 2014, no. 8, pp. 407–414, 2014.

[19] A. A. Hakeem, A. Elserougi, A. S. Abdel-Khalik, S. Ahmed, and A. M. Massoud, "Performance of a five-phase boost inverter-fed submersible induction machine," in *2013 IEEE International Electric Machines and Drives Conference, IEMDC 2013*, 2013, pp. 180–187.

[20] S. Kouro et al., "Recent advances and industrial applications of multilevel converters," *IEEE Trans. Ind. Electron.*, vol. 57, no. 8, pp. 2553–2580, 2010.

[21] M. A. Perez, S. Bernet, J. Rodriguez, S. Kouro, and R. Lizana, "Circuit Topologies , Modeling , Control Schemes , and Applications of Modular Multilevel Converters," *IEEE Trans. Power Electron.*, vol. 30, no. 1, pp. 4–17, 2015.

[22] E. Solas, G. Abad, J. A. Barrena, S. Aurtenetxea, A. Cárcar, and L. Zaj, "Modular Multilevel Converter With Different Submodule Concepts — Part II : Experimental Validation and Comparison for HVDC Application," *IEEE Trans. Ind. Electron.*, vol. 60, no. 10, pp. 4536–4545, 2013.

[23] L. Harnefors, A. Antonopoulos, S. Norrga, L. Angquist, and H.-P. Nee, "Dynamic analysis of modular multilevel converters," *IEEE Trans. Ind. Electron.*, vol. 60, no. 7, pp. 2526–2537, 2013.

[24] G. Bergna et al., "An energy-based controller for hvdc modular multilevel converter in decoupled double synchronous reference frame for voltage oscillation reduction," *IEEE Trans. Ind. Electron.*, vol. 60, no. 6, pp. 2360–2371, 2013.

[25] O. Cwikowski, H. R. Wickramasinghe, G. Konstantinou, J. Pou, M. Barnes, and R. Shuttleworth, "Modular Multilevel Converter DC Fault Protection," *IEEE Trans. Power Deliv.*, vol. 33, no. 1, pp. 291–300, 2018.

[26] S. Debnath, J. Qin, B. Bahrani, M. Saeedifard, and P. Barbosa, “Operation, control, and applications of the modular multilevel converter: A review,” *IEEE Trans. Power Electron.*, vol. 30, no. 1, pp. 37–53, 2015.

[27] N. Celanovic and D. Boroyevich, “A fast space-vector modulation algorithm for multilevel three-phase converters,” *IEEE Trans. Ind. Appl.*, vol. 37, no. 2, pp. 637–641, 2001.

[28] Jih-Sheng Lai and Fang Zheng Peng, “Multilevel converters-a new breed of power converters,” *IEEE Trans. Ind. Appl.*, vol. 32, no. 3, pp. 509–517, 1996.

[29] M. F. Aiello, P. W. Hammond, and M. Rastogi, “Modular multi-level adjustable supply with parallel connected active inputs,” 6 301 130, 2001.

[30] G. P. Adam, O. Anaya-Lara, G. M. Burt, D. Telford, B. W. Williams, and J. R. McDonald, “Modular multilevel inverter: pulse width modulation and capacitor balancing technique,” *IET Power Electron.*, vol. 3, no. 5, pp. 702–715, 2010.

[31] S. Busquets-Monge, J. Bordonau, and J. Rocabert, “A Virtual-Vector Pulse width Modulation for the Four-Level Diode-Clamped DC–AC Converter,” *Ieee Trans. Power Electron.*, vol. 23, no. 4, pp. 1964–1972, 2008.

[32] S. D. G. Jayasinghe, D. M. Vilathgamuwa, and U. K. Madawala, “Diode-clamped three-level inverter-based battery/supercapacitor direct integration scheme for renewable energy systems,” *IEEE Trans. Power Electron.*, vol. 26, no. 12, pp. 3720–3729, 2011.

[33] Y. Cheng, C. Qian, M. L. Crow, S. Pekarek, and S. Atcitty, “A comparison of diode-clamped and cascaded multilevel converters for a STATCOM with energy storage,” *IEEE Trans. Ind. Electron.*, vol. 53, no. 5, pp. 1512–1521, 2006.

[34] P. Lezana, R. Aguilera, and D. E. Quevedo, “Model predictive control of an asymmetric flying capacitor converter,” *IEEE Trans. Ind. Electron.*, vol. 56, no.

6, pp. 1839–1846, 2009.

[35] B. Chong, L. Zhang, and M. J. Waite, “Three-phase four-leg flying-capacitor multi-level inverter-based active power filter for unbalanced current operation,” *IET Power Electron.*, vol. 6, no. 1, pp. 153–163, 2013.

[36] A. M. Y. M. Ghias, J. Pou, V. G. Agelidis, and M. Ciobotaru, “Voltage balancing method for a flying capacitor multilevel converter using phase disposition PWM,” *IEEE Trans. Ind. Electron.*, vol. 61, no. 12, pp. 6538–6546, 2014.

[37] Y. Yu, G. Konstantinou, B. Hredzak, and V. G. Agelidis, “Power Balance of Cascaded H-Bridge Multilevel Converters for Large-Scale Photovoltaic Integration,” *IEEE Trans. Power Electron.*, vol. 31, no. 1, pp. 292–303, 2016.

[38] K.-M. Tsang and W.-L. Chan, “Multi-level multi-output single-phase active rectifier using cascaded H-bridge converter,” *IET Power Electron.*, vol. 7, no. 4, pp. 784–794, 2014.

[39] S. Vazquez *et al.*, “Analysis of the power balance in the cells of a multilevel cascaded H-bridge converter,” *IEEE Trans. Ind. Electron.*, vol. 57, no. 7, pp. 2287–2296, 2010.

[40] R. Marquardt, “Modular Multilevel Converter : An universal concept for HVDC-Networks and extended DC-Bus-applications,” in *The 2010 International Power Electronics Conference - ECCE ASIA -*, 2010, pp. 502–507.

[41] K. Friedrich, “Modern HVDC PLUS application of VSC in Modular Multilevel Converter Topology,” in *2010 IEEE International Symposium on Industrial Electronics*, 2010, pp. 3807–3810.

[42] M. Saeedifard and R. Iravani, “Dynamic Performance of a Modular Multilevel back-to-back HVDC system,” *IEEE Trans. Power Deliv.*, vol. 25, no. 4, pp. 2903–2912, 2010.

[43] M. Guan and Z. Xu, “Modeling and Control of a Modular Multilevel Converter-Based HVDC System Under Unbalanced Grid Conditions,” *IEEE Trans. Power Electron.*, vol. 27, no. 12, pp. 4858–4867, 2012.

[44] K. Sekiguchi, P. Khamphakdi, S. Member, and M. Hagiwara, “A Grid-Level High-Power BTB (Back-To-Back) System Using Modular Multilevel Cascade Converters Without Common DC-Link Capacitor,” *IEEE Trans. Ind. Appl.*, vol. 50, no. 4, pp. 2648–2659, 2014.

[45] J. Eralta, H. Saad, S. Member, S. Dennetière, J. Mahseredjian, and S. Nguefeu, “Detailed and Averaged Models for a 401-level MMC–HVDC System,” *IEEE Trans. Power Deliv.*, vol. 27, no. 3, pp. 1501–1508, 2012.

[46] A. Elserougi, A. Massoud, and S. Ahmed, “A Switched-Capacitor Submodule for Modular Multilevel HVDC Converters With DC-Fault Blocking Capability and a Reduced Number of Sensors,” *IEEE Trans. Power Deliv.*, vol. 31, no. 1, pp. 313–322, 2016.

[47] K. Ilves, A. Antonopoulos, L. Harnefors, S. Norrga, and H. Nee, “Circulating Current Control in Modular Multilevel Converters with Fundamental Switching Frequency,” in *2012 IEEE 7th International Power Electronics and Motion Control Conference - ECCE Asia*, 2012, pp. 249–256.

[48] D. Schmitt, Y. Wang, T. Weyh, and R. Marquardt, “DC-Side Fault Current Management in extended Multiterminal-HVDC-Grids,” in *International Multi-Conference on Systems, Signals & Devices*, 2012, pp. 1–5.

[49] E. Solas, G. Abad, J. A. Barrena, S. Aurtenetxea, A. Cárcar, and L. Zaj, “Modular Multilevel Converter With Different Submodule Concepts — Part I : Capacitor Voltage Balancing Method,” *IEEE Trans. Ind. Electron.*, vol. 60, no. 10, pp. 4525–4535, 2013.

[50] G. P. Adam, K. H. Ahmed, and B. W. Williams, “Mixed cells modular multilevel converter,” in *2014 IEEE 23rd International Symposium on Industrial Electronics (ISIE)*, 2014, pp. 1390–1395.

[51] R. Zeng *et al.*, “Design and Operation of a Hybrid Modular Multilevel Converter,” *IEEE Trans. Power Electron.*, vol. 30, no. 3, pp. 1137–1146, 2015.

[52] M. Daoud, A. Elserougi, A. Massoud, R. Bojoi, A. S. Abdel-khalik, and S. Ahmed, “Zero- / Low-Speed Operation of Multiphase Drive Systems with Modular Multilevel Converters,” *IEEE Access*, vol. 7, pp. 14353–14365, 2019.

[53] S. Debnath and M. Saeedifard, “A new hybrid modular multilevel converter for grid connection of large wind turbines,” *IEEE Trans. Sustain. Energy*, vol. 4, no. 4, pp. 1051–1064, 2013.

[54] M. I. Daoud, A. Massoud, A. Elserougi, A. Abdel-Khalik, and S. Ahmed, “A dual three-phase induction machine based flywheel storage system driven by modular multilevel converters for fault ride through in HVDC systems,” in *Asia-Pacific Power and Energy Engineering Conference, APPEEC*, 2015, pp. 1–5.

[55] M. Moranchel, E. J. Bueno, F. J. Rodriguez, and I. Sanz, “Implementation of nearest level modulation for Modular Multilevel Converter,” in *2015 IEEE 6th International Symposium on Power Electronics for Distributed Generation Systems, PEDG 2015*, 2015, pp. 1–5.

[56] M. I. Daoud, A. Massoud, A. Abdel-Khalik, and S. Ahmed, “An asymmetrical six-phase induction machine-based flywheel energy storage system using modular multilevel converters,” in *19th International Conference on Electrical Machines and Systems, ICEMS 2016*, 2016, pp. 1–6.

[57] M. Hagiwara and H. Akagi, “Control and Experiment of Pulsewidth-Modulated Modular Multilevel Converters,” *IEEE Trans. Power Electron.*, vol. 24, no. 7,

pp. 1737–1746, 2009.

[58] S. Rohner, S. Bernet, M. Hiller, and R. Sommer, “Modulation, losses, and semiconductor requirements of modular multilevel converters,” *IEEE Trans. Ind. Electron.*, vol. 57, no. 8, pp. 2633–2642, 2010.

[59] M. Daoud, A. Massoud, A. Elserougi, A. S. Abdel-Khalik, and S. Ahmed, “Sensor-less operation of hybrid boost modular multilevel converter for subsea multiphase medium voltage drives,” in *3rd IEEE Southern Power Electronics Conference, SPEC 2017*, 2017, pp. 1–5.

[60] E. Levi, R. Bojoi, F. Profumo, H. A. Toliyat, and S. Williamson, “Multiphase induction motor drives – a technology status review,” *IET Electr. Power Appl.*, vol. 1, no. 4, pp. 489–516, 2007.

[61] A. Cavagnino, Z. Li, A. Tenconi, and S. Vaschetto, “Integrated generator for more electric engine: Design and testing of a scaled-size prototype,” *IEEE Trans. Ind. Appl.*, vol. 49, no. 5, pp. 2034–2043, 2013.

[62] G. Sulligoi, A. Tessarolo, V. Benucci, A. Millerani Trapani, M. Baret, and F. Luise, “Shipboard power generation: Design and development of a medium-voltage dc generation system,” *IEEE Ind. Appl. Mag.*, vol. 19, no. 4, pp. 47–55, 2013.

[63] E. Levi, “Advances in converter control and innovative exploitation of additional degrees of freedom for multiphase machines,” *IEEE Trans. Ind. Electron.*, vol. 63, no. 1, pp. 433–448, 2016.

[64] M. Bermudez, I. Gonzalez-Prieto, F. Barrero, H. Guzman, X. Kestelyn, and M. J. Duran, “An Experimental Assessment of Open-Phase Fault-Tolerant Virtual-Vector-Based Direct Torque Control in Five-Phase Induction Motor Drives,” *IEEE Trans. Power Electron.*, vol. 33, no. 3, pp. 2774–2784, 2018.

[65] H. Guzman, M. J. Duran, F. Barrero, B. Bogado, and S. Toral, “Speed control of five-phase induction motors with integrated open-phase fault operation using model-based predictive current control techniques,” *IEEE Trans. Ind. Electron.*, vol. 61, no. 9, pp. 4474–4484, 2014.

[66] M. J. Duran, I. Gonzalez-Prieto, F. Barrero, E. Levi, L. Zarri, and M. Mengoni, “A simple braking method for six-phase induction motor drives with unidirectional power flow in the base-speed region,” *IEEE Trans. Ind. Electron.*, vol. 64, no. 8, pp. 6032–6041, 2017.

[67] I. González-Prieto, M. J. Duran, N. Rios-Garcia, F. Barrero, and C. Martín, “Open-Switch Fault Detection in Five-Phase Induction Motor Drives Using Model Predictive Control,” *IEEE Trans. Ind. Electron.*, vol. 65, no. 4, pp. 3045–3055, 2018.

[68] A. Tessarolo, G. Zocco, and C. Tonello, “Design and Testing of a 45-MW 100-Hz Quadruple-Star Synchronous Motor for a Liquefied Natural Gas Turbo-Compressor Drive,” *IEEE Trans. Ind. Appl.*, vol. 47, no. 3, pp. 1210–1219, 2011.

[69] O. Nagura, M. Higuchi, K. Tani, and T. Oyake, “Hitachi’s adjustable-speed pumped storage system contributing to prevention of global warming,” *Hitachi Rev.*, vol. 59, no. 3, pp. 99–105, 2010.

[70] B. Li, S. Zhou, D. Xu, S. J. Finney, and B. W. Williams, “A Hybrid Modular Multilevel Converter for Medium-Voltage Variable-Speed Motor Drives,” *IEEE Trans. Power Electron.*, vol. 32, no. 6, pp. 4619–4630, 2017.

[71] S. Du, B. Wu, K. Tian, N. Zargari, and Z. Cheng, “An Active Cross-Connected Modular Multilevel Converter (AC-MMC) for Medium-Voltage Motor Drive,” *IEEE Trans. Ind. Electron.*, vol. 63, no. 8, pp. 4707–4717, 2016.

[72] A. Antonopoulos, L. Angquist, L. Harnefors, and H. Nee, “Optimal Selection of

the Average Capacitor Voltage for Variable-Speed Drives With Modular Multilevel Converters," *IEEE Trans. Power Electron.*, vol. 30, no. 1, pp. 227–234, 2015.

[73] B. Tai, C. Gao, X. Liu, and Z. Chen, "A Novel Flexible Capacitor Voltage Control Strategy for Variable-Speed Drives With Modular Multilevel Converters," *IEEE Trans. Power Electron.*, vol. 32, no. 1, pp. 128–141, 2017.

[74] S. Du, B. Wu, and N. R. Zargari, "A Star-Channel Modular Multilevel Converter for Zero / Low-Fundamental-Frequency Operation Without Injecting Common-Mode Voltage," *IEEE Trans. Power Electron.*, vol. 33, no. 4, pp. 2857–2865, 2018.

[75] M. Hagiwara, K. Nishimura, and H. Akagi, "A Medium-Voltage Motor Drive With a Modular Multilevel PWM Inverter," *IEEE Trans. Power Electron.*, vol. 25, no. 7, pp. 1786–1799, 2010.

[76] S. Debnath, J. Qin, and M. Saeedifard, "Control and Stability Analysis of Modular Multilevel Converter Under Low-Frequency Operation," *IEEE Trans. Ind. Electron.*, vol. 62, no. 9, pp. 5329–5339, 2015.

[77] J. Kolb, F. Kammerer, M. Gommeringer, and M. Braun, "Cascaded Control System of the Modular Multilevel Converter for Feeding Variable-Speed Drives," *IEEE Trans. Power Electron.*, vol. 30, no. 1, pp. 349–357, 2015.

[78] K. Wang, Y. Li, Z. Zheng, and L. Xu, "Voltage Balancing and Fluctuation-Suppression Methods of Floating Capacitors in a New Modular Multilevel Converter," *IEEE Trans. Ind. Electron.*, vol. 60, no. 5, pp. 1943–1954, 2013.

[79] A. Antonopoulos, L. Ängquist, S. Norrga, K. Ilves, L. Harnefors, and H. P. Nee, "Modular Multilevel Converter AC Motor Drives With Constant Torque From Zero to Nominal Speed," *IEEE Trans. Ind. Appl.*, vol. 50, no. 3, pp. 1982–1993,

2014.

[80] M. Hagiwara, I. Hasegawa, and H. Akagi, “Start-Up and Low-Speed Operation of an Electric Motor Driven by a Modular Multilevel Cascade Inverter,” *IEEE Trans. Ind. Appl.*, vol. 49, no. 4, pp. 1556–1565, 2013.

[81] B. Li *et al.*, “An Improved Circulating Current Injection Method for Modular Multilevel Converters in Variable-Speed Drives,” *IEEE Trans. Ind. Electron.*, vol. 63, no. 11, pp. 7215–7225, 2016.

[82] Y. S. Kumar and G. Poddar, “Medium-Voltage Vector Control Induction Motor Drive at Zero Frequency Using Modular Multilevel Converter,” *IEEE Trans. Ind. Electron.*, vol. 65, no. 1, pp. 125–132, 2018.

[83] H. Akagi, “Classification, Terminology, and Application of The Modular Multilevel Cascade Converter (MMCC),” in *The 2010 International Power Electronics Conference - ECCE ASIA -*, 2011, vol. 26, no. 11, pp. 3119–3130.

[84] Y. N. Tatte and M. V. Aware, “Torque Ripple and Harmonic Current Reduction in a Three-Level Inverter-Fed Direct-Torque-Controlled Five-Phase Induction Motor,” *IEEE Trans. Ind. Electron.*, vol. 64, no. 7, pp. 5265–5275, 2017.

[85] Y. N. Tatte and M. V. Aware, “Direct Torque Control of Five-Phase Induction Motor With Common-Mode Voltage and Current Harmonics Reduction,” *IEEE Trans. Power Electron.*, vol. 32, no. 11, pp. 8644–8654, 2017.

[86] A. S. Abdel-khalik, S. Ahmed, and A. M. Massoud, “Steady-State Mathematical Modeling of a Five-Phase Induction Machine With a Combined Star / Pentagon Stator Winding Connection,” *IEEE Trans. Ind. Electron.*, vol. 63, no. 3, pp. 1331–1343, 2016.

[87] A. S. Abdel-khalik, M. I. Daoud, S. Ahmed, A. A. Elserougi, and A. M. Massoud, “Parameter Identification of Five-Phase Induction Machines With

Single Layer Windings," *IEEE Trans. Ind. Electron.*, vol. 61, no. 10, pp. 5139–5154, 2014.

[88] R. Zeng, L. Xu, L. Yao, and D. J. Morrow, "Precharging and dc fault ride-Through of hybrid MMC-based HVDC systems," *IEEE Trans. Power Deliv.*, vol. 30, no. 3, pp. 1298–1306, 2015.

[89] A. Elserougi et al., "A Transformerless STATCOM Based on a Hybrid Boost Modular Multilevel Converter with Reduced Number of Switches," *Electr. Power Syst. Res.*, vol. 146, pp. 341–348, 2017.

[90] A. Elserougi et al., "Power control of grid-connected high-gain boost full-bridge modular multilevel converter," in *IEEE Southern Power Electronics Conference (SPEC)*, 2017, pp. 1–5.

[91] T. Nakanishi and J. I. Itoh, "High Power Density Design for a Modular Multilevel Converter with an H-Bridge Cell Based on a Volume Evaluation of Each Component," *IEEE Trans. Power Electron.*, vol. 33, no. 3, pp. 1967–1984, 2018.

[92] J. E. Huber and J. W. Kolar, "Optimum number of cascaded cells for high-power medium-voltage multilevel converters," in *2013 IEEE Energy Conversion Congress and Exposition, ECCE 2013*, 2013, pp. 359–366.

[93] A. Perez-Basante, S. Ceballos, G. Konstantinou, J. Pou, J. Andreu, and I. M. de Alegria, "(2N+1) Selective Harmonic Elimination-PWM for Modular Multilevel Converters: A Generalized Formulation and A Circulating Current Control Method," *IEEE Trans. Power Electron.*, vol. 33, no. 1, pp. 802–818, 2017.

[94] R. Picas, S. Ceballos, J. Pou, J. Zaragoza, G. Konstantinou, and V. G. Agelidis, "Closed-Loop Discontinuous Modulation Technique for Capacitor Voltage Ripples and Switching Losses Reduction in Modular Multilevel Converters,"

IEEE Trans. Power Electron., vol. 30, no. 9, pp. 4714–4725, 2015.

[95] S. M. Kim, M. G. Jeong, J. Kim, and K. B. Lee, "Hybrid Modulation Scheme for Switching Loss Reduction in a Modular Multilevel High-voltage Direct Current Converter," *IEEE Trans. Power Electron.*, 2018.

[96] A. Mertens and J. Kucka, "Quasi Two-Level PWM Operation of an MMC Phase Leg with Reduced Module Capacitance," *IEEE Trans. Power Electron.*, vol. 31, no. 10, pp. 6765–6769, 2016.

[97] I. A. Gowaid, G. P. Adam, A. M. Massoud, S. Ahmed, D. Holliday, and B. W. Williams, "Quasi two-level operation of modular multilevel converter for use in a high-power DC transformer with DC fault isolation capability," *IEEE Trans. Power Electron.*, vol. 30, no. 1, pp. 108–123, 2015.

[98] I. A. Gowaid, G. P. Adam, S. Ahmed, D. Holliday, and B. W. Williams, "Analysis and Design of a Modular Multilevel Converter With Trapezoidal Modulation for Medium and High Voltage DC-DC Transformers," *IEEE Trans. Power Electron.*, vol. 30, no. 10, pp. 5439–5457, 2015.

[99] C. C. Scharlau, L. F. A. Pereira, L. A. Pereira, and S. Haffner, "Performance of a five-phase induction machine with optimized air gap field under open loop V/f control," *IEEE Trans. Energy Convers.*, vol. 23, no. 4, pp. 1046–1056, 2008.

[100] F. Bu, H. Liu, W. Huang, H. Xu, and K. Shi, "Optimal-Third-Harmonic-Injection-Based Control for a Five-Phase Dual Stator-Winding Induction Generator DC Generating System," *IEEE Trans. Ind. Electron.*, vol. 65, no. 11, pp. 9124–9134, 2018.

[101] P. J. Sotorrio-Ruiz, F. J. Sanchez-Pacheco, F. M. Perez-Hidalgo, and J. R. Heredia-Larrubia, "Modulation of a trapezoidal signal: improving signal quality and reducing costs in power inverters," *IET Power Electron.*, vol. 10, no. 5, pp.

568–576, 2016.

[102] S. Joryo, K. Tatsumi, T. Morizane, K. Taniguchi, N. Kimura, and H. Omori, “Study of Torque ripple reduction and Torque boost by Modified Trapezoidal Modulation,” in *2018 International Power Electronics Conference, IPEC-Niigata - ECCE Asia 2018*, 2018, pp. 1202–1205.

[103] K. Tatsumi, N. Kimura, K. Taniguchi, T. Morizane, and H. Omori, “Wind power generation with modified trapezoidal modulation converter for DC connected offshore wind farms,” in *International Conference on Electical Drives and Power Electronics*, 2017, pp. 153–158.

[104] A. Şchiop and D. Trip, “Analysis of the trapezoidal modulation for current source inverters,” in *ISSCS 2007 - International Symposium on Signals, Circuits and Systems, Proceedings*, 2007, pp. 1–4.

[105] A. Agarwal and V. Agarwal, “Harmonic reduction in AC to AC converter by trapezoidal modulation technique,” in *2009 International Conference on Power Systems, ICPS ’09*, 2009, pp. 1–6.

[106] N. Prabaharan and K. Palanisamy, “Comparative analysis of symmetric and asymmetric reduced switch MLI topologies using unipolar pulse width modulation strategies,” *IET Power Electron.*, vol. 9, no. 15, pp. 2808–2823, 2016.

[107] N. Prabaharan, Z. B. Salam, and K. Palanisamy, “A hybrid multilevel inverter with reduced power electronic components with unipolar trapezoidal pulse width modulation,” in *IEEE Conference on Energy Conversion (CENCON)*, 2017, pp. 283–287.

[108] G. Asplund, “Tapping power from a HVDC transmission system,” US Patent US2010/0091527A1, 2016.

[109] N. D. Dao and D. Lee, “Operation and Control Scheme of a Five-level Hybrid Inverter for Medium Voltage Motor Drives,” *IEEE Trans. Power Electron.*, vol. 33, no. 12, pp. 10178–10187, 2018.

[110] H. Akagi and K. Isozaki, “A Hybrid Active Filter for a Three-Phase 12-Pulse Diode Rectifier Used as the Front End of a Medium-Voltage Motor Drive,” *IEEE Trans. Power Electron.*, vol. 27, no. 1, pp. 69–77, 2012.

[111] D. M. Vilathgamuwa and S. D. G. Jayasinghe, “Rectifier Systems for Variable Speed Wind Generation – A Review,” in *2012 IEEE International Symposium on Industrial Electronics ISIE*, 2012, pp. 1058–1065.

[112] J. W. Kolar and T. Friedli, “The Essence of Three-Phase PFC Rectifier Systems — Part I,” *IEEE Trans. Power Electron.*, vol. 28, no. 1, pp. 176–198, 2013.

[113] T. B. Soeiro and J. W. Kolar, “Analysis of High-Efficiency Three-Phase Two- and Three-Level Unidirectional Hybrid Rectifiers,” *IEEE Trans. Ind. Electron.*, vol. 60, no. 9, pp. 3589–3601, 2013.

[114] S. D. G. Jayasinghe and D. M. Vilathgamuwa, “An Analysis on the Possibility of Using Capacitors of a Three-Level Capacitor Clamped Inverter as Power Smoothing Elements for Wind Power Systems,” in *2011 IEEE Energy Conversion Congress and Exposition ECCE*, 2011, pp. 2963–2970.

[115] J. R. Rodríguez, J. W. Dixon, J. R. Espinoza, J. Pontt, and P. Lezana, “PWM regenerative rectifiers: State of the art,” *IEEE Trans. Ind. Electron.*, vol. 52, no. 1, pp. 5–22, 2005.

[116] P. Samuel, R. Gupta, and D. Chandra, “Grid Interface of Wind Power With Large Split-Winding Alternator Using Cascaded Multilevel Inverter,” *IEEE Trans. Energy Convers.*, vol. 26, no. 1, pp. 299–309, 2011.

[117] H. Iman-Eini, J. Schanen, S. Farhangi, and S. Wang, “Design of Cascaded H-

Bridge Rectifier for Medium Voltage Applications," in *IEEE Power Electronics Specialists Conference*, 2007, pp. 653–658.

[118] J. Wen and K. M. Smedley, "Hexagram Rectifier – Active Front End of Hexagram Inverter for Medium Voltage Variable Speed Drives," in *IEEE/PES Transmission and Distribution Conference and Exposition*, 2008, pp. 1–8.

[119] G. J. M. De Sousa, A. d. S. Dias, J. A. Alves, and M. L. Heldwein, "Modeling and Control of a Modular Multilevel Converter for Medium Voltage Drives Rectifier Applications," in *2015 IEEE 24th International Symposium on Industrial Electronics (ISIE)*, 2015, pp. 1080–1087.

[120] A. A. Elserougi, M. I. Daoud, A. S. Abdel-khalik, A. M. Massoud, and S. Ahmed, "Series-connected multi-half-bridge modules converter for integrating multi-megawatt wind multi-phase permanent magnet synchronous generator with dc grid," *IET Electr. Power Appl.*, vol. 11, no. 6, pp. 981–990, 2017.

[121] A. A. Elserougi, A. Massoud, and S. Ahmed, "A Grid-Connected Capacitor-Tapped Multi- Module Converter for HVDC Applications : Operational Concept and Control," *IEEE Trans. Ind. Appl.*, vol. 54, no. 5, pp. 5523–5535, 2018.

[122] A. EL-Refaie, "Fractional-slot concentrated-windings synchronous permanent magnet machines: Opportunities and challenges," *IEEE Trans. Ind. Electron.*, vol. 57, no. 1, pp. 107–121, 2010.

[123] A. C. Williamson, E. Spooner, and L. Thompson, "Large modular PM generators," *IEE Colloq. New Topol. Perm. Magn. Mach.*, vol. (Digest No, pp. 1–6, 1997.

[124] S. Jia, J. L. Ronghai Qu, X. Fan, and M. Zhang, "Study of Direct-Drive Permanent-Magnet Synchronous Generators With Solid Rotor Back Iron and Different Windings," *IEEE Trans. Ind. Appl.*, vol. 52, no. 2, pp. 1369–1379,

2016.

[125] M. Ebrahimi and A. Khajehoddin, “A simple DQ current controller for single-phase grid-connected inverters,” in *2015 IEEE Applied Power Electronics Conference and Exposition (APEC)*, 2015, pp. 2840–2845.

APPENDIX

Appendix A: Five-Phase IM Mathematical Model

$$v_{\alpha s} = r_s i_{\alpha s} + p\lambda_{\alpha s} - \omega_s \lambda_{\beta S} \quad \text{(A.1)}$$

$$v_{\beta s} = r_s i_{\beta s} + p\lambda_{\beta s} + \omega_s \lambda_{\alpha S} \quad \text{(A.2)}$$

$$v_{\alpha r} = 0 = r_r i_{\alpha r} + p\lambda_{\alpha r} - (\omega_s - \omega_r)\lambda_{\beta r} \quad \text{(A.3)}$$

$$v_{\beta r} = 0 = r_r i_{\beta r} + p\lambda_{\beta r} + (\omega_s - \omega_r)\lambda_{\alpha r} \quad \text{(A.4)}$$

$$v_{xs} = r_s i_{xs} + p\lambda_{xs} \quad \text{(A.5)}$$

$$v_{ys} = r_s i_{ys} + p\lambda_{ys} \quad \text{(A.6)}$$

$$\lambda_{\alpha s} = (L_{ls} + L_M) i_{\alpha s} + L_M i_{\alpha r} \quad \text{(A.7)}$$

$$\lambda_{\beta s} = (L_{ls} + L_M) i_{\beta s} + L_M i_{\beta r} \quad \text{(A.8)}$$

$$\lambda_{\alpha r} = (L_{lr} + L_M) i_{\alpha r} + L_M i_{\alpha s} \quad \text{(A.9)}$$

$$\lambda_{\beta r} = (L_{lr} + L_M) i_{\beta r} + L_M i_{\beta s} \quad \text{(A.10)}$$

$$\lambda_{xs} = L_{ls} i_{xs} \quad \text{(A.11)}$$

$$\lambda_{ys} = L_{ls} i_{ys} \quad \text{(A.12)}$$

Where L_{ls} is stator leakage inductance, L_{lr} is rotor leakage inductance. L_M is magnetizing inductance, $\lambda_{\alpha s}$ is alpha-axis stator flux linkage, $\lambda_{\beta s}$ is beta-axis stator flux linkage, $\lambda_{\alpha r}$ is alpha-axis rotor flux linkage, $\lambda_{\beta r}$ is beta-axis rotor flux linkage, r_s is stator resistance, r_r is rotor resistance, p is the derivative operator, ω_s is stator angular frequency, ω_r is rotor angular frequency.

Appendix B: Samples of Simulink Models

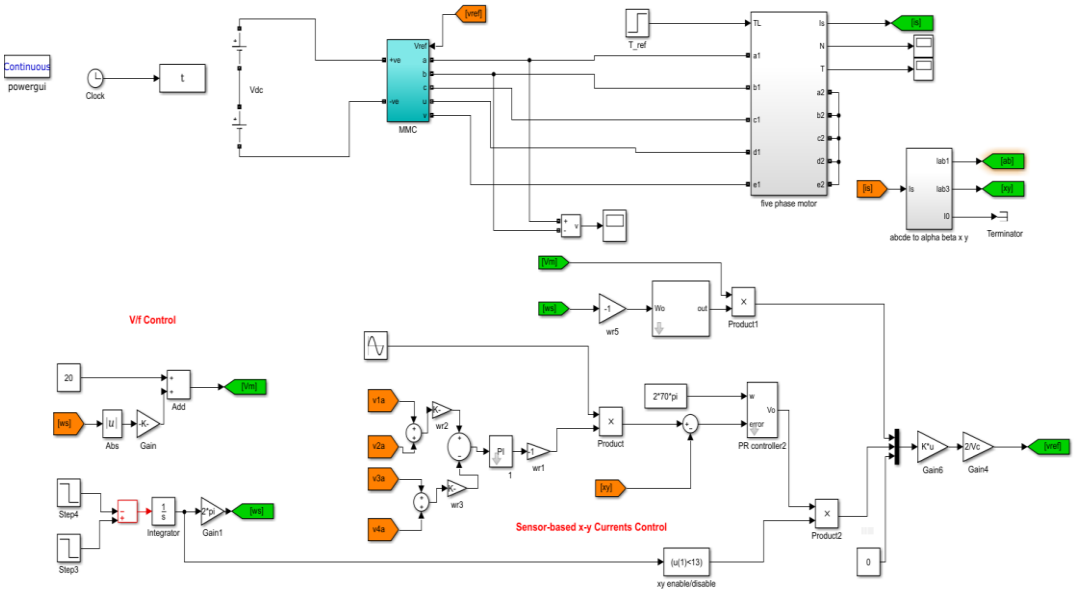

(a)

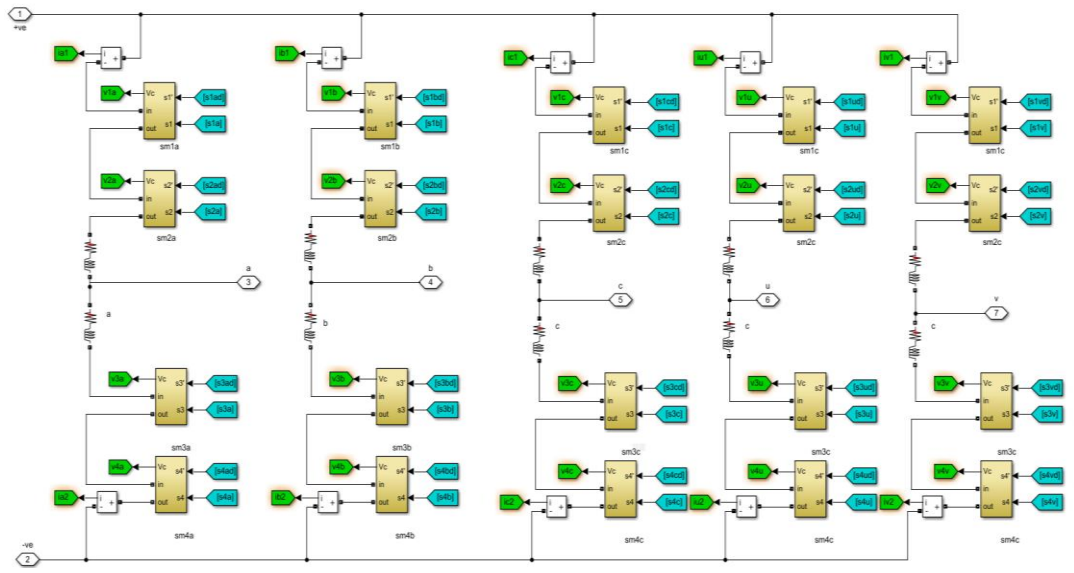

(b)

Figure B.1. Simulation of *x-y* Sensor-based Control. (a) Overall Simulink Model, (b) MMC Model.

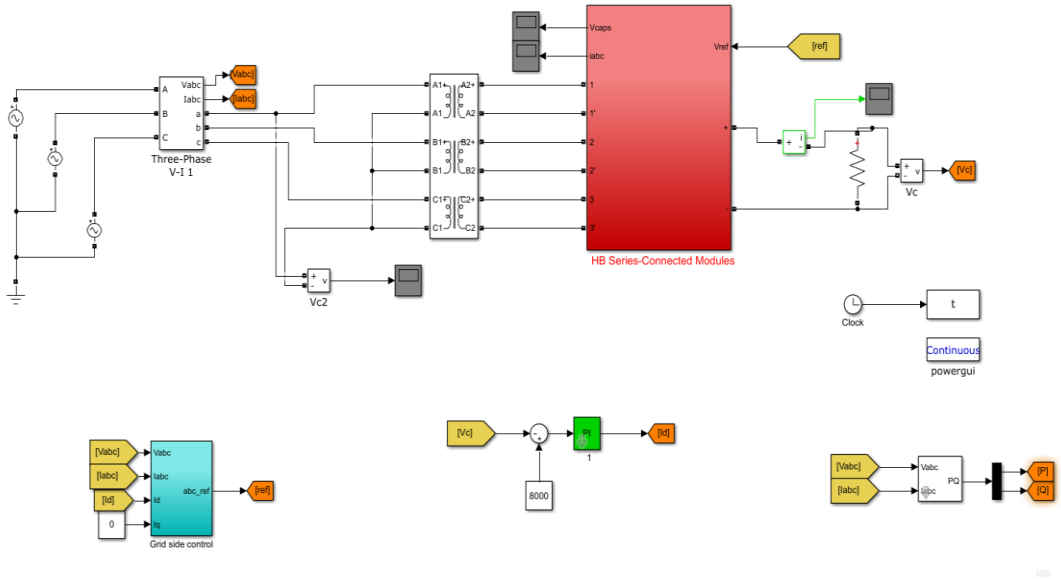

(a)

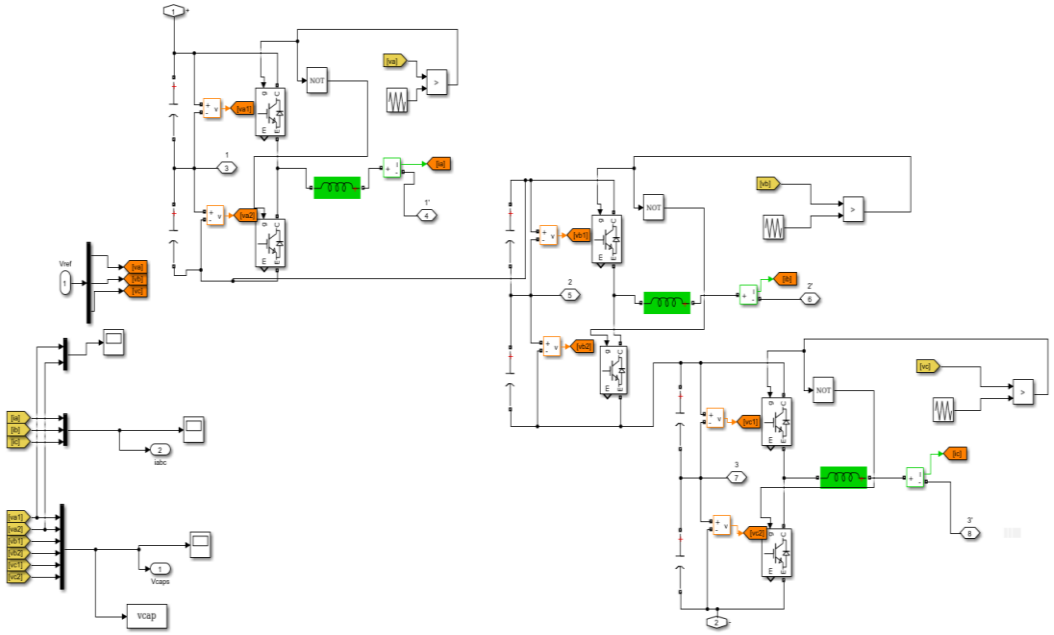

(b)

Figure B.2. Simulation of Series-Connected HB-Modules AFE. (a) Overall AFE Rectifier Simulink Model, (b) HB Series-Connected Modules Converter.

Appendix C: Student's Publications during the Course of the Ph.D.

1) M. I. Daoud, A. Elserougi, A. Massoud, R. Bojoi, A. S. Abdel-Khalik and S. Ahmed, "Zero-/Low-Speed Operation of Multiphase Drive Systems with Modular Multilevel Converters," in IEEE ACCESS, vol. 7, pp. 14353-14365, 2019.
2) M. I. Daoud, A. Elserougi, A. Massoud, R. Bojoi, A. S. Abdel-Khalik and S. Ahmed, "Investigation of Hybrid-Boost Modular Multilevel Converter-Based Medium-Voltage Multiphase Induction Motor Drive for Subsea Applications" Accepted in Journal of Power Electronics, Jan. 2019.
3) M. I. Daoud, A. Massoud, R. Bojoi, A. S. Abdel-Khalik, A. Elserougi, and S. Ahmed, "Torque Enhancement in MMC-based Five-Phase Induction Motor Drives using Trapezoidal Modulation Technique" Under Review, April 2019.
4) A. Elserougi, M. I. Daoud, A. S. Abdel-Khalik, A. Mohamed Massoud and S. Ahmed, "Series-connected multi-half-bridge modules converter for integrating multi-megawatt wind multi-phase permanent magnet synchronous generator with dc grid," IET Electric Power Applications, vol. 11, no. 6, pp. 981-990, 7 2017.
5) M. I. Daoud, A. Elserougi, A. Massoud, R. Bojoi, and S. Ahmed, "Series-Connected Multi-Half-Bridge Modules Active Front-End Rectifier for Medium Voltage Variable Speed Drives", 21st International Conference on Electrical Machines and Systems (ICEMS), Jeju, 2018, pp. 2436-2440.
6) M. I. Daoud, A. Massoud, A. Elserougi, A. S. Abdel-Khalik, and S. Ahmed, "Sensor-less Operation of Hybrid Boost Modular Multilevel Converter for Subsea Multiphase Medium Voltage Drives," 2017 IEEE Southern Power Electronics Conference (SPEC), Puerto Varas, 2017, pp. 1-5.
7) M. I. Daoud, A. Massoud, A. Abdel-Khalik and S. Ahmed, "An Asymmetrical Six-

Phase Induction Machine-Based Flywheel Energy Storage System using Modular Multilevel Converters," 19th International Conference on Electrical Machines and Systems (ICEMS), Chiba, 2016, pp. 1-6.

8) M. I. Daoud, A. Massoud, A. Elserougi, A. S. Abdel-Khalik, and S. Ahmed, "A Dual Three-Phase Induction Machine Based Flywheel Storage System Driven by Modular Multilevel Converters for Fault Ride Through in HVDC Systems," Asia-Pacific Power and Energy Engineering Conference APPEEC 2015, IEEE.